Unraveling the Competition between the Oxygen and Chlorine Evolution Reactions in Seawater Electrolysis: Enhancing Selectivity for Green Hydrogen Production

Catherine Harvey, Simon Delacroix, Cédric Tard

To cite this version:

Catherine Harvey, Simon Delacroix, Cédric Tard. Unraveling the Competition between the Oxygen and Chlorine Evolution Reactions in Seawater Electrolysis: Enhancing Selectivity for Green Hydrogen Production. Electrochimica Acta, 2024, 497, pp.144534. 10.1016/j.electacta.2024.144534. hal-04632808

HAL Id: hal-04632808

https://hal.science/hal-04632808v1

Submitted on 2 Jul 2024

Unraveling the Competition between the Oxygen and Chlorine Evolution Reactions in Seawater Electrolysis: Enhancing Selectivity for Green Hydrogen Production.

Catherine Harvey[a], Simon Delacroix[b], Cédric Tard[a,*]

[a] Laboratoire de Chimie Moléculaire (LCM), CNRS, École Polytechnique, Institut Polytechnique de Paris, 91120 Palaiseau, France

[b] Laboratoire de Physique de la Matière Condensée (PMC), CNRS, École Polytechnique, Institut Polytechnique de Paris, 91120 Palaiseau, France

* Correspondence and clarification can be addressed to Cédric Tard at cedric.tard@polytechnique.edu

Keywords: Oxygen Evolution Reaction, Chlorine Evolution Reaction, Selectivity, Heterogeneous Electrocatalysts, Seawater

Abstract

Selective oxidation of water without production of chlorine during the electrolysis of seawater is a critical impediment towards obtaining green hydrogen. Indeed, understanding the complex competitive mechanisms of oxygen and chlorine formation at the anode is an analytic challenge. An argument for direct seawater electrolysis is presented with a dissection of the complications that arise at the anode in the presence of seawater ionic constituents such as the chloride ion. Electrolyser system durability and the impact on the current and voltage efficiencies are discussed. Critical challenges at the anode under the acidic conditions of proton exchange membrane water electrolysis interrelate the thermodynamic and kinetic constraints of the oxygen evolution reaction (OER) and the chlorine evolution reaction (CER) to elucidate the heterogenous mechanisms of the OER and the CER and the crucial stability predicament under selective OER electrocatalysis. The selectivity circumstances resolved by Density Functional Theory computations shed insight onto the reaction conditions that select for the preferred OER adsorbate chemisorption on the surface and substantiates the observed overpotentials required for the OER and CER; experimental rotating ring disk electrode analysis further indicate competitive adsorption of OER and CER reactants under an assumed Langmuir isotherm model. Identifying the rate determining step and breaking the scaling relationship of the AEM OER pathway may both improve the stability of the catalyst and achieve lower OER overpotentials. Critical insight is given into designing the heterogeneous electrocatalyst structure with selective facets, additional point defects, and augmented active site density through single atom catalysts. An argument for the utilization of ruthenium for its high natural ubiquity and modulable valence states that can facilitate atomic configurations with optimal active site d-band center energies to promote selective adsorbate binding is presented. Studies of in-situ filtration of the chloride ion under acidic conditions highlight the utility of manganese oxide and silica; the augmentation of the conductivity through manipulation of polaronic interactions; and the design of heterogeneous electrocatalysts with self-healing characteristics demonstrated in select molecular catalysts that may decrease the overpotential of the OER and achieve selectivity. It is with the hope that these design strategies provide insights into future research efforts to uncover an electrocatalytic surface selective for OER evolution under the perilous acidic conditions and reveal an effective solution as serendipitous as the abundancy of a natural resource such as seawater.

Table of Contents

I. Introduction

I.1 The Social-Technological Crisis

Energy consumption is expected to reach 100,000 terawatt-hours (TWh) in the Net-Zero Emissions Scenario (NZES), outlined at the 2015 Paris agreement to minimize global temperature increases to 1.5 °C by the year 2050 [1,2]. This NZES expects water electrolysis to adsorb about 15,000 TWh to produce the required 520 mega tons of hydrogen to sustainably power our world [1,2]. Indeed, the generation of a hydrogen energy vector that is derived from renewable energy sources ("green hydrogen") would fulfill the world's energy shortage while also evading these climatically harmful carbon emissions that warm the planet [3,4]. Water electrolysis was initially discovered by two Dutchmen, Adriann Paets van Troostwijk (1752–1837) and Johan Rudolph Deiman (1743–1808), who connected two gold wires to an electrostatic generator that were each placed at either end of a glass tube filled with water [5]. The electric discharges of the generator produced evolved gases on both wires. Those evolved gases were interpreted to be oxygen at the anode and hydrogen at the cathode, shown in the reactions below under acidic conditions.

$$2H_2O \rightarrow 4H^+ + O_2 + 4e^- \ (OER, anode) \qquad (1a)$$

$$2H^+ + 2e^- \rightarrow H_2 \ (HER, cathode) \qquad (1b)$$

Considering that the production of one ton of hydrogen requires about 10 m^3 of water, there will become an exigency to source and also transport upwards of 5,2 km^3 of water [6]. With total global renewable freshwater resources estimated at 49,809 × 10^9 m^3 in 2020, exclusive withdrawals would dry up our critical freshwater resources within 100 years [7]. Moreover, utilizing freshwater to power electrolysis would heighten the emerging social-technological crisis inherent in the water-energy nexus [8]. More than two billion people live in countries experiencing water stress and an estimated 1.6 billion people live in regions with water availability though without the infrastructure to access it [9]. Alleviating that social-technological crisis and propelling the sustainability of our society requires unlocking the other 96.5 % of the 1.69 × 10^9 km^3 of seawater water on earth portrayed in Fig. 1a.

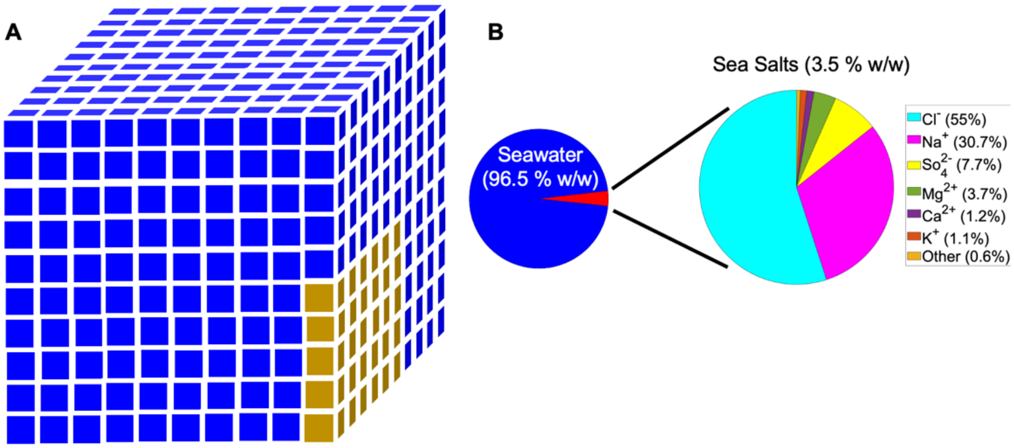

Fig. 1. (A) Graphical representation of the volumetric percentages of ice and seawater (97 % v/v) on the Earth represented by blue squares and freshwater (3 % v/v) represented by gold squares, adapted from Urban [8]. (B) Diagram of the major chemical constituents of seawater, sea salt percentages were adapted from the seawater reference composition defined by Millero et al. and represent the mass fractions of the solute with respect to the total mass of solutes at pH 8 [10].

However, there is plethora of chemical constituents in seawater including sea salts, small organic molecules, living organisms, and polymers (Fig. 1b) which create complications during the electrolysis [10,11]. Especially, one of the major challenges during the seawater electrolysis is the presence of chlorine anions which induces a competition between oxygen and chlorine production (CER).

I.2. State-of-the-Art Water Electrolyser Technologies

Undergoing the preferential oxygen evolution reaction (OER) at the anode and the hydrogen evolution reaction (HER) at the cathode leads to local acidification at the anode as water or hydroxide ions are consumed under acidic or neutral/basic conditions and protons or water are produced (*Reaction 2a* and *Reaction 2b*), and a local basification at the cathode as protons or water molecules are consumed under acidic or neutral/basic conditions and water or hydroxide ions are produced (*Reaction 3a* and *Reaction 3b*).

$$2H_2O \rightarrow 4H^+ + O_2 + 4e^- \quad (Anode\ in\ acid) \tag{2a}$$

$$4OH^- \rightarrow 2H_2O + O_2 + 4e^- \quad (Anode\ at\ neutral\ or\ alkaline) \tag{2b}$$

$$H^+ + 2e^- \rightarrow H_2 \quad (Cathode\ in\ acid) \tag{3a}$$

$$2H_2O + 2e^- \rightarrow H_2 + 2OH^- \quad (Cathode\ at\ neutral\ or\ alkaline) \tag{3b}$$

The pH dependence of the OER enables the reaction at the anode to evolve at voltages below its characteristic reversible potential of 1.23 V – 0.059·pH vs. RHE in alkaline solutions in accordance with the Nernst relation. Alkaline water electrolysis (AWE) utilizes a cell with two compartments continuously fed with a highly concentrated, corrosive alkaline supporting electrolyte (often 20–30 wt% (ca. 7 M) KOH solution), though this design is subject to leakages and require periodic replenishment (Fig. 3a). The electrodes are separated by a porous diaphragm to prevent gas crossover, though this diaphragm has been shown to poorly operate, causing low Faradaic efficiencies, and limiting the maximum AWE current densities to about 0.2 - 0.4 A/cm^2 despite the use of the highly concentrated supporting electrolyte [12]. The device must also be operated at ambient pressures, making the produced hydrogen significantly wet and increasing the cost of drying and compression. Moreover, electrolysis of seawater under alkaline conditions can induce hydroxide precipitation and reduce the lifetime durability of the electrolyser and the active surface area of the electrocatalyst [13].

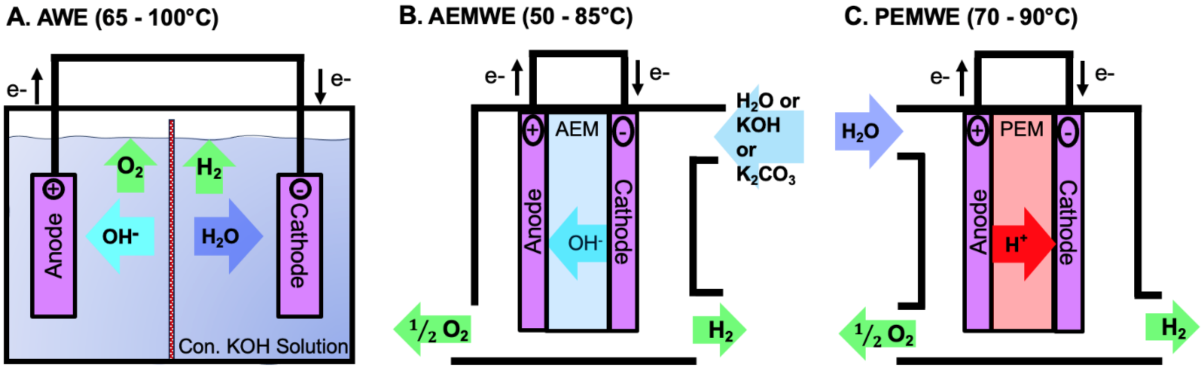

Fig. 2. (A) An alkaline water electrolyser with a concentrated KOH liquid supporting electrolyte pumped on both sides of the cell with a porous diaphragm that impedes gas crossover while promoting the migration of the hydroxide ions generated at the cathode toward the anode. (B) An anion exchange membrane water electrolyser consisting of a solid cationic polymer promoting migration of hydroxide ions from the cathode to the anode where oxidation occurs; water with or without a dilute supporting electrolyte such as potassium hydroxide or potassium carbonate is shown being supplied to the cathode. (C) A proton exchange membrane water electrolyser with water being supplied to the anode; the evolution of oxygen promotes the generation of protons that then migrate through the solid poly-sulfonic membrane towards the cathode to evolve hydrogen. Reproduced from Li et al. [14].

Anion exchange membrane water electrolysis (AEMWE) utilizes an anion exchange solid polymer electrolyte (< 50 μm in thickness). This membrane facilitates the transport of hydroxide ions from the cathode to the anode and separates the evolved gases while decreasing the ionic resistance. Thus AEMWE can operate at higher pressures with more efficient current densities (Fig. 3b). Indeed, Li et al. reported current densities of 2.7 A/cm^2 using an ammonium-enriched anion exchange ionomer embedding both the cathode and the anode [15]. To improve the ionic conductivity, dilute solutions of KOH (< 1 M) supporting electrolyte or potassium carbonate are often needed, though pure water is preferred to minimize chemical and device maintenance. Water is indeed a feasible electrolyte solution with an ionomer of sufficient cationic functionality and electrode binding ability [12,14]. Moreover, the non-acidic environment enables the use of non-precious metals electrocatalysts such as first-row transition metal oxides, nitrides, and sulfides decreasing the capital expenditure, and increasing the scalability. Anion exchange membranes can also enable the design of asymmetric electrolysers with independent electrolyte feeds to promote the selectivity for the OER at the anode [16]. Dresp et al. developed an electrolyser where 0.5 M KOH anolyte circulate in the anode compartment which was separated from natural seawater catholyte by an AEM membrane. Only few millimole of chloride ion can cross over in the anolyte, unaffecting the NiFe-LDH electrocatalyst. In another study, a custom made biphenyl-based ionomer showed high anion exchange capacities contributing to low overpotential at high current densities [17].

The highest current densities are achieved with proton-exchange membrane water electrolysers (PEMWE). In PEMWE, a solid polymer electrolyte membrane between the anode and the cathode such as Nafion is used to facilitate migration of the protons generated at the anode towards the cathode where their reduction occurs (Fig. 3c). This solid polymer allows for high operating pressures. However, it is especially vulnerable to water impurities, which can become trapped and concentrated, reducing the proton conductivity. Moreover, the harshly acidic conditions require the use of platinum group metals (PGM) such as iridium or ruthenium at the anode to catalyze the OER, and platinum or palladium HER catalysts at the cathode. The local acidification of the anode caused by the OER at high current densities may moreover increase the degradation of the electrode materials. Thus, it is crucial to develop acidic resistant catalysts to avoid continuous buffer additions [[18], [19], [20], [21]]. Unfortunately, the thermodynamic potential difference between the OER and the parasitic CER when electrolyzing seawater is the lowest under acidic conditions. To avoid the chlorine production, Rossi et al. use an asymmetric design electrolyte feed in which a humidified gas stream is introduced at the anode, while the chloride ions in the seawater catholyte were prevented from crossover by the electrostatic repulsions presented from the anionic functionalities of the membrane [22]. The vapor anolyte further reduced the occurrence of sodium ion transport and decreased the observed overpotentials of the cell [22]. Kumari et al. went one step further to introduce seawater humidified air at the anode and a nitrogen gas stream in the cathode compartment; the solar hydrogen conversion efficiency calculated before and after 50 h of continuous operation was found to increase from 6 % to 6.3 % compared to the decrease of 6.6 % to 0.5 % observed when liquid seawater electrolytes feeds were used [23].

I.4.1 Abating the Use of Precious Metals in PEMWE

Krishnan et al. calculated an 82 % price reduction in the PEMWE stack design through alternative materials utilization and lower loadings of PGM electrocatalysts. Unfortunately, the high overpotential for the OER, the low pH contributed by the ionic membrane, and the highly oxygenated environment at the anode necessitates an electrocatalyst with a durability currently only characteristically found in iridium [24]. Though with loadings of 2 mg/cm^2 required to achieve typical operating conditions of 2 A/cm^2 and 2 V, only a capacity of > 1 GW per year of PEMWE production technology can be achieved by tapping almost 10 % of the annually mined production [24]. Though to meet the NZES for 2050, upwards of 3600 GW must be realized [24], thus ensuing an iridium shortage [25]. On the other hand, costing a sixth to a fifteenth of the price of the extremely rare iridium metal with 0.001 ppm in the Earth's crust, both DFT studies and experimental measurements of its overpotential have rendered ruthenium as the precious metal with remarkable OER electrocatalytic activity under acidic conditions [26,27]. However, its preferential utilization must address its characteristically low stability.

Therefore, there exists a challenge to reduce the precious metal loadings without however sacrificing the performance and durability of the electrocatalyst. Alia et al. indeed showed that reduced metal loadings can degrade the current density over the long term [28]. Thus coherent strategies to diminish the precious metal loading are exigent. Improving the catalytic interface by incorporating supportive substrates with improved electrical conductivity; optimizing the surface area of the catalyst structure and iridium packing density by implementing the design of 1D and 2D nanomaterials; utilizing reactive spray deposition technologies with a self-assembly mechanism proceeding through volatile solvent evaporation that creates a porous hierarchical structure with low Ir loadings [29] are some methodologies that have been explored and discussed in the literature. Techniques that improve catalyst recycling such as ultrasonication and alcoholic delamination have also been reported [30,31].

Development of non-PGM catalysts would evidently alleviate the cost burden of current PEM technology and the taxing utilization of precious natural resources. However, the lacking level of performance and durability of these alternatives when compared to Ir have continually rendered this feat elusive [24]. Towards assuaging this predicament, Wang et al. identified 68 nonbinary acid-stable oxides as electrocatalysts at the anode for PEMWE from the data of the Material Project through computation of Pourbaix decomposition free energies. For example, Sb, Ti, Sn, Ge, Mo, and W-based oxides were indicated to have high corrosion resistance in strong acids [32]. Moreover, Li et al. identified a stable potential window in which γ-MnO_2 showed no signs of deactivation after 8000 h of electrolysis at 10 mA/cm^2 and pH = 2 [33]. Hernandez et al. reported a nickel-manganese antimonate electrocatalyst that performed the OER in 1 M sulfuric acid, though required an overpotential of 735 mV operating at 10 mA/cm^2 for 168 h [34]. Thorarinsdottir et al. elucidated the OER catalytic mechanism of bismuth oxide (BiO_x) films electrodeposited on fluorine-doped tin oxide-coated glass working electrodes and posited that two $Bi^{3+}O_x$ centers undergo two sequential two-electron oxidations to form the symmetric peroxo $Bi^{4+}O_xBi^{4+}O_x$ entity, which then disproportionates intermolecularly to form a mixed valence $Bi^{3+}O_xBi^{5+}O_x$ peroxo species [35]. Upon oxidation to form $Bi^{5+}O_xBi^{5+}O_x$, oxygen is subsequently released. No distinctive changes in film morphology were evident through SEM following chronopotentiometry testing; an OER current density of 1–5 mA/cm^2 was sustained at moderate overpotentials for 110 h at pH 1.82, acidified with sulfuric acid [35]. These results further demonstrated that the p-block metal oxides often used as the stabilizing embedding matrices may indeed play a catalytic role in acidic OER electrocatalysis. On the other hand, an overpotential of 189 mV at 1 mA/cm^2 was recorded for a metal molecular cluster anion, a barium salt of cobalt polyoxometalate blended with a commercial carbon paste support; this design showed a stable current density for one day that was 10 times higher than that of iridium oxide (IrO_2) blended with the carbon paste support, producing a TON of 47 compared to 0.1 for IrO_2 when corrected for the metal content. This was the first instance in which a low-cost, earth abundant material reached comparable activities to the commercial IrO_2 standard [36].

I.2 Indirect Seawater Electrolysis Technologies

The complexity of seawater instigates the development of new strategies to electrolyze this abundant resource to produce hydrogen. Desalinization of seawater is currently used in electrolyser technologies and called indirect seawater electrolysis. Current desalination technologies include forward osmosis [37,38] and reverse osmosis (RO). RO occupied 66 % of the global water desalination in 2016 and utilizes polyamide membranes capable of 99.7 % salt rejection [[39], [40], [41], [42]]. These relatively easy single reverse osmosis technologies can produce water with conductivities of 5–20 μS/cm. However, the European Union recommends low temperature water electrolysis to be conducted according to ISO 3696 Grade 2 water with a conductivity of < 1.0 µS/cm [[43], [44], [45], [46]]. Thus, the infrastructure for additional purification is required. Reverse osmosis membranes could be placed in series, though each of these high pressure pumps require 2 to 4 kWh of energy to produce 1 m^3 of freshwater [47]. Purifying the needed 5.2 km^3 of water to meet the NZES could thus require 20.8 TWh of energy as highlighted in Fig. 2. Thus it is of a fundamental importance to continue scientific advancement into the development of direct seawater electrolysis to spare energy.

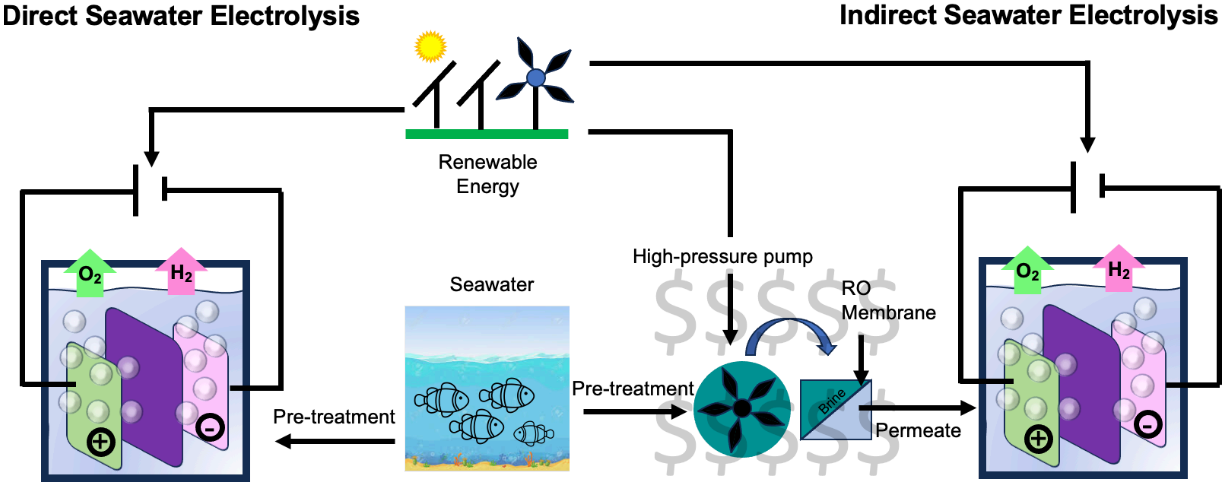

Fig. 3. Schematic comparison of Direct and Indirect Seawater Electrolysis highlighting the additional energy costs required to power the high-pressure pump module. Figure adapted from Farràs et al. [48].

II. Mitigating Seawater Electrolyser Performance

It is therefore crucial to be able to produce green hydrogen with direct electrolysis starting from seawater. However, the presence of salts induces drop in performances.

II.1 Parasite Reactions in Seawater Electrolysers

The electrolysis of non-purified seawater has been shown to degrade the electrolyser system performance. The carbonate and borate ions in seawater are present, though at concentrations too low to buffer a seawater electrolyte from these dramatic pH shifts that occur upon the preferential evolution of oxygen and hydrogen at the anode and the cathode. The local acidification that occurs at the anode enables seawater constituents such as the chlorine chemistry to promotes the corrosion and toxicity. The local basification that occurs at the cathode causes hydroxide precipitation and the blockage of the electrode surfaces and the membrane materials. This convoluted composition can thus affect the chemical and mechanical robustness of the electrolyzer, the electrochemically active dimensions of the electrode, and the specific operating conditions (voltage, current density, solution feed rate, response time to reach steady-state operation) [49].

Furthermore, the presence of additional chemical constituents into the electrolyte of the electrolyser can create competition among the substrate at the active site of the electrocatalyst [11,50]. In particular, the chloride ion can be oxidized at the anode (**Reaction 3** of Fig. 4) in place of water to create toxic chlorine gas. After the CER, the evolved chlorine or its disproportioned species can then travel to the cathode and be reduced as shown in **Reaction 4** of Fig. 4 corroding the cathode. The chloride ions can also replace the oxygen atoms in a passivated surface and cause pitting corrosion along the anode, as shown in **Reaction 5** of Fig. 4 [[51], [52], [53], [54]]. The catalysts can also become poisoned by the presence of these noninnocent ions, **Reaction 6** of Fig. 4. [55,56].

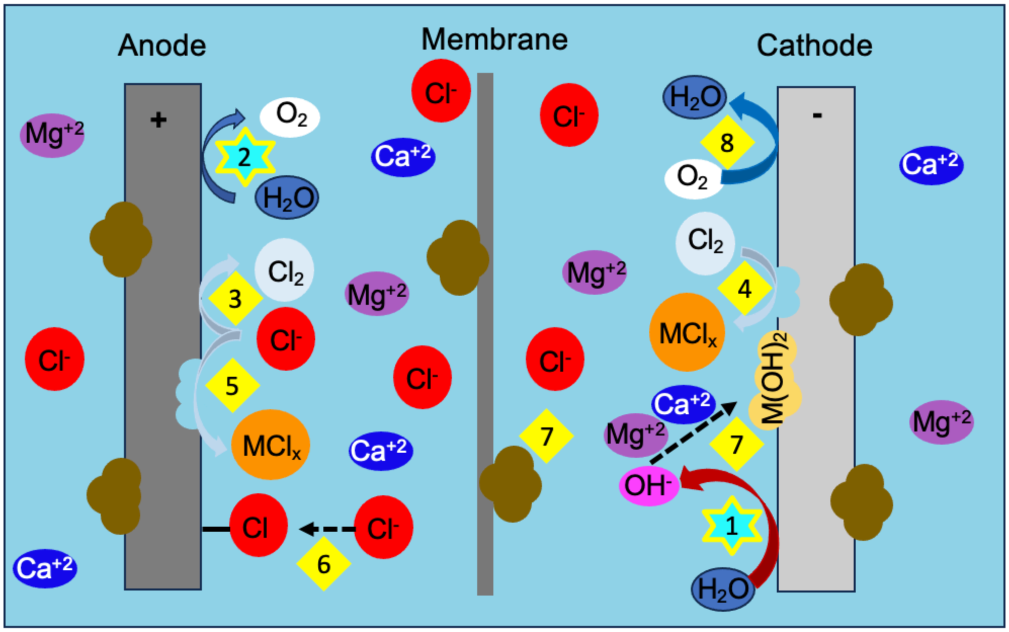

Fig. 4. Depictive representation of the inherent complications of seawater electrolysis. The desired efficiencies for the HER (Reaction 1) and OER reactions (Reaction 2) can be undermined by the presence of antagonistic ions in the electrolyte such as the chloride ion, which can compete with water to undergoes oxidation at the anode (Reaction 3). The toxic chlorine gas and its disproportionation species can then undergo reduction at the cathode and corrode the electrode (Reaction 4). The chloride ion can also corrode the anode by replacing the oxygens along the passivated surface (Reaction 5). The ions can also inhibit the catalysts at the anode and cathode by affecting their functionality and promoting dissolution (Reaction 6). The local basic environment of the cathode can also cause magnesium and calcium hydroxides to precipitate and block the functionality of the electrocatalysts; these deposits can also become trapped along the electrolyser membrane (Reaction 7). Parasitic oxygen reduction reactions can also occur at the cathode (Reaction 8).

Other ions present in seawater can also affect the electrode integrity. The precipitation of magnesium and calcium hydroxides, shown in **Reaction 7** of Fig. 4, lead to depositions on the electrode surface that inhibit the functionality of the electrocatalysts [57,58]. These magnesium and calcium hydroxide precipitates can also become trapped and concentrated in electrolyser membranes, causing deactivation and reducing the lifetime durabilities of these essential components [59]. Han et al. utilized a bipolar membrane consisting of an anion exchange layer and a cation exchange layer under reverse bias to promote local acidification in the catholyte to inhibit this inorganic precipitation [60]. Sadly, this novel design decreases the susceptibility towards evolved O_2 which can cross toward the membrane and induced aa parasitic oxygen reduction reaction (**Reaction 8**, Fig. 4) [11,50]. Finally, membranes could be subject to significant microbial fouling in presence of seawater [61]. For example, Belila et al. found that 0.25 % of the bacterial operational taxonomic units were present at all stages within a water desalination plant, and further indicated that chlorination was not effective at inactivating all bacteria and preventing microbial growth [62]. Though Debiemme-Chouvy and Cachet do suggest that electrochemical methods such as the generation of hydrogen bubbles and a low-intensity electrical potential may prevent the formation of a biofilm [63].

It worth to mention that all these precipitates and deposits decreases logically the electrochemically active surface of the cell and stack components. In addition, gas bubbles generated during the electrolysis of seawater may also be less prone to coalesce than the ones in freshwater (Fig. 5) [64,65]. Tourneur et al. have however recently found that the introducing cylindrical micropatterns at the surface of the electrode can promote gas bubble release [66].

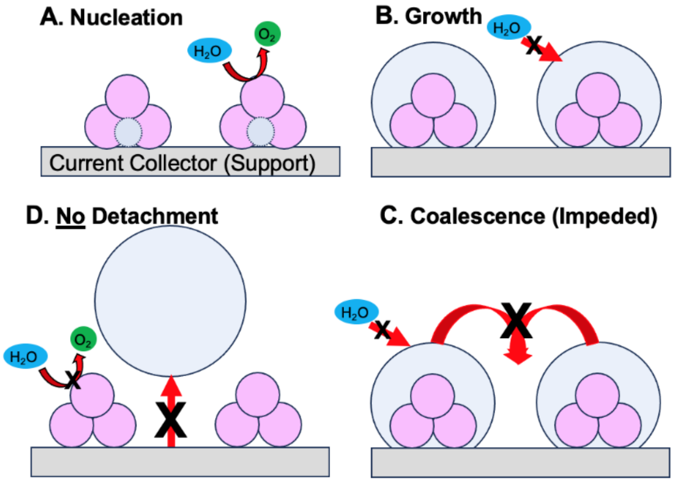

Fig. 5. Stages of gas bubble (grey) formation on an electrocatalytic nanoparticle (pink) along a conductive support beginning with (A) nucleation followed by (B) growth. Seawater impedes the coalescence of the bubbles (C) preventing the electrocatalytic material from oxidizing (or reducing) adjacent water molecules (D).

II.3 Drop in the Electrolyzer Efficiency using Seawater

The efficiency of the individual cells may be determined as a product of the current efficiency ($\tilde{\eta}_C$) and the voltage efficiency ($\tilde{\eta}_U$), which includes the power consumption to maintain the heat balance during endothermic and exothermic electrode processes and prevent potential electrolyte freezing and elevated temperatures [67]. All the parameters influencing the efficiency are listed in Table 1 (adapted from Schalenbach et. Al) [77].

$$\tilde{\eta}_{cell} = \tilde{\eta}_C * \tilde{\eta}_U \tag{4}$$

Table 1. Classification of the operational parameters, electrolyte characteristics, and properties of the electrocatalyst and the electrodes that affect the voltage efficiency, the current efficiency, the heat balance, and thus the overall cell efficiency. Adapted from the work of Schalenbach et al. [67].

	Cell efficiency		
	Voltage efficiency	Current efficiency	Heat balance
Operation parameters	Temperature Pressure Cell current	Temperature Pressure Cell current	Temperature Pressure Cell current
Electrolyte	Membrane thickness Conductivity	Membrane thickness Diffusivities Permeabilities	Membrane thickness Vapor pressure
Catalyst and electrodes	Morphology Permeability Activity Surface area Conductivity	Morphology Permeability	

II.3.1 The Current Efficiency

The current efficiency ($\tilde{\eta}_c$) also known as a faradaic efficiency, is the ratio between the moles of hydrogen produced (Δn_{H_2}) to the moles of electrons used during the electrolysis process (Δn_{e^-}). The current efficiency can be given by the following equation:

$$\tilde{\eta}_c = \frac{\Delta n_{H_2}}{\Delta n_{e^-}} = \frac{\frac{I\Delta t}{2F} - \Delta n_{loss}}{\frac{I\Delta t}{2F}} = \frac{I - 2F\left(\frac{\Delta n_{loss}}{\Delta t}\right)}{I} = \frac{I - I_{loss}}{I} \tag{5}$$

Where (I) is the current, (t) is the time, and (F) is Faraday's constant.

Current efficiencies at the anode and cathode are affected by two major losses. The first one is the recombination of H_2 and O_2 in H_2O and the second one is the current loss caused by the parasitic CER. The recombination of H_2 and O_2 is caused by the diffusion of the gases through the membrane and the convection insured by the electrolyte of the solubilized gases through the membrane [67]. Thus, I_{loss} can be written as following:

$$I_{loss} = I_{loss}^{recombination} + I_{loss}^{CER} \tag{6a}$$

$$I_{loss} = 2F\left(\frac{K}{\mu} p_c^{H_2} - D_{H_2}\right) S_{H_2} \frac{\Delta p}{d} + 4F\left(\frac{K}{\mu} p_a^{O_2} - D_{O_2}\right) S_{O_2} \frac{\Delta p}{d} + I_{loss}^{CER} \tag{6b}$$

Gordon et al. reported the solubility of hydrogen at various salinities of local seawater samples. They found the hydrogen solubility to decrease with increasing salinity [68].

Thus, differences in hydrogen diffusivity and permeability through the membrane are expected to affect the cross-permeation flux densities.

II.3.2 The Voltage Efficiency

The voltage efficiency, $\tilde{\eta}_U$, can be defined with respect to the reversible voltage of a water electrolytic cell ($U_{rev,T}$) and the applied voltage (U_{cell}). These two parameters are affected by the use of seawater.

$$\tilde{\eta}_U = \frac{U_{rev,T}}{U_{cell}} \tag{7}$$

The reversible voltage ($U_{rev,T}$) is affected by the presence of salts in water. Indeed, increasing the salinity of the aqueous electrolyte solution is known to lower its characteristic vapor pressure (p_w) at a total pressure (p) [69]. By assuming that the water vapor is ideal and in equilibrium with the water in its electrolyte solution at a vapor pressure (p_{w^*}), the effect of this vapor pressure on the reversible voltage of a water electrolytic cell $U_{rev,T,p}$ at temperature (T) may be defined as following [70]:

$$nFU_{rev,T,p} = nFU^{\circ}_{rev,T} + RT\ln\left[\frac{(p-p_w)^{3/2}\bullet p_{w^*}}{p_w p^{1/2}}\right] \tag{8}$$

Where the Nernst relation with the standard reversible voltage ($U^{\circ}_{rev,t}$) may be equated to the standard free energy of formation of liquid water, which at 25°C is -2.37 x 10^5 J, giving ($U^{\circ}_{rev,t}$) a value of 1.229 V.

The applied cell voltage (U_{cell}) is also modified by the use of seawater. Indeed, (U_{cell}) is defined as the sum of the Nernst voltage U_N, the ohmic drop U_Ω ,and the kinetic overpotential U_{kin} [67].

$$U_{cell} = U_N + U_\Omega + U_{kin} \tag{9}$$

U_N is affected by the partial pressure ($p^c_{H_2}$) and ($p^A_{O_2}$) at the cathode and anode, respectively. Assuming that the gaseous hydrogen and oxygen produced at the electrodes are saturated with the water vapor, we obtained the following expression for U_N.

$$U_N = U^{\circ}_{rev,T} + \frac{RT}{2F}\ln\left(\frac{p^C_{H_2}\sqrt{p^A_{O_2}}}{p^{3/2}a_{H_2O}}\right) \tag{10}$$

Where *R* is the universal gas constant, *T* is the temperature, (a_{H_2O}) is the activity of water, ($p^c_{H_2}$) and ($p^A_{O_2}$) represent the partial pressures of hydrogen and oxygen at the cathode and anode, respectively, and (*p)* denotes the ambient total pressure as used above.

However, depending on the pH of the solution, only the proton and/or hydroxide ions involved in the oxidation and reduction reactions of water electrolysis that evolve the measured stationary currents at the anode and the cathode can contribute to the specific conductance (K_s) of the electrolyte [67]. Seawater alone is known to have a lower specific conductance than the buffered osmotic water used in PEMWE or AWE technologies. Electrolyzing seawater alone will thus require a greater applied cell voltage (U_{cell}) due the increase in the Ohmic drop (U_Ω), of the cell by increasing the total DC resistance between the cathode and the anode (R_t), which affects the overall voltage efficiency of the electrolyzer [71].

$$U_\Omega = R_t j \qquad (11a)$$

$$R_t = \frac{1}{\mathrm{K}_s} \qquad (11b)$$

II.3.2.1 A Consideration for the heat flow.

It is desirable for electrolysers to operate at a fixed temperature. Leroy et. al. defined the thermobalanced voltage (U_{TB}) by considering the heat of vaporization ($T\Delta S$) caused by the phase transition of liquid water to gaseous oxygen and hydrogen, the heat of vaporization (H_{ev}^{gas}) that accounts for the phase transition of liquid water into gaseous water vapor, and the energy required to increase the temperature of the supply water at ambient temperature (20 °C) to typical cell temperatures of 80 °C (E_{Supply}),

$$U_{TB} = U^{\circ}_{rev,T} + \frac{T\Delta S}{2F} + \frac{E_{Supply}}{2F} + \frac{H_{ev}^{gas}}{2F} \qquad (12)$$

The voltage efficiency can thus be further defined.

$$\tilde{n}_U = \frac{U_{rev}}{U_{TB}}\ for\ U_{cell} \leq U_{TB} \qquad (13a)$$

$$\tilde{n}_U = \frac{U_{rev}}{U_{cell}}\ for\ U_{cell} > U_{TB} \qquad (13b)$$

To conclude, the decreases of the vapor pressure (p_w) and the specific conductance of the electrolyte with the use of seawater will increase the reversible voltage ($U_{rev,T,p}$), the thermobalanced voltage (U_{TB}), and the applied cell voltage (U_{cell}) decreasing the efficiency.

III. Critical Challenges at the Anode

The strategic exigency for a design at the anode that mitigates the chemical and mechanical degradation of the overall electrolyser performance during seawater electrolysis is convoluted in part by the chlorine species that can form upon perturbing the solution pH and adjusting the potential applied at the anode.

III.1 Thermodynamic Constraints of the OER and CER

The reduction-oxidation equilibria of the predominate chloride species at certain pH and electrical potential is given by the Pourbaix diagram in Fig. 6 [20,72,73].

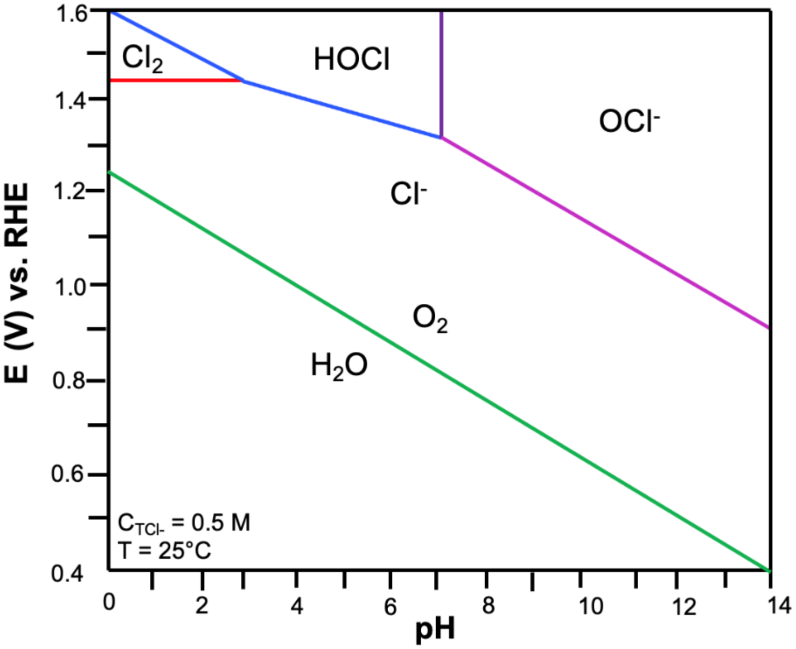

Fig. 6. Pourbaix diagram of a salinated aqueous electrolyte (0.5 M NaCl) indicating the stable chemical species that are evolved as the pH and electrode potential are varied. The green line represents the pH and electrode potential values at which a thermodynamic equilibrium between water and oxygen exists; pH and electrode potential combinations above this line indicate regions at which oxygen can be evolved from water. The red line similarly indicates the electrode potentials and pH values where chlorine gas is evolved. The blue line and the magenta line indicate the onset of the hypochlorous acid and hypochlorite ion, respectively. The purple line indicates the pH and electrode potentials at which a thermodynamic equilibrium exists between the hypochlorous acid and hypochlorite.

Different chemical species can be electrochemically generated from the parasitic oxidations of the chloride ion including Cl_2, HClO, and ClO^- in acidic, neutral, and basic pH conditions. Specifically, under acidic conditions,

$$2Cl^- \longrightarrow Cl_2(aq) + 2e^- \qquad E^0 = 1.36\,V\ vs.SHE \tag{14}$$

Moreover, it is apparent that the voltage difference between the OER and the thermodynamically unpreferred formation of hypochlorite is largest under basic conditions (480 mV). This difference promotes the high OER selectivity evident in alkaline seawater electrolysis [72]. Non-PGM catalysts stable in these basic conditions have been reported with OER faradic efficiencies approaching 100 % [72,74,75].

III.2 Heterogeneous Mechanisms of the OER and the CER

Present in a phase different from the reactants, heterogenous catalysts are easily separable from the reactants and the products after the reaction. Thus they are very desirable for high volume transformations such as those within the energy sector. The heterogeneous catalysts interact strongly with the reactants, intermediates, and products in what is known as an inner sphere electrode reaction, or the electron transfer can occur through a monolayer of solvent in between the solid catalyst and the reactants, products, and intermediates in what is known as an outer sphere electrode reaction [76]. Indeed, the characteristics of the interface can greatly influence the rate of electron transfer, the required overpotential, and the resulting faradaic current. Three different major mechanisms are referenced in the literature for the OER: the electrochemical oxide mechanism (EOM), the adsorbate evolution mechanism (AEM), and the lattice oxygen oxidation mechanism (LOM).

III.2.1 Elucidated Mechanisms for the Oxygen Evolution Reaction

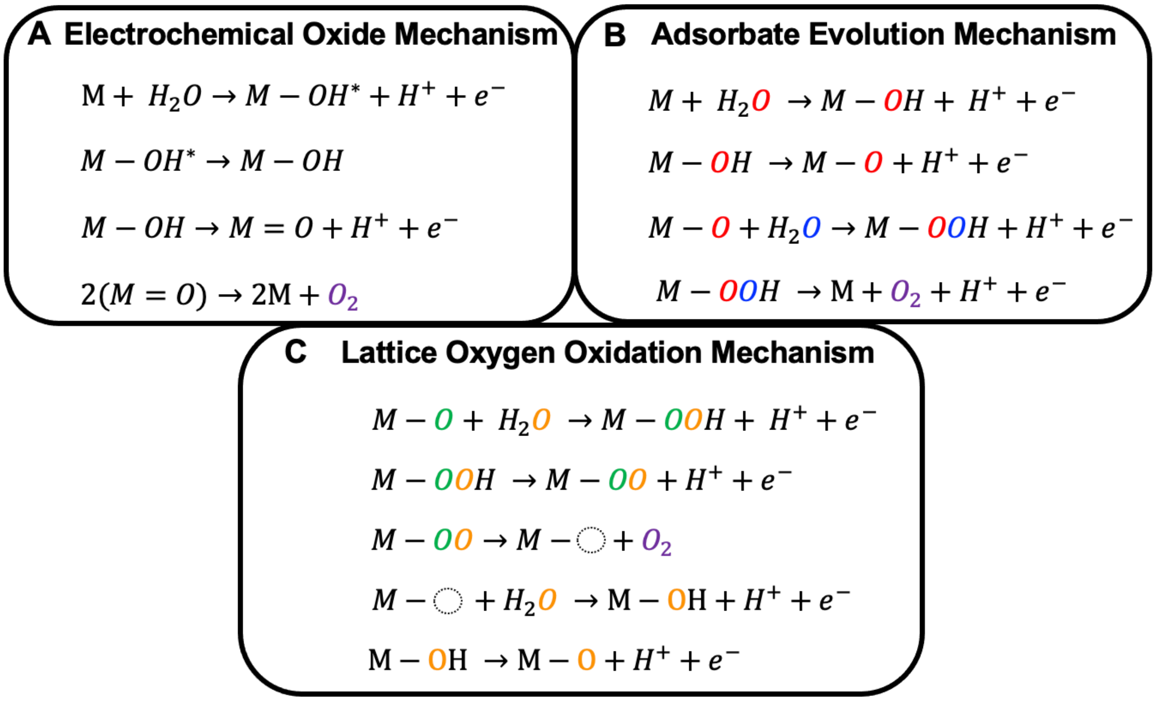

$$M + H_2O \rightarrow M - OH^* + H^+ + e^-$$
$$M - OH^* \rightarrow M - OH$$
$$M - OH \rightarrow M = O + H^+ + e^-$$
$$2(M = O) \rightarrow 2M + O_2$$

$$M + H_2O \rightarrow M - OH + H^+ + e^-$$
$$M - OH \rightarrow M - O + H^+ + e^-$$
$$M - O + H_2O \rightarrow M - OOH + H^+ + e^-$$
$$M - OOH \rightarrow M + O_2 + H^+ + e^-$$

$$M - O + H_2O \rightarrow M - OOH + H^+ + e^-$$
$$M - OOH \rightarrow M - OO + H^+ + e^-$$
$$M - OO \rightarrow M - \bigcirc + O_2$$
$$M - \bigcirc + H_2O \rightarrow M - OH + H^+ + e^-$$
$$M - OH \rightarrow M - O + H^+ + e^-$$

Fig. 7. Proposed reaction pathways for the oxygen evolution reaction elucidated (a) from Tafel kinetics and DFT studies, (b) through DFT studies, and (c) by a combination of DFT, OLEMS, XPS, and XAS.

III.2.1.1 Electrochemical Oxide Mechanism.

Initial evidence demonstrating the effect that the solid electrocatalyst can have on the kinetic rate of the reaction was first mounted by Bockris et al., who found the rate of electron transfer to be dependent on the work function of the metal [77,78]. J. O'M. Bockris was also the first to calculate the corresponding Tafel slope for different considered reaction mechanisms in the oxygen evolution reaction. The approach assumed only one step in the mechanism was rate determining. Thus, the produced intermediates from the non-rate determining steps were present in only small concentrations and the saturation of the surface was only appreciable with the reactants of the rate determining step [79]. These calculations were compared to Tafel slopes obtained from experimental analysis of the log current vs. overpotential data and an electrochemical oxide path was proposed. The EOM was later refined by Over and Castelli et al. with DFT calculations. They propose an additional structural rearrangement of the bound oxide (step 2) to be the rate determining step as shown in Fig. 7a [80,81,82]. By further studying the relative stabilities of the most pertinent spin states through DFT, Busch et al. modeled the OER reaction cycle of a biomimetic catalyst, a μ-OH Mn(III-V) dimer bridged through hydroxide entities and truncated with acetylacetonate-type ligands [83]. The electrochemical oxide mechanism was confirmed with an oxidation of Mn–OH to Mn=O prior to the generation of O_2, which was found to occur through a chemical step in which the two Mn=O moieties recombine in what has become known as a binuclear mechanism [83,84].

III.2.1.2 Adsorbate Evolution Mechanism.

The proposed proton concerted electron transfer (PCET) mechanism shown in Fig. 7b, known as both the adsorbate evolving mechanism and the mononuclear mechanism, is thought to initiate with an acid-base nucleophilic attack [85,86].

To theoretically study this mechanism, the (ΔG_{RX}) of each intermediate formed in the pathway has to be computed. It requires the computing of the chemisorption ($\Delta\epsilon$), the zero-point energy adjustment (ΔZPE), and the entropy (ΔS) as shown in Eq. (15), though also corrected for the total energy of the gases [87,88],

$$\Delta G_{RX} = \Delta\epsilon(z) + \Delta ZPE - T\Delta S \tag{15}$$

The chemisorption energy is quantified by measuring the change in potential energy of the adsorbate-catalyst system ($\Delta\epsilon_{pot}$) as a function of the adsorbate distance (Z) above the solid surface [89]. To calculate (Δε), Norskov et. al. developed the computational hydrogen electrode (CHE) method. Rather than computing the solvation energies of the electrons and protons, Norskov et. al. assumed a chemical equilibrium between gaseous hydrogen molecules and solvated protons and electrons [90]. Thus, a simple computation of the free energy of the H_2 molecule in the gas phase can be conducted and the free energy (ΔG_{RX}) of each intermediate reaction (i.e. $M - OH \rightarrow M - O + H^+ + e^-$) can be calculated as the free energy of the reaction $M - OH \rightarrow M - O + \frac{1}{2}H_2(g)$.

One example of the calculated chemisorption energies ($\Delta\epsilon$) of each intermediate onto active surface sites was made by Rossmeisl et. al. on a (110) RuO_2 surface [91]. The active surface sites consisted of either a bridge site between two fourfold coordinated metal ions (in purple), or a coordinately unsaturated site (CUS) located on top of a fivefold coordinated metal at the surface (in light orange) in Fig. 8.

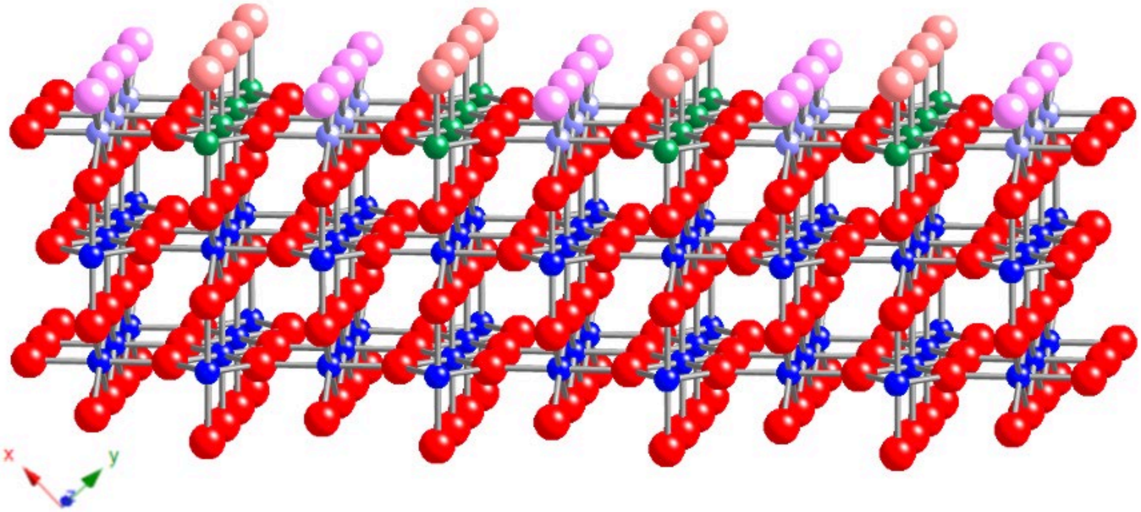

Fig. 8. Representation of the bulk Ru and O atoms in blue and red, respectively, and the surface atoms, consisting of bridging Ru sites in purple and CUS Ru sites in green. Oxygen adsorbates on the electrochemically active Ru CUS sites are shown in light orange and the pink atoms on the Ru bridge sites represent surface oxygens.

The mononuclear mechanism considers the CUS sites to be the primary active site on the surface of the rutile metal oxide structure [92]. The activation of bridge sites, that can occur by doping the metal oxide, creates a proton donor-acceptor moiety. This modification can initiate the bifunctional OER mechanism [92] and the bifunctional OER mechanism 2. These mechanisms differ only in that the splitting of the water during the formation of the peroxide adsorbate occurs electrochemically in the first and chemically in the second [93,94].

The chemisorption energies of these intermediates can be utilized to calculate the Gibbs Free Energy ($\Delta G_{RX}(U)$) of each reaction step (X) in the mechanism as a function of the electrode potential (U) [91].

$$\Delta G_{RX}(U) = \Delta G_{RX} - ne_0U + k_bTpH\ln 10 \tag{16}$$

The potential determining step is the formation of the intermediate peroxide. Assuming that the rate determining step is determining by the potential determining step, the reaction mechanism may be deduced on a thermodynamic basis [[95], [96], [97], [98], [99]]. To minimize the overpotential required to complete the reaction, the energies of the three intermediates must be tuned. However, Rossmeisl and coworkers further found that the energies of the different intermediates are linearly correlated and are thus unable to be varied independently. It further limited the ability to optimize the electrocatalyst towards catalyzing the reaction at the minimum reversable potential value (E_E) of the overall reaction [95,96,100].

Thus computing the chemisorption energy of the second intermediate of the pathway depicted in Fig. 7.b ($M-O_{ads}$) enables the ΔG_{RX} value for the $M-OH_{ads}$ and $M-OOH_{ads}$ intermediates to be determined. Indeed, this constant difference of 3.2 eV between the $\Delta G(M-OH_{ads})$ and $\Delta G(M-OOH_{ads})$ rather than the ideal 2.46 eV indicates an inherent overpotential [101]. Further optimizing the proton donor/acceptor functionality of the bridge sites along the ruthenia catalyst surface and activating the bifunctional mechanisms has been proposed to break that scaling relation [92]. Finally, by modeling (Δε), the ability of the catalytic surface to form the chemical bond with the $M - O_{ads}$ intermediate, the reaction rate, the catalytic activity, of electrocatalyst for the OER can be calculated [102]. By thus plotting the catalytic activity as a function of the $\Delta\epsilon_{M-O_{ads}}$, a volcano-shaped curve can be obtained, as shown in Fig. 9.

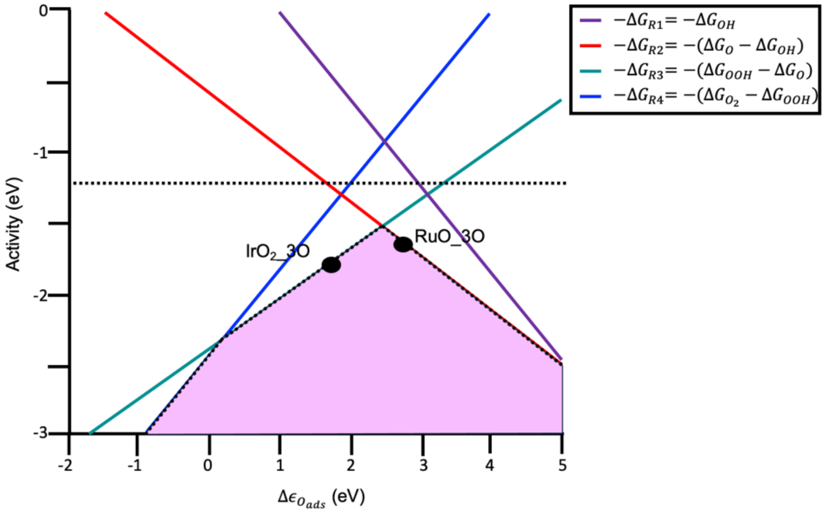

Fig. 9. The theoretical activity of the four charge transfer steps of the proposed AEM oxygen evolution reaction on a metal oxide surface. Along the y axis are the activities of each step along the proposed reaction pathway, which are shown to be linearly coordinated with the oxygen dissociative chemisorption energies plotted on the x axis along the oxide surface. The resulting volcano curve is highlighted in pink and outlined in dotted lines with the position of two potent catalysts, iridium dioxide and ruthenium dioxide with saturated bridge sites and vacancies at the CUS sites. The best possible catalyst would catalyze the reaction at the horizontal dotted line indicating the equilibrium potential of 1.23 eV. Figure adapted from Rossmeisl et al. [103].

The apex of the volcano plot, known as the Sabatier maximum, is defined at the oxygen interaction energy at which the oxygen coverage is constant and the formation of the $(M - OOH_{ads})$ peroxide intermediate becomes possible [91]. This maximum illustrates the Sabatier principle, which states that the reaction rate is maximum at an optimum interaction strength of the adsorbates with the catalyst. A stronger interaction inhibits the release of the O_2 molecules and poisons the surface and a too weak interaction is indicative of an incomplete surface site coverage of the $M - O_{ads}$ and an inability to promote the formation of the peroxide intermediate [104].

This Sabatier maximum of Fig. 9 has a characteristic activity along the y axis smaller than the ideal equilibrium value of 1.23 eV (horizontal dashed line). In the AEM, there is an inherent thermodynamic impediment to the maximum activity of a catalyst coming from the observed linear scaling relationship previously discussed. Indeed, the competition between the –OH bond cleavage (step 2, Fig. 7b) and the formation of the $(M{-}OOHads)$ peroxide intermediate renders a minimum theoretical overpotential of 0.4 eV. Thus catalyzing the mechanism with an applied potential of just 1.23 V when the system is at equilibrium is considered thermodynamically unrealizable [96]. Additional energy, or driving force, is required to promote the rate and observed current of the water splitting reaction in the direction of oxygen evolution.

Lastly, it was shown that the mechanism at the apex of the volcano plot is highly dependent on the applied potential [93]. By applying an overpotential of 200 to 400 mV, Exner demonstrated the prominence of a Walden inversion mechanism, similar to the AEM with the concurrent formation of gaseous oxygen and adsorption of a water molecule in the final step of the pathway [105]. It worth noting that this inversion contributes to the degradation of rutile RuO_2 electrodes [106]. Binninger further found that at applied potentials close to the equilibrium potential, crystalline IrO_2 (110) preferentially catalyzes the OER through the availability of an Ir*OO surface entity. The active sites were found to be the oxygen atoms at the crystalline IrO_2 (110) surface, avoiding Ir–O bond breaking and justifying the evidenced stability of crystalline IrO_2 towards the OER [107]. The applied potential was further shown to affect the electrocatalytically produced current through the amount of oxidative (rather than capacitive) charge accumulated within the catalyst. This indicate a decrease in the activation free energy of the rate determining step with the amount of charge stored [108].

III.2.1.2.1 Descriptor Development.

The slope of the volcano curve, which assumes a single elementary reaction governs the rate of the reaction, has been shown to change both at the legs and at the apex of the curve as the preferred mechanism adjusts or another elementary step begins to dictate the rate [109]. These phenomena add complexity of predicting selective catalysts for the OER and CER. Adequate descriptors, such as the energetic span [110] and the electrochemical step symmetry index [111] have been developed. Utilizing heuristic tools which incorporate the overpotential into the volcano-based analysis allow to assess the performance of electrode compositions [[109),[112], [113], [114], [115]]. As previously shown, the volcano curve is resolved from calculations of the potential determining steps, which may indeed differ from the rate determining step. Exner determined that for small overpotentials the potential determining step may differ from the rate determining step and only approach the rate determining step at large overpotentials [21,112]. The descriptor $G_{max}(\eta)$ was proposed to replace the thermodynamic overpotential (η) and the use of the potential determining step as a classification for catalytic activity as it can approach the rate determining step for typical reaction conditions. The use of $G_{max}(\eta)$ can elucidate the chemical steps of a reaction pathway and can be coupled with a microkinetic approach to approximate current densities. It can resolve discrepancies in the rate determining steps of a reaction pathway with a predetermined Tafel slope [116]. Furthermore, it was shown to be an effective approach towards predicting the selectivity between the OER and peroxide formation as the effect of the applied overpotential on the surface coverage could be accounted for and an evaluation of the evolved current densities could be made [116,117].

Many other OER activity descriptors such as the e_g orbital filling of transition metal ions [118], the shifting of the redox potentials through the inductive effect of foreign metal substitution [119], the covalence of the oxygen-metal bonds [120], and structural factors such as the lattice spacing of the metal electrodes [121], the M–O–M bond angle and the ability of the crystal structure to accommodate the ion size (Goldschmidt tolerance factor) have been proposed [122]. Though if in-situ surface reconstruction induced by the OER is indeed appreciable including loss of the crystal matrix and variable densities of the electrocatalytic active sites, the utility of these descriptors may be limited [121,123].

III.2.1.3 Lattice Oxygen Oxidation Mechanism.

The lattice oxygen oxidation pathway depicted in Fig. 7c, is similar to a Mars-Van Krevelen mechanism. It has the potential to surpass the inherent limitation (scaling relationship) of the AEM by the lattice oxygen participation through direct O–O coupling in the oxygen evolution pathways. Therefore, the inevitable catalyst instability must be addressed [124,125].

Initial observation of the drastic surface reconstruction that occurs in many OER catalysts led Grimaud et al. to study the influence of the substitution of a monovalent alkaline metal in La_2LiIrO_6 perovskite. By doing this, higher Ir oxidation states are stabilized and they can prove unambiguously that the metallic t2g-like π* states are inactive for the OER [126]. Instead, the active surface sites on highly oxidized Ir-based catalysts are shown to be the lattice surface oxygen species that become more electrophilic upon oxidation. The computation of the Fukui function to render electron density maps indicated the participation of non-bonding oxygen states at the Fermi level upon Li removal and Ir oxidation, creating electrophilic oxygen radicals susceptible to nucleophilic attack by water oxygen lone pairs [126]. Grimaud et al. combined online electrochemical mass spectroscopy (OLEMS) and DFT calculations to reveal that the O_2 generated by catalytic oxides with high activity towards the OER can derive from the oxygens within the lattice [120,125,127]. Furthermore, these oxides exhibited pH dependent OER activity which indicated that the proton transfers in the OER mechanism (step 2) are nonconcerted [120,125]. This pH dependency provides a lever to increase the efficiency of water electrolysis in the electrolysers. Saveleva et al. furthermore confirmed that the generation of the electrophilic oxygen anion reactive intermediate can occur on both electrochemical iridium oxides (hydrated and amorphous) and thermally generated iridium oxides (of the crystalline rutile structure) through DFT analysis and operando studies using soft X-ray absorption spectroscopy at the O-K edge and near atmospheric pressure-XPS at the core levels of Ir 4f and O 1s [128].

III.2.2. Stability Predicament at the Anode

The LOM may affect the stability of the material and enhance its susceptibility towards degradation. Indeed, disruption of the catalytic surface was evidenced to promote dissolution. Cherevko et al. found Ru to have the highest rate of dissolution among six different noble metals including Ir indicated for acidic water electrolysis as shown in Fig. 10 [129].

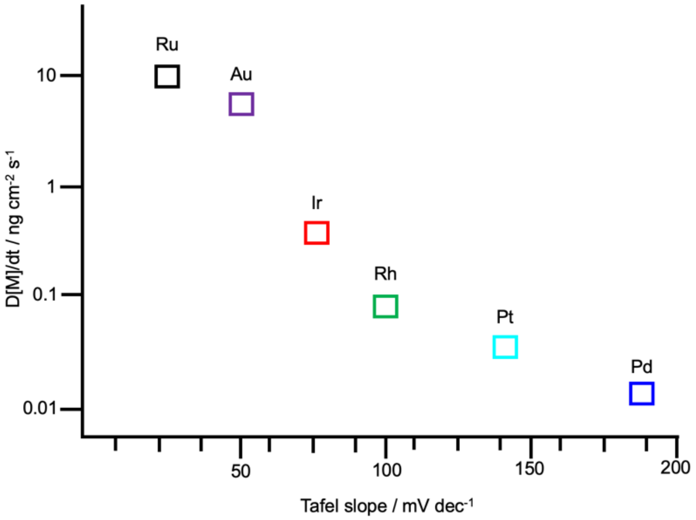

Fig. 10. A scatter plot of the dissolution rate at $j = 5$ mA cm^{-2} determined through scanning flow cell/inductively coupled plasma mass spectrometry as a function of the Tafel slope taken from ohmic drop compensate current-potential curves scanned at 2 mV s^{-1}. Reproduced from Cherevko et al. [129].

Shown in their respective Pourbaix diagrams, both the Ir and Ru metals become passivated at pH = 0 at a voltage of ~0.9 V. The IrO_2 oxide layer is further indicated to be stable up to a potential of 2 V under acidic conditions, whereas RuO_2 begins to electrochemically dissolve to volatile RuO_4 under acidic conditions at a mere 1.4 V [130]. More specifically, the intermediate specie Ru (IV) is proposed to be the substrate for oxygen evolution and corrosion reactions [131]. Both of these processes were determined by Kötz et al. to proceed towards Ru (VIII) through two single-electron transfer steps as shown in Fig. 11a, with the relative stability of Ru(VI) determining whether the Ru (VIII) corrodes or volatilizes, or dissociates to Ru (VI) [131]. Kasian et al. found the dissolution products of IrO_2 to be potential dependent as shown in Fig. 11b with the formation of Ir(V) occurring regardless of the starting electrode material and the potential [132].

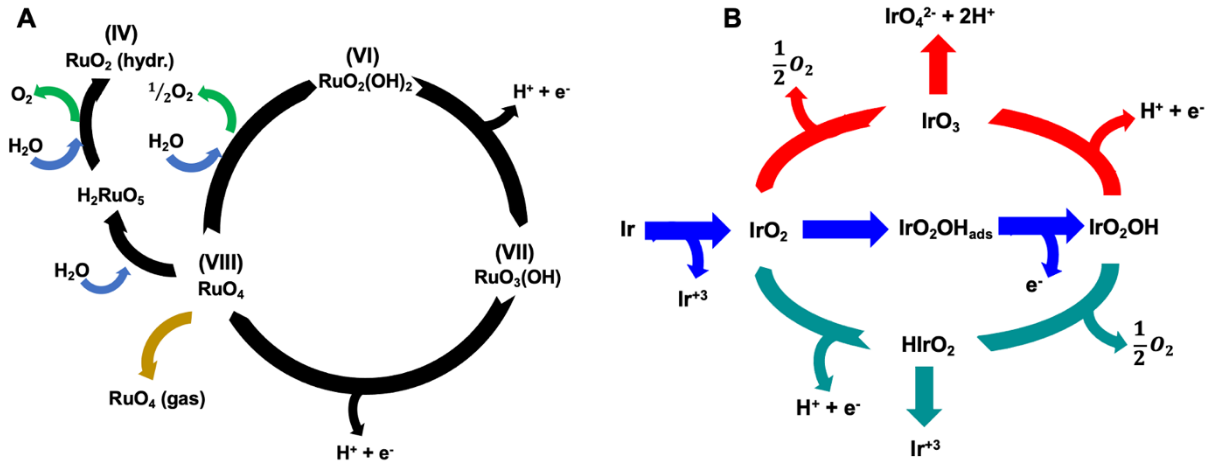

Fig. 11. (A) Depiction of the Ru metal oxidation state during the oxygen evolution and corrosion processes on Ru and RuO_2 electrodes reproduced from Kötz et al. [131] (B) Ir dissolution scheme at higher anode potentials indicated in red

arrows, at lower anode potentials indicated in green arrows. The blue arrows indicate the pathway of dissolution intermediates that occur irrespective of the potential and electrode material. Figure adapted from Kasian et al. [132].

Ir and Pt were found to have lower steady-state dissolution rates [129]. Their however higher rate of transient dissolution was proposed to be caused by the higher kinetic rate of initial iridium oxide formation. Furthermore, amorphous iridium oxides were shown to be more sensitive to transient dissolution processes though also showed a superior activity towards the OER [133,134]. This high recorded activity is thought to be independent of the increase in surface area. Evidence shown by Schweiner et.al. of O atom exchange between the oxide lattice and water of up to 2.5 nm below the catalytic surface suggests that all the atoms in these smaller particles sizes can be enabled [135,136]. Indeed, Willinger et.al found IrO_x samples with high electrochemical activity towards the OER to consist of a hollandite-like structural motif with a IrO_6 structural distortion creating a ratio between corner- and edge- sharing units; mixed Ir-oxidation states were moreover found [137]. This open three-dimensional network of short range order is proposed to encourage a redox mechanism that enables the uptake and release of oxygen atoms through the rotating corner-sharing and edge-sharing units, uninhibited by concerted motions that would be required of long-range ordered structures as shown in Fig. 12 [137].

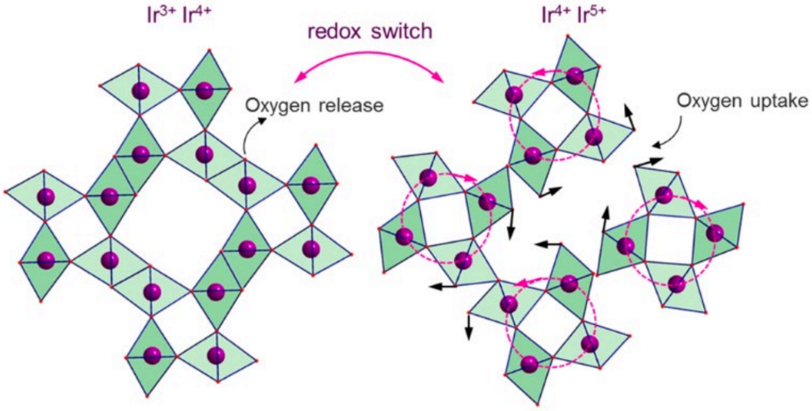

Fig. 12. Proposed redox mechanism of hollandite-like structural motifs of amorphous iridium oxides.

Mom et al. further found that amorphous iridium oxides contained more CUS sites and O-bridge sites than crystalline rutile type IrO_2 that can be deprotonated upon the application of a potential [133]. This deprotonation increases the electrophilicity of the active sites and decreases the activation barrier for O–O coupling as indicated in Fig. 13. Thus, a higher density of CUS and bridge sites in amorphous iridium oxides increase the electrochemical activity [133]. However, this activity was simultaneously shown to lower the barrier for Ir dissolution [133]. Thus strategies centered on the design of amorphous iridium oxide anodes may aid in improved selectivity between the OER and CER; however, the stability of the electrode may still be questionable.

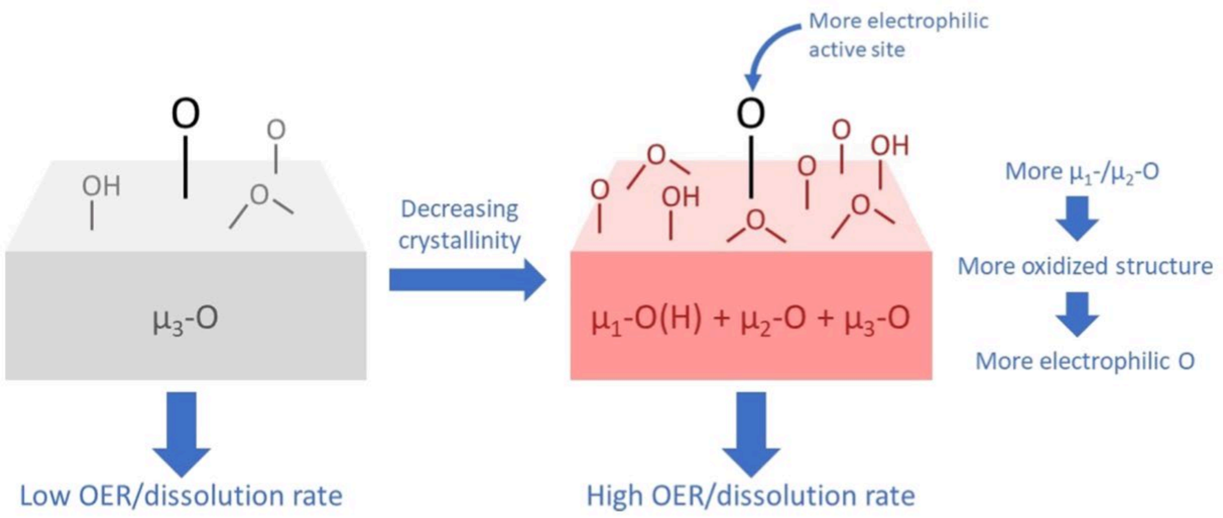

Fig. 13. Representative depiction of the adverse effect of decreasing the crystallinity of iridium oxide. Amorphous iridium oxides were shown to consist of more CUS sites (μ_1) and bridge sites (μ_2) in addition to bulk oxygen sites (μ_3) that were susceptible to deprotonation under anodic potentials, creating electrophilic oxygen atoms on the electrode surface that lowered the rate-limiting barrier for O-O coupling. Figure of Mom et al. [133].

Interestingly, Willinger et al. had found that the residual K ions localized in the large tunnels of the hollandite-like open structure of amorphous IrO$_x$ could stabilize the catalyst [137]. Thus, Xu. et al. prepared an IrO$_x$ catalyst with incorporated hydronium ions through rapid oxidation of IrCl$_3$.nH$_2$O in molten salts. It achieved negligible degradation after 8 months of hydrogen production in a three-electrode cell test in 0.1 M HClO$_4$ [138]. OLEMS with isotopic labeling further indicated that the lattice water accommodates into the IrO$_x$ framework as hydronium ions that undergo nucleophilic attack by the water adsorbed on the electrocatalytic surface at anodic potentials, initiating a modified AEM mechanism [138].

Encouraging the AEM mechanism for OER electrocatalysis may indeed improve the stabilities of the materials. Lu et al. found that the OER mechanism could be switched from AEM to LOM to AEM by manipulating the oxygen defect content of La$_x$Sr$_{1-x}$CoO$_{3-\delta}$ perovskites. They exhibit a volcano-type activity variation as the oxygen defect concentration increased [139]. The mechanistic manipulation and volcano activity variation was proposed to be caused by a concentration lockup of the generated Co^0 with increasing O vacancies. DFT simulation found this lockup to be caused by a coupling between the p and d orbitals. This coupling induces interionic pπ compensation, which can maintain the oxidation activities by the tailband of localized O-2p orbitals, and preserve the stability of the material through the transition back to the AEM mechanism [139]. A metal defect trapping technique was also utilized to synthesize Ru single atoms within the Co–O–Co skeleton of Co$_3$O$_4$. This configuration shifted the Co–O hybridized orbitals away from the Fermi level discouraging the removal of valence electrons and the activation of the lattice oxygen. In addition, the local geometry of the active centers was shifted from planar to a 3D local orientation. This change facilitates the proton transfer from the OER reaction intermediates to the bridging oxygen sites and broke the intermediate adsorption energy limitation as shown in the proposed mechanism of the study of Fig. 14 [140]. Thus, both the stability of the material was improved and an overpotential of a mere 198.5 mV under acidic conditions was required to catalyze the OER.

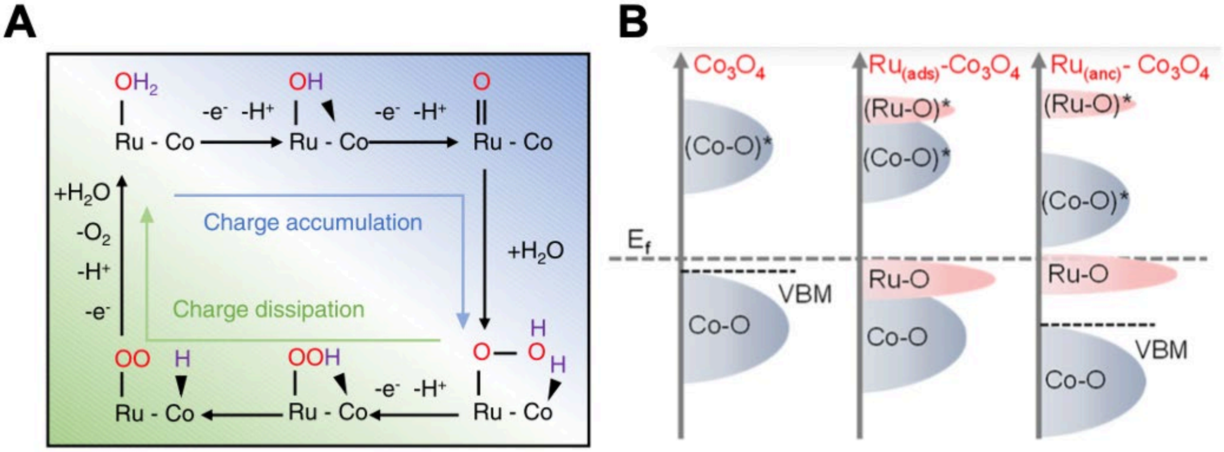

Fig. 14. (A) The proposed OER mechanism of an atomically disperse Ru atom under a lattice anchored (Ru_{anc}) steric configuration. (B) DFT calculations comparing the band centers of the Ru–O–Co system indicating downshifted Co–O hybridization in the $Ru_{(anc)}$ – Co_3O_4 steric configuration, which decreased the tendency to loose valence electrons at the Co sites and the participation of the lattice oxygen. Figure of Hao et al. [140].

III.2.3 Elucidated Mechanisms for the Chlorine Evolution Reaction

Understanding how the chlorine evolution reaction takes place was at first discussed through calculations of indirect experimental Tafel slopes and reaction orders. Three main mechanisms are reported in the literature. First, Krishtalik and Rotenberg initially deduced the mechanism for chlorine evolution shown in Fig. 15a on graphite electrodes. They proceed through the identification of a low Tafel slope on the anodic polarization curve and a first order reaction with respect to the chloride ion that created a univalent positive chlorine state. This result was later confirmed on RuO_2 and RuO_2-TiO_2 electrodes [[141], [142], [143]]. Though Janssen and Hoogland argued that the electrode doesn't behave as a porous material. Thus the electrochemical active surface area is nearly equal to its external surface area, and found the chlorine evolution pathway to follow a Volmer-Heyrovsky mechanism on a graphite anode. According to their analysis, the rate determining step should dependent on the degree of electrode aging [144]. Finally, Faita et al. found evidence for the Volmer-Tafel mechanism of Fig. 15c on an electrode made of a Pt-Ir alloy on a titanium substrate [145].

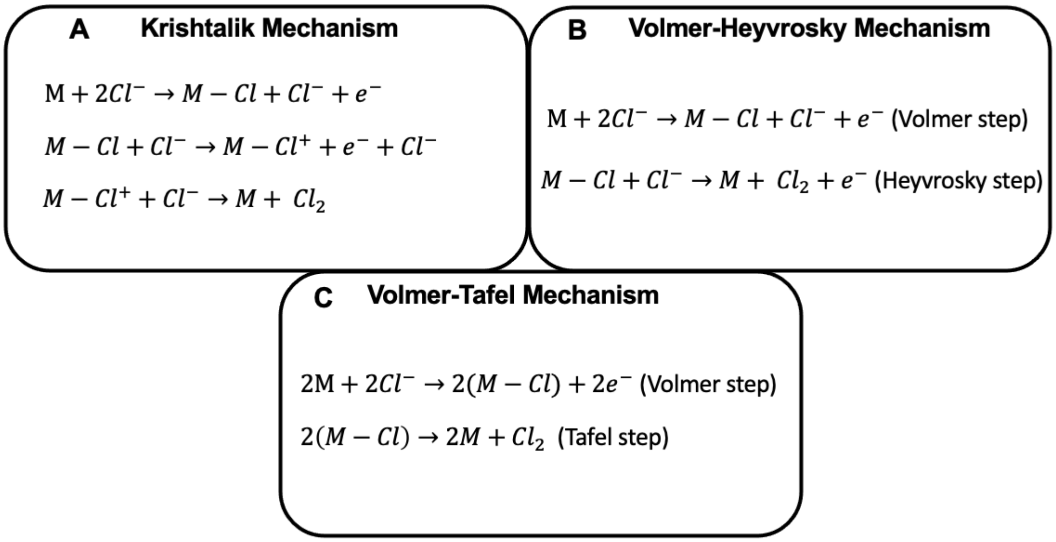

Figure 1: Classical chlorine evolution mechanisms derived by kinetic studies.

It was the discovery of the dimensionally stable anode (DSA), designed with a titanium substrate and a mixed metal oxide composed of ruthenium dioxide and titanium dioxide, that cut the energy consumed per ton of chlorine produced to nearly half [53]. Developed initially by Beer, who patented the material in 1965, these DSA anodes replaced the carbon electrodes, which are highly susceptible to corrosion under any crystalline structure or morphology ($C + 2H_2O \rightarrow CO_2 + 4H^+ + 4e^-$) [53,146,147]. Tethered with more than 50 % of the entire global chemical production turnover, brine electrolysis produces the globally demanded 90 million tons of chlorine and 100 million tons of sodium hydroxide, positioning the industry as one of the largest chemical sectors, just behind sulfuric acid and ethylene production [53]. As expected, the industry demands a large consumption of electricity to power the voltage demands required to produce the current densities for the evolution of chlorine at the anode and sodium hydroxide at the cathode. These hydrophilic anodes designed by Beer could be engineered in the form of meshes with a mud-cracking morphological pattern that enabled greater escape of gas bubbles, decreasing the inner electrode gap and the gaseous oversaturation of the inner electrode solution, reducing the ohmic drop [53,148]. Reducing the gas bubble size and the average residence time at the electrode surface also promoted deblocking of the electrode active sites; coverage of the active sites can increase the local overpotential and accelerate corrosion [53,148]. Though the actual electrocatalytic properties of the material showed only a modest improvement over the electrocatalytic properties of the carbon electrode that was due to their powder-like consistency, which increased the surface area and roughness factor [148]. It is the versatile nature of these highly conductive, active oxides that promote their potentiality and robustness towards decreasing the activation energies of critical electrochemical reactions [148].

IV. Facilitating the Electrocatalytic Performance at the Anode

Enhancing the selectivity of seawater electrolysis with appreciable faradic efficiencies for oxygen and hydrogen evolution is convoluted by the multifarious complexity of the competition between CER and OER at the anode. Beginning to unravel that complexity enables strategies to be designed that break the scaling relationships select for the most active facet of the electrocatalyst, modulate the electrocatalytic surfaces with substitutions and vacancies, and augment the conductivity. Incorporating filtration approaches and taking inspiration from the observed self-healing properties of molecular electrocatalysts may lead to a heterogeneous electrocatalysts with a characteristic penchant for OER selectivity crucially needed to utilize the abundancy of seawater reserves to generate the hydrogen energy carrier.

IV.1 OER vs. CER Mechanistic Competition

Usually in brine electrolysis, the oxygen evolution reaction is considered a parasitic side reaction hampering the selectivity for the chlorine evolution reaction at the DSA rutile-type anodes [149]. Under the aqueous NaCl or HCl conditions, the surface of the electrode can interact with water, chloride ions, or other ionic constituents of the electrolyte solution. Within the potential region of the chlorine evolution reaction that occurs beginning at 1.36 V, there is a strong occurrence for the oxidation of water considering that the reversible voltage of water begins at 1.23 V. In further considering this contention by examining the adsorbate evolution mechanism for the OER, two electrons are transferred to form the adsorbed oxygen species whereas only one electron is transferred to form a chlorine intermediate. Thus the energy gained ($= zeE$) for the adsorption of oxygen is double the energy gained for the adsorption of a chlorine intermediate. Therefore thermodynamics dictates that the electrode surface is effectively covered with the $M - O_{ads}$ adsorbate under the potentials at which chlorine begins to evolve [150].

Trasatti conjectured that the chloride ion adsorbed onto the surface by binding the same single oxygen species ($M - O_{ads}$). The slope of unity in the graph of Fig. 16 indicates that the AEM ($-OH_{ads}$) adsorbate of the OER and the (-Cl) adsorbate of CER bind the catalytic surface through the same $M - O_{ads}$ atom. Indeed each of these adsorbates adsorb onto the $M - O_{ads}$ populating the surface with a one-to-one linear correlation [89,151]. Thus Trasatti observed that good oxygen evolving catalysts were also chlorine evolving catalysts. Trasatti also revealed that an additional overpotential is required for those catalysts to catalyze the oxygen evolution reaction [151]. This overpotential comparison indicates that the prevalent mechanism on these catalysts is indeed the AEM.

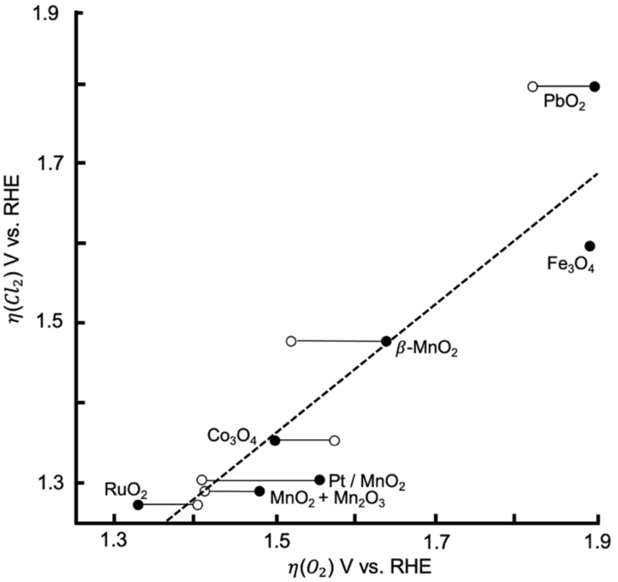

Fig. 16. Plot of the overpotential for chlorine evolution against the overpotential for oxygen evolution recorded for various oxides at the same current density in acidic solution (•) and basic solutions (O). Figure adapted from Trasatti et al. [151].

The initial density functional theory (DFT) studies to elucidate the potential, pH regions, chloride concentrations, and electrode materials in which this O_{ads} species was adsorbed on the electrode surface were conducted by Hansen et. al.. They analyzed the surface structure and the activity trends underlying the electrocatalysis of chlorine evolution over rutile oxides [152]. Further considerations for the effects of the solvent, the bridging lattice oxygen atoms, and the uncertainties of the DFT calculations were also studied [115, 153, 154]. The unit cell surface consisted of two bridge sites (^{b}) and two CUS sites (^{c}) and the adsorbates were found to strongly bind the bridge sites. Thus the adsorbate binding stabilities at the CUS sites were probed. It was assumed that the activation energies (E_A) of the reactions were linearly correlated to the reaction chemisorption energies ($\Delta\epsilon$) as previously described. It was found that adsorption of the CER adsorbates directly onto the CUS sites required a pH < -3 and formation of CER adsorbates directly on the bridge sites required an even lower pH [98, 152]. Plots of the Cl^c and ClO^c chemisorption energies against the O^c_{ads} chemisorption energies showed a similar trend seen in the plot of Fig. 16 and thus indicated that the chemisorption energies are linearly correlated. This phenomenon was thought to be caused by the identical valency of one found in both the chloride species and the oxygen atom of the hydroxide adsorbate precursor. Thus, a plot of the potential against the O_{ads} binding energy was generated and depicts the potential and O_{ads} chemisorption energy regions in which the most stable adsorbates can be found on the surface, as shown in Fig. 17. The three Sabatier volcano curves indicate chlorine evolution through the mechanistic pathway consisting of the ClO^C, the $Cl(O^c)_2$, or the Cl^c intermediates. The blue line represents a combined Sabatier volcano that takes the stability of the initial adsorbate on the surface into account; the intermediate is only expected to form at active sites that are indeed stable and abundant.

The three metal oxides indicated in Fig. 17 each bind to the O^c_{ads} with a different binding energy and thus stabilize a different adsorbate and a different chlorine intermediate. Along the surface of IrO$_2$, the O^c_{ads} initiates the formation of the ClO^c

intermediate, which was further determined to follow a Volmer-Heyrovsky mechanism [152,155,156].

$$O^{c}_{ads} + 2Cl^{-}(aq) \rightarrow ClO^{c} + Cl^{-} + e^{-} \rightarrow O^{c}_{ads} + Cl_2(g) + 2e^{-} \tag{17}$$

Along the RuO_2 (110) surface, the most stable adsorbate populating the CUS sites in the potential regions of chlorine evolution is the O_2^{cc} adsorbate, enabling the formation of the chlorine intermediate through the Krishtalik mechanism [152].

$$O_2^{cc} + 2Cl^{-}(aq) \rightarrow Cl(O^{c})_2 + Cl^{-}(aq) + e^{-} \rightarrow O^{c} + Cl_2(g) + 2e^{-} \tag{18}$$

This analysis indicates that chlorine will evolve on IrO_2 and RuO_2 through the formed ClO^{c} and the $Cl(O^{c})_2$ intermediates at the CUS sites. Exner et. al. later proposed however that the ClO^{c} adsorbate is also indeed the precursor for the CER on RuO_2 (110) [153]. When the combined Sabatier volcano curve for the chlorine evolution of Fig. 17 *(Blue Curve)* is compared to the Sabatier volcano curve for oxygen evolution, as shown in Fig. 17 *(Green Curve)*, it is apparent that in accordance with the initial work by Trasatti, the CER will evolve at lower potentials than the oxygen evolution reaction on oxides with characteristic oxygen chemisorption energies. The CER occurs through a single intermediate, and thus the mechanism isn’t subjected to the linear scaling relationships between the three intermediates inherent in the OER undergoing the AEM. Moreover, CER selectivity is highly favored under conditions in which the Cl^{c} intermediate, rather than the ClO^{c} intermediate is formed at the rutile surface, even in only slightly acidic or even neutral pH conditions [155].

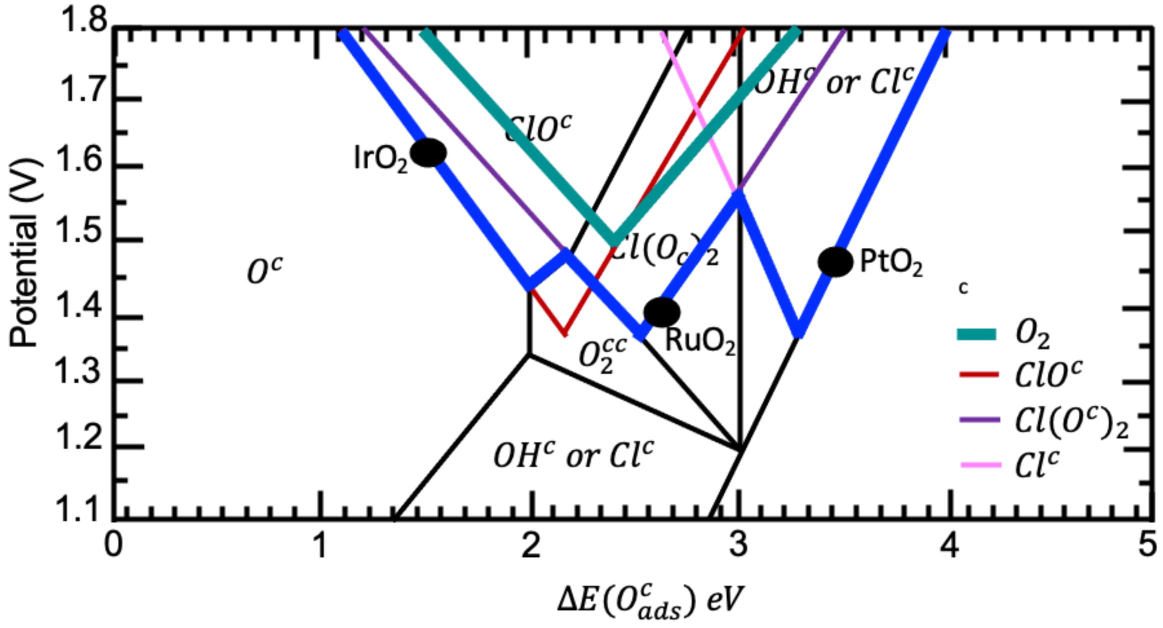

Fig. 2: (Blue Curve) Combined Sabatier volcano curve that indicates the most stable adsorbate and formed intermediate at a given O_{ads} binding energy and potential at pH = 0 and $a_{Cl^-} = 1$. (Green Curve) The Sabatier volcano for the OER indicating that greater potentials are required to catalyze the reaction along IrO_2, RuO_2, and PtO_2. Reproduced from Hansen et al. [152].

IV.1.1 Confronting Competitive Adsorption

Vos et al. indicated that the OER reaction is suppressed in the presence of chloride ions through competitive adsorption and active site blocking [55]. Graphs in solutions showed decreasing OER activity as the concentration of the chloride ion (and the bromide ion) increased as shown in Fig. 18. The CER was further found to proceed through the Volmer-Heyrovsky mechanism, similar to the Rideal-Eley mechanism for gaseous reagents.

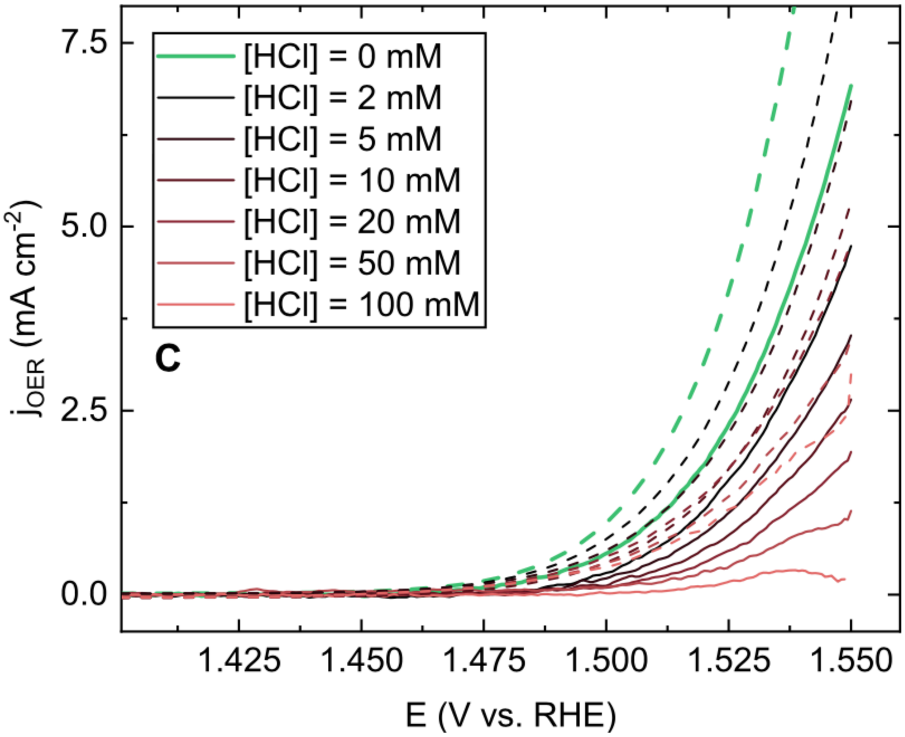

Fig. 18. OER current density as a function of potential vs. RHE in the presence of bromide (solid curves) and without bromide (dashed curves) at increasing chloride ion concentrations. Figure of Vos. et al. [55].

If a Langmuir adsorption model with a lack of lateral interactions among adsorption sites is assumed, the surface coverage of water at the active sites is thus expected to diminish in the presence of the chloride ion, though its presence at an approximately consistent concentration enables a small amount of oxygen to form, at the dismay of the chloro-alkali industry. Therefore, improving the selectivity at the anode is an inevitable challenge.

IV.1.2 Identifying the Rate Determining Step

Efforts have been proposed to develop new electrocatalysts that maximize the free energy difference between the respective CER and OER intermediates. With the assumption of quasi-equilibrium of the reaction intermediates preceding the rate determining step in place, the free energies of the transition states corresponding to the rate determining step can be found, enabling the rate determining step to be identified [150,157]. With the desire to discover an electrocatalyst that stabilizes the oxygen transition state, the intrinsic catalytic characteristics of an electrocatalyst may be regarded through measurements of the exchange current density. Exner et.al. proposed that the linear regions of the Tafel plot may each be extrapolated to $\eta = 0$ to measure the exchange current densities. They could then be utilized in the generalized Butler-Volmer equations discussed by Parsons to determine the free energy of the corresponding transition state, enabling the rate determining step to be determined with respect to the overpotential applied [150,158].

The free energies of the reaction intermediates must be determined to enable a critical assessment of the intermediates and transitions states to stabilize and thus promote CER or OER selectivity. Quasi-equilibrium implies inaccessible values of reaction intermediates free energies. Though, advancement of transient experiments like cyclic voltammetry [159] and operando spectroscopic methods [160] can aid in their identification. However, with small surface area coverages due to their higher Gibbs Free energies, in-situ intermediate detection is generally difficult. A particular attention should be made to verify the reaction intermediates and their corresponding free energies determined through DFT theory and the construction of ab initio surface Pourbaix diagrams. The free energies in function of potential of reaction intermediates can be *ab initio* calculated and correlated with the respective free energies of their transition states determined through the Tafel plots. This work enables a free energy surface model of an electrocatalyzed reaction to be deduced and the dependence of the free energies of the transition states and reaction intermediates on the overpotential to be depicted. Understanding the characteristic rate determining step of a designed electrocatalyst with respect to the overpotential could enable optimization of an electrocatalyst that, for instance, stabilizes the $(M - OOH_{ads})$ transition states, making the OER the kinetic product by increasing the speed of the reaction step as delineated in Fig. 19 [161].

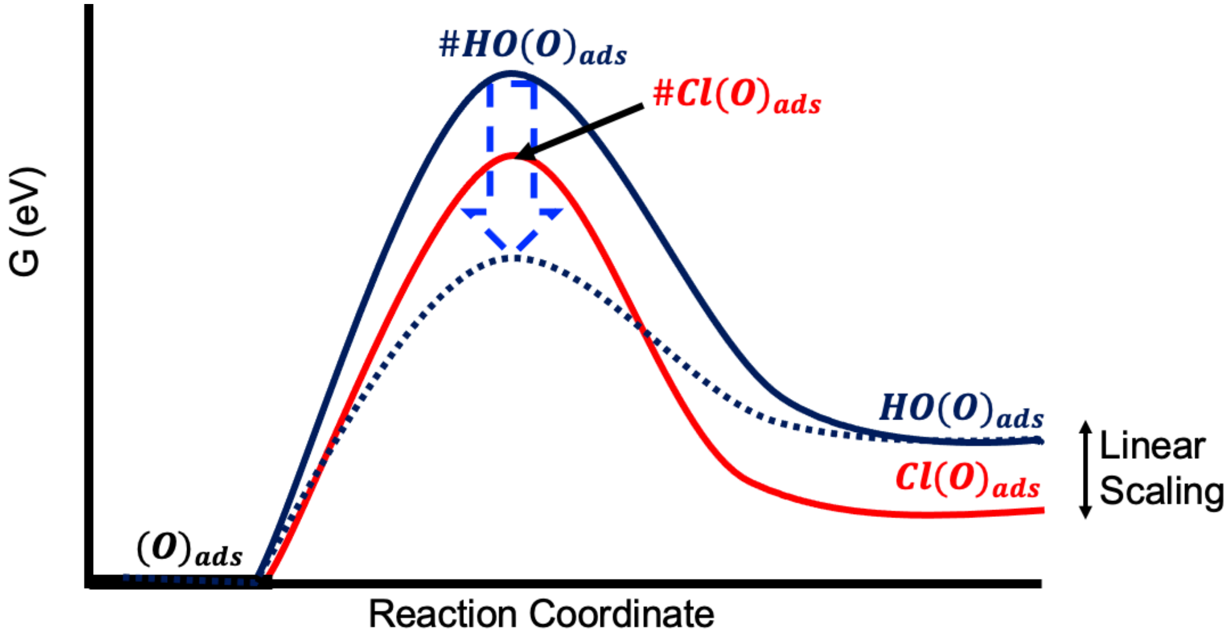

Fig. 3: The free energy diagram along the reaction coordinate of the OER and the CER over a single-crystalline RuO_2 (110) electrode at $\eta_{CER} > 0.1$ V and constant pH indicating the relative energies of the transition states (#) of the rate limiting steps for the OER and CER. The thermodynamic stabilities of the $\mathrm{HO(O)_{abs}}$ and the $\mathrm{Cl(O)_{abs}}$ intermediates are determined by the linear scaling relationships. Figure adapted from Exner [162].

IV.2. Modulating the Structure of the Electrocatalyst

Initial thoughts by Taylor implicated that unsaturation within an active site at the atomic level can control surface reactivity [163]. Refinement of the local structure can optimize the functionality of the active site. A challenge of heterogenous electrocatalysis is maximizing the exposed active sites and enhancing their intrinsic mass activity by stabilizing the transition state while maintaining stability. Refining the size and the dispersion, and moreover the crystal facet orientation, has been shown to improve the amount of exposed active sites [164]. Moreover, dispersing the active centers among various types of substrates such as metal oxides [165], metals sulfides [166], and carbons [167] can influence the ionic and electronic defects within the material and encourage electron transfer capabilities of the active centers, manipulating the valence of the active site and the coordinating bond lengths [168]. These refinements can influence the stability of the intermediates and the activation energies of the transition states electronically, geometrically, and through confinement effects enabling selective seawater electrolysis to be achieved [169,170] (Fig. 20).

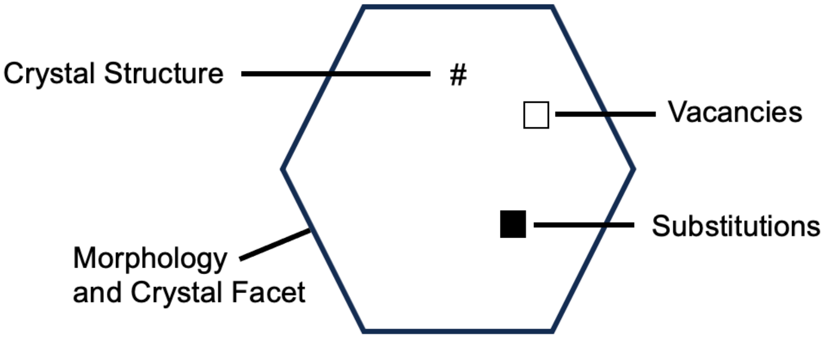

Fig. 20. Means of manipulating the active site to improve the activity and selectively of the electrocatalyst.

IV.2.1. Manipulating the Morphology and Crystal Facet

The D-band centers of late transition metals with low coordination numbers, consisting of edges, steps, and kinks are thought to be more diffuse, residing further from the nucleus and interacting more strongly with adsorbates than metal atoms on close packed surfaces with higher metal coordination numbers and more compact, tightly-bound d-states [169]. Dickens and Norskov projected the density of states onto an Ru atom CUS-terminated single kink site along the (110) plane and found shifted d-band centers with significant higher energies, which result in less filling of the Ru–O adsorbate antibonding states and a stronger Ru–O adsorbate bond, promoting the OER [171]. Indeed, the structure of the catalytic surface has been shown to affect the catalytic activity of the material towards the OER through a linear correlation with the density of coordinatively undersaturated metal sites (CUS) along each crystallographic face [172]. The (100) facet of epitaxial grown RuO_2 supported on a single crystal (001) facet of $SrTiO_2$ was found to more easily oxide the reagent substrate than the corresponding (110) facet in a basic 0.1 M KOH solution as shown in Fig. 21. Measurements of the cathodic pseudocapacitive charge further enabled a charge ratio between the two surfaces to be determined that was found to mimic the CUS ratio between the two facets [172].

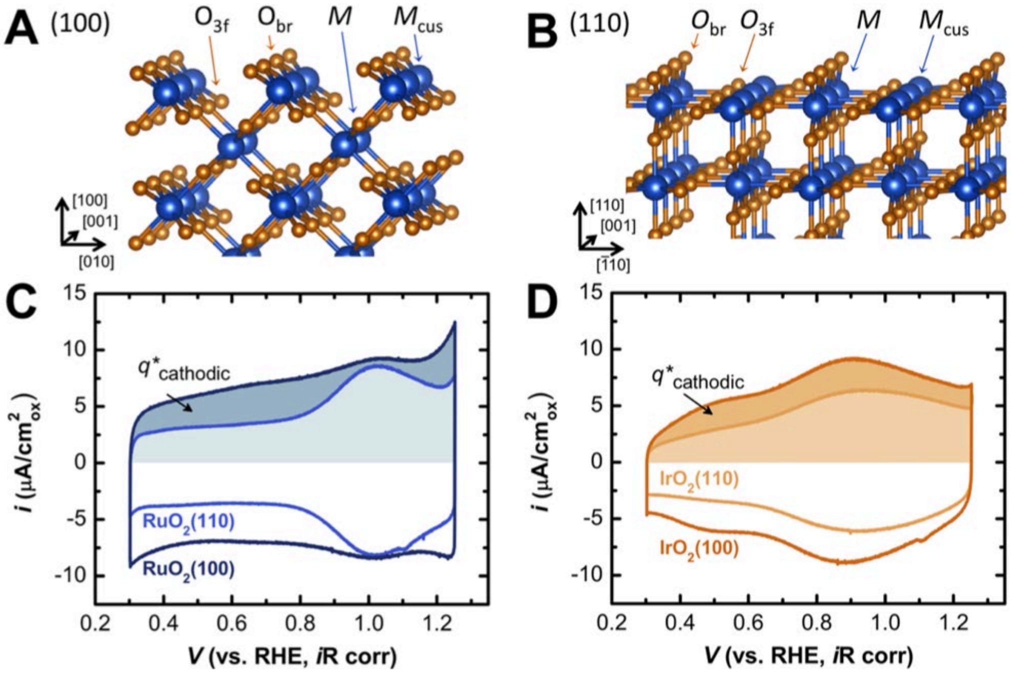

Fig. 4: (A) Schematic depiction of the (100) facet and (B) the (110) facet of RuO_2 and IrO_2. Fully coordinated metal centers (M) and coordinately undersaturated metal sites (M_{cus}) are indicated in blue, bridging oxygens (O_{br}) and three-fold coordinated oxygen (O_{3f}) are shown in orange. Analysis of the pseudocapacitive charge ($q^*_{cathodic}$) shown in (C) and (D) for RuO_2 and IrO_2 gave an indication of the electrochemically active metal site density on the electrode surface, the ratio of the calculated charge between each orientation indicating the undercoordinated metal site density. Figure of Stoerzinger et al. [172].

The stepped nature of the (230) facet of RuO_2 was further proposed to explain the greater Cl^-evolution; the (230) facet possesses an activity with a greater susceptibility to changes in the pH because of the abundant pre-oxidation occurring through proton removal of the hydroxide adsorbates along the surface active sites [173,174]. This (230) surface was indeed proposed to be more hydrophilic, possibly due to its unique binding energies with the –H_2O and –OH adsorbates, enabling different degrees of hydrogen bonding amongst the adsorbate groups along the surface [175]. The mechanism of chlorine evolution was further proposed to proceed without pre-oxidation on more hydrophobic surfaces such as the (100) facet with less local functional group motion that facilitates proton exchange [173]. Facilitating proton exchange may indeed be more facile on faceted surfaces. Adiga et al. epitaxially grew a (101) surface of RuO_2 on r-Al_2O_3 and TiO_2 substrates, a surface which is known to possess a large degree of strain due to the large lattice mismatch between the film and the substrate [176]. This strain was shown to relax as the film thickness increased through the introduction of facets and defect formation. This faceting was shown to dramatically decrease the activity towards the OER, which was shown to be perpetuated through the LOM evidenced by exposing the thicker films to solutions of varying pH, the AEM mechanism is conjectured to independent of solution pH due to the proposed concerted proton-electron transfers. Interestingly, the CER activity was minimally affected. Strain relaxation and the resulting faceting may thus induce a mechanistic change in the OER [176]. The study moreover found the thicker films to be more selective for the CER.

Indeed, mitigating the elucidated mechanisms of the CER and the OER to select for one evolved product is convoluted by the disparities between the single intermediate and the multiple intermediate reactions. Interpretation of the most thermodynamically stable intermediate, initially addressed by the DFT studies by Hansen et al. has aided in the utilization of potential and pH manipulations to promote the evolution of the CER or the OER [152]. Fig. 22 highlights the potential and pH conditions that promote the evolution of the CER or the OER.

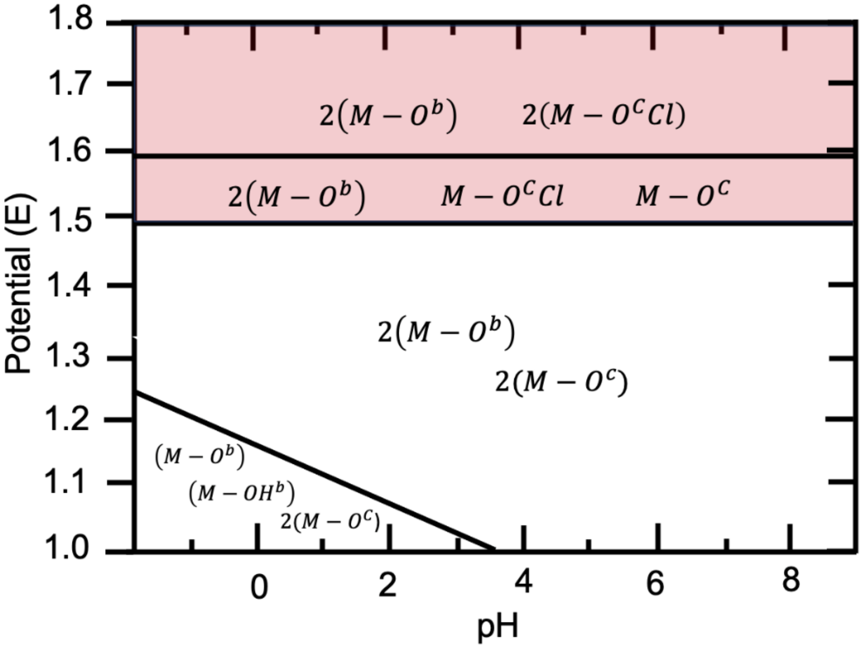

Fig. 22. Pourbaix diagram depicting the most stable adsorbates along the RuO_2 (110) catalytic surface corrected for solvent effects at Activity Cl^-= 1. Denoted adsorbate structures were further found to be stable with respect to the gas phase molecular species. Potential and pH regions highlighted in red indicate the conditions promoting the CER; the $2(M-O^b)+2(M-O^C)$ structure is expected to serve as the catalytic active phase for the OER. Figure reproduced from Exner et al. [153].

However, with the high current densities afforded by PEM electrolysers, achieving OER selectivity under acidic conditions is critical, requiring surface engineering that controls the nature and abundance of the active sites that catalyze the desired reaction. Saha et al. utilized ab-initio studies to further find the (101) and the (001) to be the most selective facets at pH = 0 along RuO_2 for the CER and the OER, respectively [98]. The difference in selectivity was attributed to the variation in the adsorption energies of the CER and OER intermediates along each facet, which is caused by the disparities in the ligand coordination symmetry around each active site that affects the charge distribution and the bond length between the adsorbate and active site [98,177].

IV.2.2. Introducing Point Defects into the Local Chemical Environment

IV.2.2.1. Lattice Substitution.

Exner et al. found in an ab initio thermodynamic study that the activity towards the OER could be improved by 0.8 to 1.0 eV by reducing the adsorption energy of oxygen to the catalytic Ru_{cus} when the ruthenium atoms of the second coordination shell were substituted by Ir or Cr [177]. To further their investigation of the OER vs. CER selectivity, Exner et al. found in another study that replacement of the top most monolayer of RuO_2 (110) with TiO_2 improved the CER selectivity by adjusting the bonding strength of the oxygen to optimize the strength of the chloride adsorption in the Heyrovsky step [178]. Karlsson et al. found that monolayers of TiO_2 on RuO_2 improved selectivity for the CER while maintaining the characteristically high activity of pure RuO_2, and that by moreover doping TiO_2 with Ru, the Ti_{CUS} sites could be activated with optimal oxygen adsorption descriptor values for active and selective chlorine evolution [179]. Ru has been indeed proposed to influence the electronic state of TiO_2 [180]. Deactivation of DSA electrodes was further noted by Karlsson et al. to be caused by the removal of Ru from the surface [179,181]. Macounová et al. went one step further to employ a systematic study of spray freeze drying prepared nanocrystalline $Ru_{1-x}Ti_xO_2$ ($0 < x < 0.2$) in chloride containing acidic media to dissect the ambiguity surrounding the compositional roles of these catalysts within DSA electrodes [182]. The authors found the selectivity towards the CER to increase with greater Ti content that relieves Ti clustering along the *z* axis and promotes Ti–Ti pairing between CUS and bridge sites, as shown when comparing Fig. 23a and c; these structural shifts were furthermore indicated to cause an increased oxygen deficiency within the Ti environment [182]. Moreover, this increased oxygen deficiency was indicated to promote the LOM, as evident in the comparison of Fig. 23b and d. Thus, the variability in the chlorine selectivity was ascribed to the differences in the mechanisms used by the catalyst to evolve oxygen, with catalytic structures that promote the LOM having an increased selectivity for the CER [182].

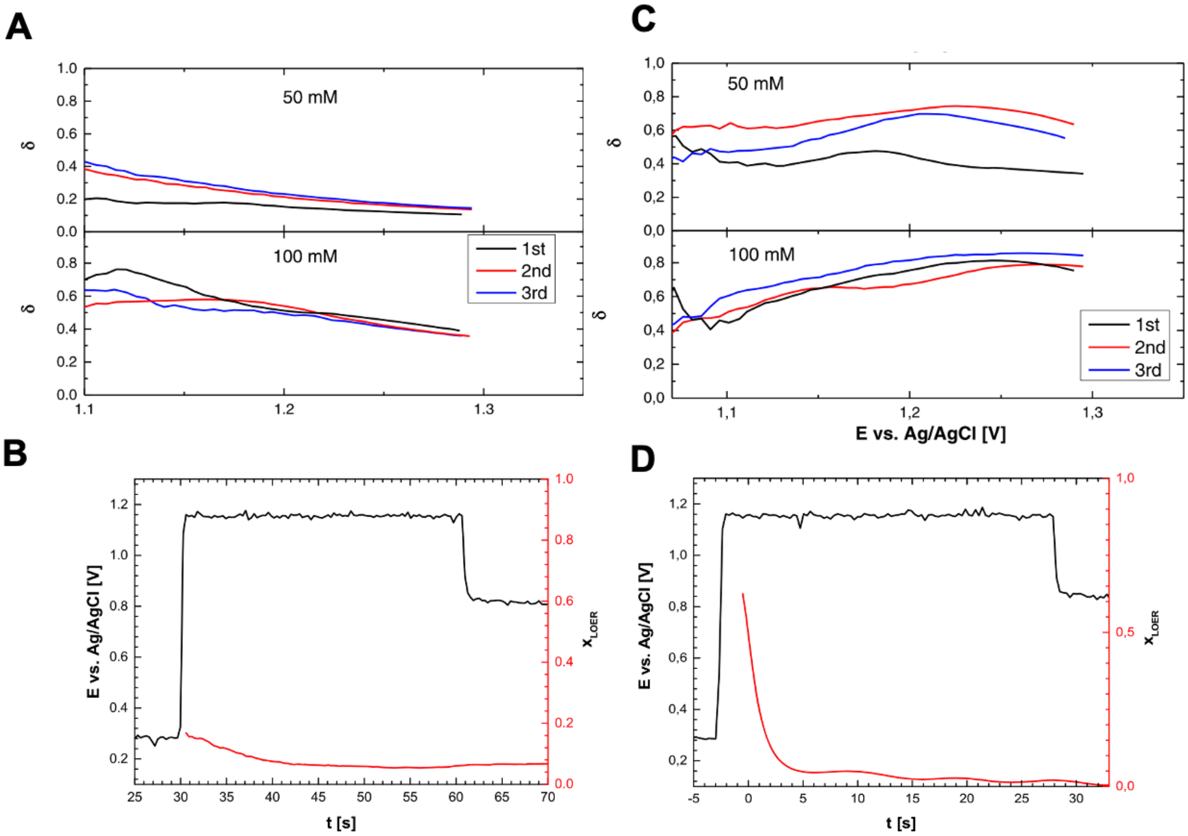

Fig. 5: (A) and (B) represent the selectivity (δ) towards chlorine evolution and the tendency to evolve oxygen via the LOM determined through differential electrochemical mass spectrometry isotopic labeling for $Ru_{0.95}Ti_{0.05}O_2$. (C) and (D) represent the results obtain for the structural composition $Ru_{0.80}Ti_{0.20}O_2$. Figure of Macounová et al. [182].

In another study, Astudillo et al. found through detection by differential electrochemical mass spectroscopy that the LOM in acidic, chloride containing aqueous solutions electrocatalyzed by Ru–Mn–O oxides coincided with greater CER selectivity [183]. However, ab-initio studies indicated that an Ru–Mn–O surface behaves similarly to pure RuO_2 surface in that the adsorption of oxygen into any conceivable surface site is unlikely to result in its immobilization that promotes the LOM: the surfaces are rendered too stable [183]. The binding of oxygen adsorbates at the Mn_{cus} sites was however found to be weaker, which may promote the migration of a proton towards the bridge sites for the –OH and –OOH reaction intermediates, and explain the observed experimental trend of higher OER activity with increasing Mn content [183,184]. However, it must be noted that spectroscopic confirmation of the CUS and bridge sites in the prepared Ru–Mn–O oxides remained elusive throughout the study and low dimensionality sites, such as crystal edges and vertices, were mentioned by the authors to not be taken into account, which may indeed influence the perceived mechanism of the OER and an understanding of the observed selectivity [176].

Interestingly, substituting RuO_2 materials with Zn was found to increase selectivity towards the OER at more positive potentials [185]. The authors suggested that the substitution resulted in rearrangement of the metal atoms along the [111] that created more oxygen vacancies on the surface that affected the adsorbate binding of the chlorine evolution precursors and enhanced the oxygen evolution via the LOM at more positive potentials [185]. However, the chemical constituent which is substituted into the lattice may affect the OER mechanism. An overpotential of 214 mV was achieved by Wu et al. who incorporated Ni into the RuO_2 lattice; DFT studies and operando electrochemical mass spectrometry analysis indicated that the Ni replaced Ru in the bridge sites, which both stabilized the lattice oxygen and promoted the AEM mechanism while achieving impressive stabilities of >1000 h under a current density of 200 mA/cm^2 [186]. Interestingly, the oxidation state of the Ru catalyst with Ni embedment was shown through X-ray photoelectron spectroscopy to be slightly up-shifted compared to RuO_2; higher Ru oxidation states have been shown to enhance OER electrocatalysis [187]. Moreover, the number of dopants on the electrocatalytic surface may affect the OER mechanism that predominates. Zagalskaya and Alexandrov found that substituting the surface of RiO_2 (110) with only two nickel atoms wasn't enough to induce a mechanistic shift from the AEM to the LOM [188]. The formation of metal vacancies that were caused by catalyst dissolution were further proposed to have a synergistic effect with the introduced dopants to lower the OER overpotential via the LOM [188]. Zagalskaya and Alexandrov further found defective IrO_2 to be less LOM active than defective RuO_2 through simulations suggesting that by creating two surface vacancies in the high energy 211 facets of RuO_2 and IrO_2, the mechanism could be switched from AEM to LOM in RuO_2 though not in IrO_2, indicative of the greater structural stability of IrO_2 under OER conditions [188].

IV.2.2.2. Generating Vacancies within the Lattice.

Incorporating the Ru into a mixed metal oxide such as the pyrochlore $Pb_2Ru_2O_{7-x}$ structure increased the concentration Ru(V) indicated through XPS measurements and was further shown to improve its stability even after being subjected to a 2 h stability test in alkaline conditions [189]. The high Ru oxidation state and high concentration of oxygen vacancies characteristically present in pyrochlore $A_2B_2O_{7-x}$ structures that form upon a cationic radii mismatch of >1.46 was proposed to promote an improvement in the activity and selectively towards the OER during simulated seawater electrolysis under alkaline conditions [[190], [191], [192], [193]]. Oxygen vacancies shifted the O-2p orbitals upwards, increasing the density of states around the Fermi level and promoting both metallic character and potential interaction with AEM adsorbates [190]. Another means of generating vacancies within the lattice is through leaching. Though deemed thermodynamically unstable under acidic conditions and prone to dissolution through cation A-site leaching according to in-situ Pourbaix analysis, an increase in electrocatalytic activity with A-site dissolution was found for Ru incorporated into $A_2Ru_2O_7$ (A = Y, Nd, Gd, Bi) pyrochlores [194]. Weaker interactions between the Ru 4d and O 2p orbitals of the OER intermediates of the AEM with longer Ru–O bond lengths were shown to improve activity in the materials when compared to RuO_2 [194]. This increase in activity was shown to be correlated with both the increase in the density of Ru active sites promoted by leaching and an increase in the oxygen 2p-state energy for adsorbed oxygen density of states, as shown in Fig. 24 [194]. Moreover, the bulk phase of $Y_2Ru_2O_7$ was shown to be maintained after chronoamperometry testing by XRD and also that the surfaces evolves during OER catalysis [194]. The surface coverage of the active sites is indeed critical. Gayen et al. found the apparent OER activity of $Pb_2Ru_2O_{7-x}$ pyrochlores to decrease upon being subjected to annealing at elevated temperatures regardless of the annealing environment; this effect was attributed to the observed increase in crystallinity that lowered the density of under-coordinated active sites, which decreased their surface coverage on the catalytic surface [189].

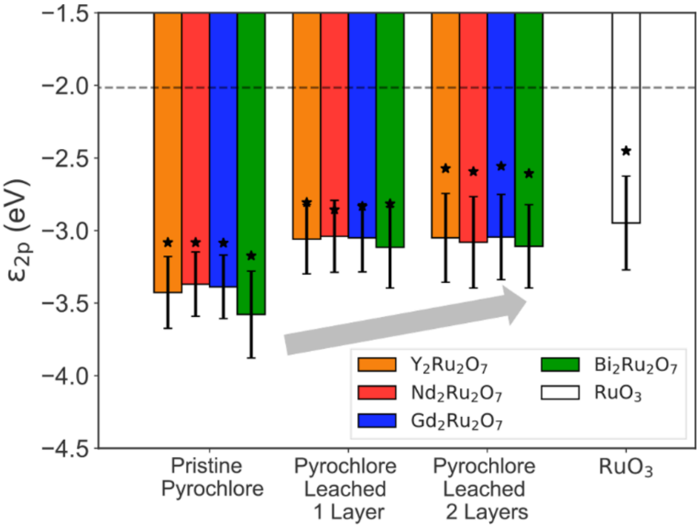

Fig. 24. Computed oxygen 2p-state energy comparison of pristine pyrochlore, one and two layer leached pyrochlore, and the fully leached pyrochlore-like RuO_3 structure, showing an increasing trend that approaches the computationally determined optimal OER activity value of −2.0 eV shown by the dashed line. Figure of Hubert et al. [194].

Nong et al. also found that leaching nickel from their IrNi@IrO_x core-shell nanoparticles could achieve uniquely high activities in OER electrocatalysis [195]. The leaching produced significantly shorted Ir–O bond lengths at the shell surface with a covalent character that created electrophilic oxygens, highly conductive and more susceptible to the nucleophilic attack inherent in the O–O bond formation of the LOM mechanism as shown in Fig. 25b. Conclusions from XANES measurements indicated that the iridium atoms adjacent to the vacancies formed through nickel leaching had a greater number of d-band holes. Moreover, the occupied projected density of states indicated that the iridium 5d-states were concomitantly lowered below the oxygen 2p states, producing oxygen hole formation, with significant Ir character, that was reflected by the appearance of an unoccupied, narrow band just above the Fermi level [195].

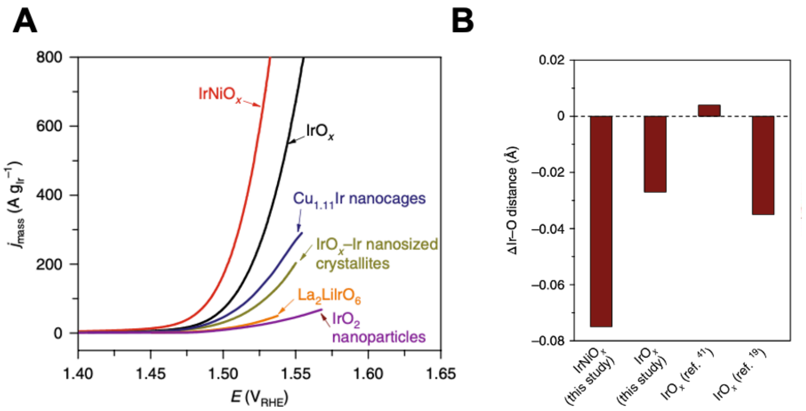

Fig. 25. (A) Comparison of the activity towards the OER in an acidic electrolyte amongst the investigated IrNi@IrO_x, the benchmark IrO_2, and electrocatalysts of high recorded intrinsic activity divulged from the literature. (B) Degree of change in the Ir–O bond length along the surface of the IrNi@IrO_x nanoparticles, IrO_x nanoparticles, an IrO_x film, and standard IrO_x nanoparticles. Figure of Nong et.al. [195].

IV.2.3. Use of Single-Atom Catalysts

The number and type of atoms within the first and second coordination shell can significantly affect the local geometry and charge density of the metal active sites [196] Ji. et al. incorporated Ru atoms into a low crystallinity 2D TiO_x substrate that promoted sub-nano ruthenium clusters through a cationic defect adsorption-oxidation anchoring method, creating partially oxidized, high valence, and lowly coordinated ruthenium atoms [197]. DFT simulations predicted that the CER proceeded through stabilization of the –Cl adsorbate by the ruthenium clusters, similar to the results of Lu et al. discussed above, avoiding the –OCl intermediate and improving the mass activity, selectivity, and stability towards the CER [197]. Though, the close-packed geometries adopted by these supported metallic cluster/nanoparticles may limit, as previously indicated, their achievable activities and desired selectivities [198].

Embedding a metal atom with a heteroatom support as in the case of single-atom catalysts (SACs) or amongst adjacent metal atoms, known as correlated SACs (c-SACs) may provide greater flexibilities in the structural design to tune the atomic structure and the local coordination of the active site to achieve optimal electronic structures for selective adsorbate binding with high activities and verified stability [164,198]. Cho et al. identified the critical role of the three-coordinated Pt^{II} with broken D_{4h} symmetry in a platinum single atom catalyst with reported CER selectivities approaching 100 % under acidic conditions [199]. It must however be understood that the study illustrated the significant degree of heterogeneity present at the active sites of SACs and the complexity of discriminating the authentic active sites and the quantifying the intrinsic activity of the catalysts through metrics such as the turnover frequency (TOF) [199]. These lowly coordinated active sites were deemed more active in the CER than the Pt-N_4 sites previously reported with a preferential binding of the –OCl intermediate [199,200]. On the other hand, the design and successful synthesis of single atoms that exhibit spatial correlation within a sublattice substrate have the potential to exhibit identical structural motifs within those substrates. Accommodating iridium single atoms into the cationic sites of a cobalt spinel oxide through an ion exchange-pyrolysis procedure produced Ir sites that were shown to possess short range order though the partial projected pair distribution function profiles derived from multiple high-angle annular dark field scanning high resolution transmission electron microscopy (HAADF-HRSTEM) images [201,202]. These Ir cluster sites exhibited a spatial correlation with the Co_3O_4 host lattice with the majority of the Ir sites exhibiting short range order rather than being isolated within the cationic lattice of the Co_3O_4 [201]. The electrocatalytic active sites were shown to be comprised of these short range Ir octahedral spatially correlated sites enclosed by Co sites. Electronic structural analysis showed a downshift valence band maximum edge and d-band centers of these Ir-Co_{oct} nanodomains at the Fermi energy, as shown in Fig. 26d that could modulate the oxygen intermediate adsorption energies. An overpotential of 300 mV at 6 mA/cm^2 was exhibited with a mass activity two orders of magnitude greater than commercial IrO_2 catalysts.

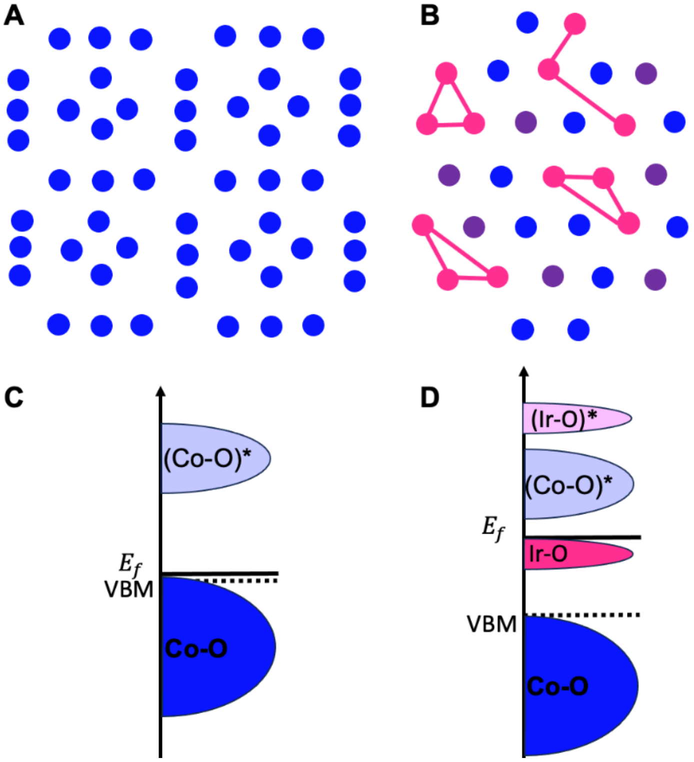

Fig. 26. The schematics of (A) represent the precursor cobalt based zeolitic imidazole framework and (B) the structural modification through Ir ion incorporation with correlated sites indicated. The corresponding Density of States diagrams are shown in (C) and (D) and reveal the formation of Ir 5d–O 2p states near the Fermi level upon Ir substitution. Figures of Shan et al. [201].

The activity was also found to be greater than Ir single atoms adsorbed onto a Co_3O_4 support without spatial correlation. Moreover, the electrocatalysis was proposed to proceed through the electrochemical oxide path mechanism, proposed by Antolini [203]. Chronopotentiometry at a current density of 10 mA/cm^2 showed 200 hrs of continuous OER electrocatalysis. Liang et al. further showed that incorporating iridium dopants into strontium titanate perovskites could activate the titanium electronic states towards surface oxygen adsorption [204]. The intrinsic activity of the catalyst, calculated by normalizing the catalytic current by the electrochemical surface area, was found to be 26 times that of commercial IrO_2 under acidic conditions. Thus the structural flexibility afforded by correlated single atom catalysts could provide an additional metal-metal interaction with the means to manipulate the electronic states of the active site to promote selective adsorbate binding. The novelty of these discovered electrocatalytic topologies enriches the potential development of potent electrocatalysts and requires an ingenuity to tailor the active sites with a coordination environment that can achieve the desired selectivity by preferentially stabilizing the intermediates and the respective transition states of the adsorbate evolution mechanism of the OER for improved stability of the catalyst, or promote the -Cl adsorbate pathway of the CER to achieve the desired selectivity at the anode to advance the potential of direct seawater electrolysis.

The characteristically high OER activity of Ru catalysts is thought to arise from its modulable redox state. The electrocatalytic activity of single atom Ru sites were shown to be electronically augmented by incorporating a compressive strain induced by the lattice mismatch of the surrounding Pt-rich coordination environment, which shifted the d-band center εRu-d towards the Fermi level, optimizing the binding the OER reaction intermediates as shown in Fig. 27 [26].

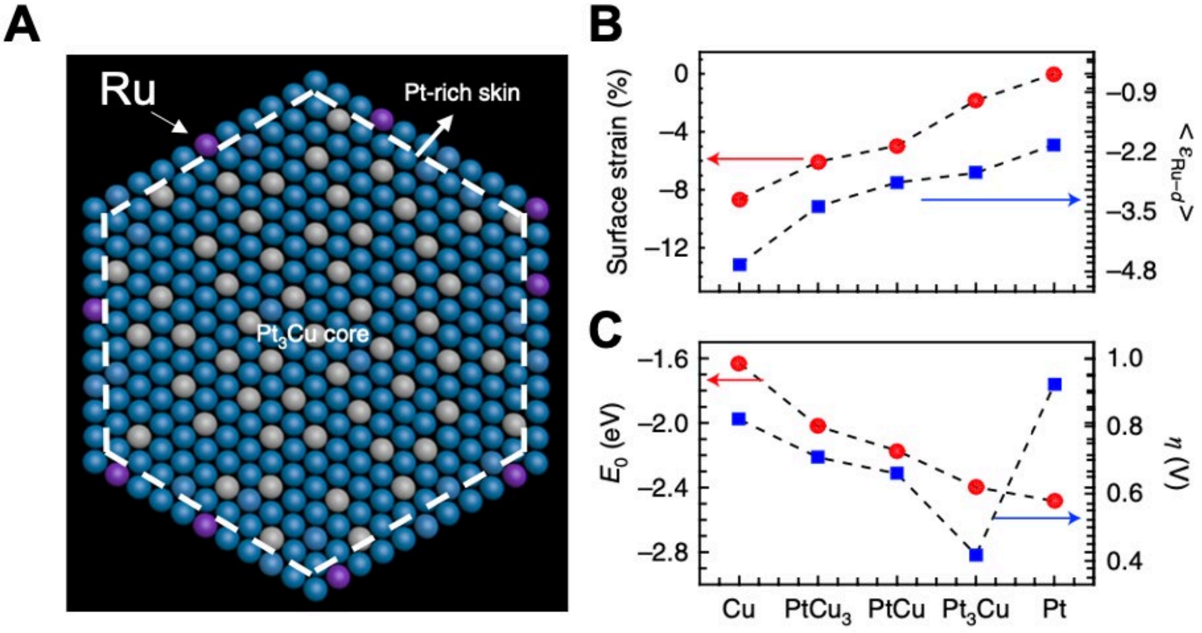

Fig. 27. (A) Representative atomic schematic of the most potent Ru_1-Pt_3Cu electrocatalyst in a series of PtCu alloys with the position of the Pt in blue, the Cu in grey, and the Ru in purple determined through elemental mapping of the HAADF image. (B) indicates the shifting of the ε_{Ru-d} towards the Fermi level in blue squares as the in-plane lattice contraction relative to a pristine Pt (111) surface in red circles decreases. (C) Indicates the corresponding absorption

energy (E_0) of the oxygen adsorbate and the overpotential (η) resolved through DFT theoretical analysis. Figures of Yao et al. [26].

ATR-IR measurements further detected the presence of the –OOH intermediate suggesting the Ru sites catalyzed the OER through the AEM mechanism, which ensured stability while also requiring an overpotential of just 220 mV to achieve the metric current density of 10 mA / cm^2 under acidic conditions [26]. In situ XAFS and XPS measurements also revealed the transfer of electrons towards the Ru atom, indicating possible charge compensation that prevented the over oxidation of the Ru atom and its subsequent dissolution [26]. Similar redox shifts were seen by Liu et al. who embedded Ru single atoms in an oxygen coordinated metal organic framework nanosheet shown in, which downshifted the bonding Ru_{3d} band center towards the bonding O_{2p} band and weakened the chemical bonding between the Ru active sites and the –Cl$^-$ adsorbate of the CER more so than the –OH adsorbate of the OER [205]. This refinement decreased the Gibbs Free Energy change of the potential determining step of the proposed CER mechanism, the second Heyrovsky step accompanying the formation of the molecular chlorine, which enabled the reaction to proceed with a lower overpotential than the OER [205]. The material demonstrated an overpotential of just 30 mV to catalyze the CER at a current density of 10 mA/cm^2 in 1 M NaCl and pH = 1, current densities of 1000 mA/cm^2 were further shown to be maintained for >1000 h with a Cl_2 selectivity of >98 % in simulated seawater [205] (Fig. 28).

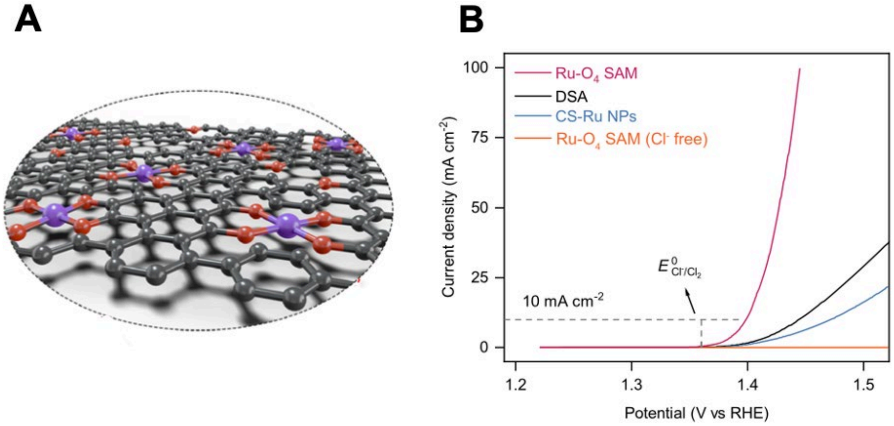

Fig. 28. (A) Schematic of the synthesized RuO_4 single atom moieties (SAM) with ruthenium in purple, oxygen in red, and carbon in grey. (B) Polarization curves of the Ru–O_4 SAM, the commercial DSA, carbon-supported Ru nanoparticles, and the Ru–O_4 SAM in a solution free of chloride ions. The scan rate was 5 mV/*sec* and the rotation rate was 1600 rpm within a 1 M NaCl solution at pH = 1. The DSA wasn't stirred, and the chloride free solution consisted of 1 M $NaClO_4$. Figure of Liu et al. [205].

Moreover, this overpotential is less than the 85 mV reported for commercial DSA, which also has a recorded Cl_2 selectivity of 95.5 %. Thus a strategy that modulates the valence of single atom Ru and the relative energies of its d-band centers through optimization of the coordination environment could enable selective binding of the CER or OER intermediates and the preferred gas evolving reaction at the anode (Table 2).

Table 2. Studied electrocatalysts probed for respective CER and OER activities. (NS) indicates not specified, (UD) is undetermined, (N/A) is not applicable, (K) is Khrishtalik, (V–H) is Volmer Heyrosky, (AEM) is Adsorbate Evolution Mechanism, (LOM) is Lattice Oxygen Mechanism.

Active Site	**Crystal Structure**	**Probed Plane**	**(+) Substitution (-) Vacancies**	**Probed Reaction**	**Preferred Mechanism**	**Ref.**
Ru (CUS)	Rutile RuO_2	100 & 110	N/A	OER	(100)	183
Ru (CUS)	Rutile RuO_2	230 & 100	N/A	CER	K (230)	184
Ru (CUS)	Rutile RuO_2	101	N/A	OER and CER	V-H (-OCl)	187
Ru (CUS)	Rutile RuO_2	101	N/A	OER and CER	V-H (-OCl)	103
Ru (CUS)	Rutile RuO_2	001	N/A	OER and CER	AEM	103
Ru (CUS)	Rutile RuO_2	110	(+) Ir or Cr	OER	AEM	188
Ru (CUS)	Rutile RuO_2	110	Top Layer TiO_2	OER and CER	V-H (-OCl)	189
Ti (CUS)	Rutile TiO_2	110	(+) Ru	CER	V-H (-OCl)	190
UD	Rutile RuO_2	NS	(+) Ti	CER	NS	193
Ru (CUS) and Mn (CUS)	Rutile RuO_2	NS	(+) Mn	OER	AEM	194
NS	Rutile RuO_2	NS	(+) Zn	OER	LOM	196
Ru (CUS)	Rutile RuO_2	NS	(+) Ni	OER	AEM	197
Ru (CUS)	Rutile RuO_2	110	(+) 2 Ni	OER	AEM	134
Ru (CUS)	Rutile RuO_2	110	(+) 6 Ni	OER	LOM	134
Ru	$Pb_2Ru_2O_{7-x}$	NS	(-) O	OER	AEM	200
Ru	$A_2Ru_2O_7$	NS	(-) A = Y, Nd, Gd, Bi	OER	AEM	204
Ir-O	$IrNi@IrO_x$	N/A	(-) Ni	OER	LOM	205
Ru	2D TiO_x	N/A	N/A	OER and CER	V-H (-Cl)	207
$Pt\text{-}N_4$	CNT	N/A	N/A	OER and CER	V-H (-OCl)	209
Ir	Co_3O_4	N/A	N/A	OER	ECOP by Antolini [213]	211
Ru	Pt_3Cu	N/A	N/A	OER	AEM	51

Ru	MOF	N/A	N/A	OER and CER	V-H (-Cl)	215

IV.3 In-Situ Filtration

The evolution of chlorine may also be impeded by arresting the species transport of the chloride ions towards the anode. Strategies such as the application of an electrochemically inert coating layer with an optimized thickness that selectivity mitigates the respective concentrations of the desired reactants and products at the buried interface, and renders a physical stability resistant to delamination; the incorporation and synthetic linkage of electrostatic repelling polyanion moieties; the degree of crystallinity of electrocatalytic surfaces; and the placement of a gas-permeable, hydrophobic membrane between the seawater and the anode have all been designed to impede the species transport of the chloride ion and selectively evolve oxygen at the anode during seawater electrolysis.

Initially implemented by Bennett, a layer of MnO_2 was electrochemical deposited onto a DSA substrate and shown to evolve oxygen from seawater with 99+% efficiency [206]. He further proposed that the coating layer prevented the diffusion of chloride ions, creating a polarized concentration gradient. Subsequent studies by Fujimura et.al. deposited MnO_2 on an IrO_2-coated titanium plate with 13 mol% molybdenum; the film was found to consist of a single phase of δ-MnO_2 that only slightly reduced the activity towards oxygen evolution while improving the durability of the material to reach an OER efficiency of 98.5 % for over 1500 h in pH = 12 at 1000 A/m^2 [74]. Further additions of tungsten were conducted by Habazaki et al., who found the manganese-molybdenum-tungsten oxide anodically deposited on an IrO_2-coated titanium improved the activity of the electrode towards the OER [207]. Moreover, additions of iron by Ghany et.al. to an Mn-Mo oxide anodically deposited on an IrO_2 coated Ti substrate was shown to improve the stability of the material at higher temperatures while maintaining 100 % OER efficiency [208].

Intrigued by the impressive OER selectivity characteristic of these manganese oxide based overlayers, Vos et al. electrochemically grew a thin film (5 – 20 nm) of MnO_x on a GC disk electrode with a IrO_x catalytic layer and used rotating ring-disk electrode voltammetry to discover that the selectivity for the CER at 30 mM Cl^- decreased from 86 % to 7 % in the presence of the MnO_x overlayer, though with a 45 % drop in activity for the OER [209]. The morphology of the overlayer consisted of a porous structure of intertwined, amorphous sheets of δ-MnO_2 with a thickness of 8–10 nm that were thought to be electrochemically inert and instead impeded the species transport of the chloride ion while remaining permeable to H_2O, H^+, and O_2 as shown in Fig. 29 [209]. Thus at the buried interface between the MnO_x and the IrO_x catalytic layer, the diffusion coefficient and concentration gradient of the chloride ion are decreased, increasing the diffusion layer thickness and the overpotential required for the chlorine evolution.

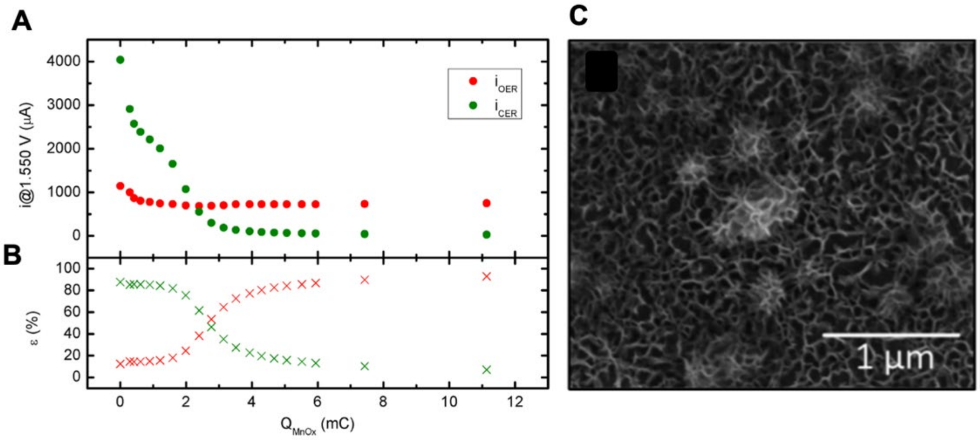

Fig. 29. (A) OER and CER recorded currents at 1.550 V calculated with the rotating ring disk electrode indicating a drop in CER currents as the charge (Q) characteristic of the MnO_x layer thickness is increased, a 45 % decrease in the OER activity is also evident. (B) The equivalent selectivities of the OER and the CER as a function of the charge of the MnO_x layer. (C) SEM image of thin, porous sheets of MnO_x deposited on the IrO_x / GC electrode. Figure of Vos et al. [209].

Beatty et al. initiated a study of the structure-property relation of the buried interface; the induced confinement effects may indeed affect the steric, chemical, and electronic properties of the mechanistic intermediates and may enable an addition means of tuning the activity and selectivity of the desired reaction [210]. Different thicknesses of SiO_2 overlayers were grown on Pt substrates of varying thicknesses. Silica is considered more thermodynamically stable in acidic and neutral solutions under a wider range of applied potentials than manganese oxide [211]. Through measurements of the hydrogen underpotential deposition (H_{upd}) by cyclic voltammetry, the peak in the voltammogram at +0.26 V RHE typically associated with Pt (100) terraces could be found for the 4.6 nm SiO_x overlayer on thick Pt substrate, though was greatly suppressed in the voltammograms of the bare Pt control and the 1.4 nm SiO_x overlayer thickness, and skewed in the 10.3 nm SiO_x overlayer due to slow proton diffusion through the overlayer, indicating that the Pt crystal orientation and densities of the crystalline defects can be modulated by the thickness of the overlayer, providing a potential means to select for the CER or OER [210]. Moreover, the thickness and composition of the Pt oxide interlayer, shown to be grown between the SiO_x overlayer and the Pt thin film through XPS measurements, was found to be tunable by adjusting the thicknesses of the SiO_x overlayer and Pt/Ti substrates; these characteristics were furthermore found to dictate electrochemical properties, the stability of the SiO_x overlayers, and the HER performance [210]. Indeed, a reduction in the thickness of the interlayer can rupture the steric environment between the interlayer and the silica overlayer, even affecting the potential mechanism. Robinson et al. moreover found that application of SiO_x overlayers on a platinum thin film disposes adjacent silanol groups at the Pt active centers that can facilitate the oxidation of the CO intermediates that have adsorbed onto Pt to CO_2, advancing the potential of fuel cells that directly utilize alcohols [212].

To thus further the applicability of silica overlayers towards selective OER catalysts, Bhardwaj et.al. applied a SiO_x overlayer on a thin Pt film electrode; the 4.8–8.7 nm overlayer thicknesses demonstrated a three order of magnitude decrease in the

Cl⁻ permittivity when compared to aromatic polyamide membranes utilized in reverse osmosis water desalination membranes as shown in Fig. 30 [21].

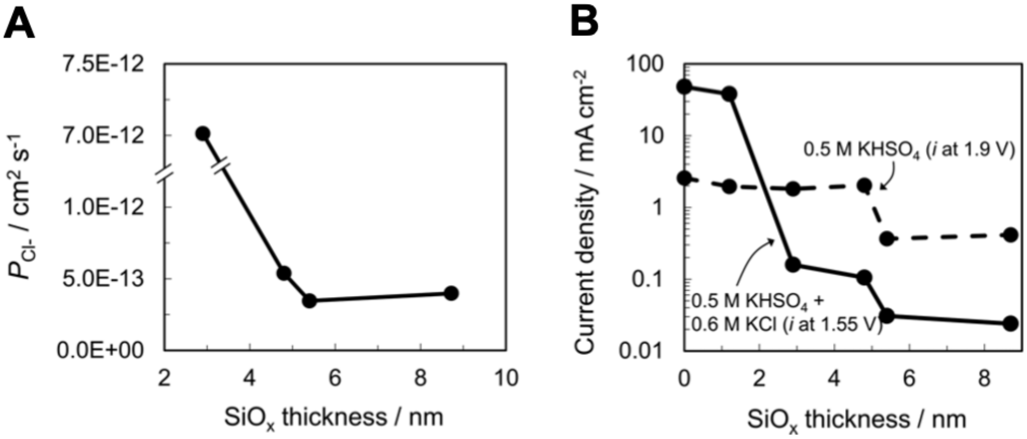

Fig. 30. (A) Calculated permeability of Cl- through an SiO$_x$ overlayer deposited on Pt thin film electrocatalyst as a function of the SiO$_x$ overlayer thickness as determined through linear scanning voltammetry in 0.5 M KHSO$_4$ + 0.6 M KCl. (B) The current densities recorded during linear scanning voltammetry at +1.90 V vs. RHE in 0.5 M KHSO$_4$ in the dotted curve and at +1.55 V vs. RHE in 0.5 M KHSO4 + 0.6 M KCl in the solid curve. Figure of Bhardwaj et al. [21].

The selective transport arresting mechanism was proposed to be the additional energy required to rearrange the bonds of the hydration sphere surrounding the chloride ion, which required removal to permeate the free volume elements within the SiO$_x$ overlayer, determined by ellipsometric porosimetry measurements and XPS analysis to have Si-Si nearest neighbor distances of ~4.6 Å [21]. Indeed, the hydrated diameters of the Cl⁻ion has been measured to be 6.5 Å [213]. Vos et al. furthered this study by also applying the SiO$_x$ overlayers on amorphous iridium oxide nanoparticles and iridium mixed-metal oxides deposited on a Ti support and found the morphology of the underlayer and its synergy with the overlayer to be of crucial importance towards achieving both a selective and stable electrocatalytic design [214]. Microscopic defects and irregularities in the IrO$_x$ nanoparticle substrate indeed affected the electrocatalytic selectivity towards the OER and no correlation between the overlayer thickness and OER selectivity could be found [214]. Silica overlayers applied on the mixed metal substrate appeared to decrease the activity for both the CER and the OER, though were more favorable towards the OER with prolonged integrity maintained during a potentiodynamic electrolysis evaluation [214].

Iridium oxide coated titanium substrates have also been hot pressed with the cation selective perfluorosulfonic acid polymer Nafion® [215]. Though achieving lower current densities, applying a Nafion-117 membrane (*H*⁺-form) onto the coated electrode allowed water to permeate while electrostatically repelling the chloride ions and led to nearly 100 % oxygen selectivity at pH = 8.3. A similar sieving mechanism with the use of the anionic backbone of sulfonated polystyrene-block-(ethylene-ran-buylene)-block- polystyrene polymer (S-PSEBS) was applied to coat an IrO$_2$/Ti anode with an electrostatically Cl⁻ repelling layer [216]. The sulfonated form of the S-PSEBS polymer, with a hydrophilicity that enables the species transport of water molecules, was shown to increase the oxygen evolution efficiency to 94 % and decrease the chlorine evolution efficiency to 6 % at 100 mA/cm² at pH = 8.3.

Selective electrocatalysts have also been designed for alkaline conditions with a graphene oxide overlayer that was electrodeposited with iron hydroxide onto an annealed, porous nickel foam that had been subjected to a hydrothermal deposition of Ni-Co hydroxide as shown in Fig. 31 [217]. The electrocatalyst was able to reach current densities of 1 A / cm^2 under alkaline conditions below overpotentials reaching 480 mV and thus before the evolution of hypochlorite becomes thermodynamically possible [217]. The graphene oxide overlayer was shown to improve the resistance to corrosion caused by the chloride ion, and moreover improve the OER activity both by decreasing the size of the FeOOH nanoparticles, and thus improving their interaction with the Ni-Co hydroxide underlayer, and by decreasing the charge transfer resistance of the material, and thus improving its electrical conductivity [217].

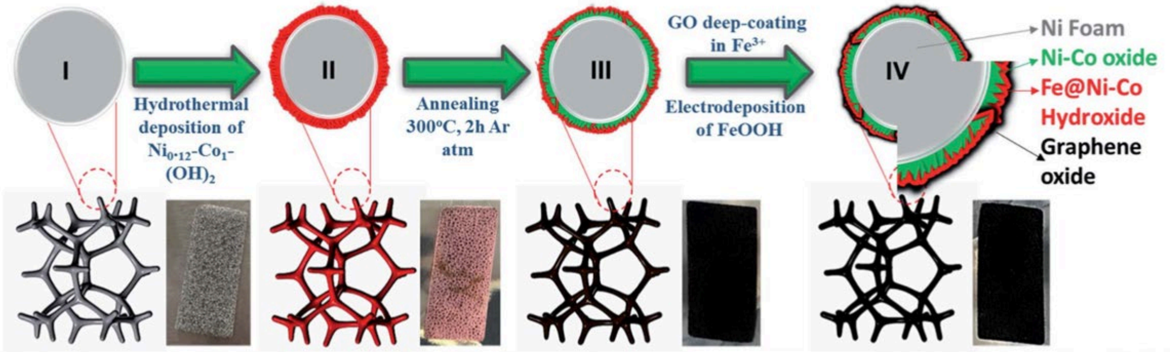

Fig. 31. Schematic depiction of the FeOOH deposited on β-Ni-Co hydroxide with a graphene oxide outer layer. Figure of Jadhav et.al. [217].

Kitiphatpiboon et al. found that by submerging a nickel foam that had been oxidized to form $NiFe(OH)_x$ along its surface into an 0.1 M Na_2S solution for sulfur integration, the stability of the electrode could be improved by the intercalation of sulfate ions, which could block the species transport of the chloride anions [218]. The sulfur doping was also shown to improve the conductivity between the active sites on $FeNiS_x$ and $NiFe(OH)_x$ [218]. A strategy that prepared porous N-$NiMo_3P$ sheets with negatively charged surface polyanions such as nitrates and phosphates also protected the electrode from the chlorine chemistry [219]. Alternatively, Obata et al. utilized anodic deposition to apply a CeO_x overlayer onto an Au substrate that had been coated with $NiFeO_x$ through conventional cathodic deposition and found that the overlayer prevented dissolution of the active Fe species and selectively impeded the chloride ion through an electrostatic interaction [220]. With an isoelectric point of 7, CeO_x is expected to be negatively charged under alkaline conditions [220]. Its hydrous, disordered structure was proposed to enable the diffusion of OH^- to the $NiFeO_x$ catalyst on the Au substrate, promoting an OER overpotential shown to be less than the onset of the hypochlorite redox potential [220,221].

Interestingly, a hollow nanocubic electrocatalyst composed of Ir-doped Ni-Fe-Zn Prussian blue analogs was demonstrated to manifest abundant amorphous-crystalline interfaces (ACI) that were indicated to be in-situ passivated with carbonate anions after prolonged electrolysis in an alkaline seawater electrolyte [222]. These carbonate anions were proposed to protect the electrocatalyst against chloride corrosion by repelling the negatively charged chloride anions. The synthesized hollow nanocubes were further shown to have a higher catalytic activity than commercial IrO_2 in alkaline, alkaline seawater, and acidic electrolytes that was proposed to be facilitated by the heterogeneity of atomic arrangements at the ACI surface as shown in Fig. 32 [222]. The Zn was however shown to be completely leached out under acidic conditions, though a synergy between the Ni, Fe, and Ir at the surface of the nanocubes was supposed to preserve the ACI during water oxidation.

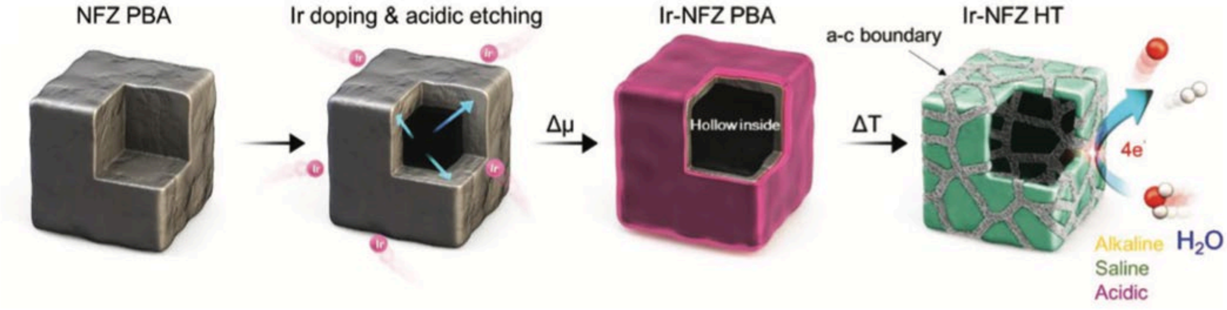

Fig. 32. Schematic representation of the synthetic route utilized to generate the numerous amorphous-crystalline interfaces on the Ir-NFZ HT nanocube. Figure of Han et al. [222].

Xie et al. further designed a hydrophobic, porous polytetrafluoroethylene (PTFE) based membrane permeable only to gases that encompassed the anode and sandwiched a concentrated KOH solution, termed a self-dampening electrolyte, that provided a water vapor pressure gradient driving the evaporation and diffusion of water vapor from the seawater across the PTFE membrane towards the catalyst at the anode as shown in Fig. 33 [223]. Current densities of 250 mA/cm^2 with an operational lifetime of over 3200 h were achieved [223].

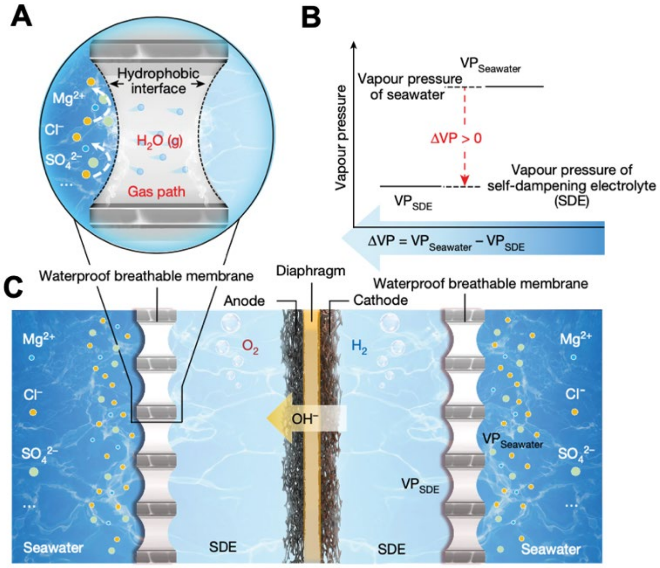

Fig. 33. (A) Schematic of the hydrophobic porous polytetrafluoroethylene (PTFE)-based waterproof breathable membrane permitting the selective diffusion of water vapor while remaining impermeable to impurity ions and seawater. (B) Representation of the driving force created for water vapor diffusion through application of a self-

dampening electrolyte. (C) Depiction of the orientation of the membrane and the electrolyte with respect to the anode and the cathode. Figure of Xie et al. [223].

The use of the membrane within the electrolyzer unit itself could moreover act as a filtering mechanism to prevent the movement of the chloride ion towards the anode. Though an asymmetric electrolyzer design, Shi et al. introduced natural seawater into the cathode compartment and a hydroxide solution into the anode compartment; the species transport of the chloride ion was impeded from approaching the anode through the placement of a sodium ion exchange membrane [224]. The Ni-Fe-P nanowires anchored with atomically dispersed Pt at the cathode accelerated hydrogen evolution through a DFT calculated energy barrier reduction of 0.26 eV in natural seawater [224].

IV.4 Augmenting the Conductivity

By manipulating the surface structure of the catalyst, an augmentation in the conductivity may be realized, which may indeed lower the overpotential required to effectuate the OER and enable selectivity against the CER to be achieved under acidic conditions. Conductivity is related to the concentration of mobile electronic carriers such as electrons, holes, and ionic point defects occupying lattice atomic positions such as vacancies, interstitials, and substitutional solutes as well as impurities [225]. Indeed, removing oxygen atoms through mechanisms such as the Mars-van Krevelen leaves excess electrons either delocalized through a metallic state or localized within a polaronic state [226]. The mobility of these electronic carriers is defined as the velocity of the entity per unit driving force and is directly proportional to the diffusion coefficient according to the Nernst-Einstein relation. In addition, electrons and holes in metals, semiconductors, and high-mobility ceramics are subject to a drift velocity that is much less than the instantaneous velocity of random particle movements. Their mobility is inversely proportional to their effective mass, which considers the interaction between the charge carrier and the lattice potential [225]. This polaronic interaction may be large, which indicates a weak interaction between the carrier and the ion and a small effective mass, or strong resulting in large polarons in which the motion of electrons and holes must occur through a thermally activated hopping mechanism and can reduce mobility [225]. Kim et al. synthesized an IrO_2 shell encasing a metallic iridium core by rapidly dealloying osmium from an $Ir_{25}Os_{75}$ alloy under highly acidic conditions [121]. A decrease in overpotential for the $Ir_{25}Os_{75}$ core-shell thin film when compared to a synthesized $Ir_{50}Os_{50}$ nanoparticle at high current densities is shown in Fig. 34a, which was attributed to the measured increase in conductivity [121]. The conductivities of the 3D-interconnected, porous $Ir_{25}Os_{75}$ core-shell thin film and the $Ir_{50}Os_{50}$ nanoparticles, proposed to be highly oxidized and consisting of many insulating oxide interfaces, were quantified through measurements of the carrier mobility and carrier density with 4-probe van der Pauw measurements [121]. The interconnected heterogeneity of a metallic core oxide shell structure could indeed create additional undercoordinated sites that induce alterations in the local geometries, the electronic structures, and additional defect sites that can be manipulated to tailor the electrocatalytic properties of the surface [226].

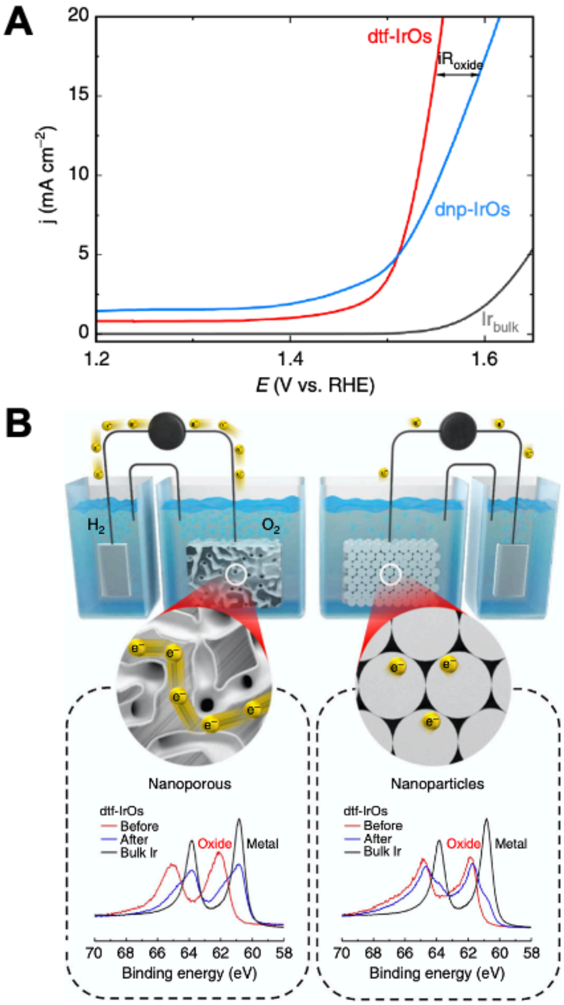

Fig. 34. (A) Linear sweep voltammogram with a rotating disk electrode in 0.1 M $HClO_4$ showing the polarization curves of the $Ir_{25}Os_{75}$ core-shell material (dtf-IrOs) and $Ir_{50}Os_{50}$ nanoparticle (dnp-IrOs). (B) A depiction of the effect of numerous, insulating oxide interfaces on the conductivity of the material; the oxides layers were quantified through XPS sputter etching experiments. The XPS experiments for the dtf-IrOs material indicated on the other hand the presence of an Ir-metallic core. Figure of Kim et al. [121].

Indeed, induction of polaronic interactions with the CO adsorbate in the rutile titanium dioxide (110) was shown to significantly affect its adsorption energy and the polaronic ground state of the system; CO adsorption was shown to promote polaron transfer from subsurface to surface sites [227]. Probed through analysis of the polaron formation energy, or the electronic energy gained by phonon-electron coupling balanced the energy lost to local lattice distortions, the CO adsorbate was shown to not only reduce the energy cost to form the polaron though also was found to bind most favorably at a titanium atom site with a polaron just below [227].

Stoerzinger et al. manipulated the degree of epitaxial strain within a $LaCoO_3$ thin film grown through pulsed layer deposition on insulating substrates of different thicknesses and found the degree of tensile strain to influence the electrical conductivity and observed activity towards the OER; deviations in the local symmetry were proposed to affect the number of defects sites and the charge transfer resistance, and moreover to decrease the Co–O bond distance and increase the strength of the adsorbed bond to oxygen [228]. Engineering these defects were moreover shown to dramatically improve the OER performance of a Co-doped nanorod-like RuO_2 electrocatalyst; the low oxidation state of the Co dopant required less O^{2-} in the RuO_2 lattice and thus yielded oxygen vacancies, as evidenced through X-ray photoelectron spectroscopy analysis [229]. The oxygen vacancies were proposed to improve not only the electrical conductivity of the materials though also augment the number of active sites, and moreover participate in the LOM mechanism, calculated to be the lowest free energy path according to DFT simulations [229]. Overpotentials of 169 mV for the OER under acidic conditions were achieved with stable chronopotentiometry measurements for over 50 h at 10 mA/cm^2 [229]. Thus strategies that implement designs to elevate the conductivity of the electrocatalyst at the active site through formation of point defects and manipulation of the electronic structure have the potential to tune the binding of the preferential intermediate and moreover promote the activity of the material without depreciating the inherent stability.

IV.5 Self-Healing Catalysts

Tuning the catalytic active site and the reaction mechanism selectivity is indicated within to be quite challenging through heterogeneous electrocatalysis of PGM metals. Though the high anodic potentials required to effectuate the OER and the resulting harshly acidic environment has generally required a characteristically robust catalyst such as a heterogeneous catalyst composed of PGM metals in PEMWE technology [230]. Indeed, oxides of earth-abundant metals are basic according to the Lux classification of bases, and thus readily react with acid and corrode through leaching and dissolution [231]. Implementation of molecular electrocatalysts to facilitate the OER can on the other hand enable the structure-activity relationships and reaction mechanisms to be finely tuned through manipulation of the ligand design [230]. However, most of the ligand design optimizations to impart selective activity of the metal center such as metathesis, transfer dehydrogenation, C–H activation and functionalization, and cross coupling bond formation have been developed under reductive conditions, requiring the development of ligands stable to oxidative transformations [232].

One approach to catalyst design can be the development of molecular electrocatalysts which undergo self-healing, the characteristic ability to reform from a self-assembly process [233]. If the equilibrium for self-assembly energetically lies within that of the OER catalysis, overall corrosion of the catalyst can be avoided [233]. Indeed, regeneration will occur if the catalyst can self-assemble at applied potentials lower than the potentials required to effectuate the OER. If a greater dependence on the proton concentration through calculation of its reaction order within the mechanism is moreover found for the self-healing catalyst than for the catalysis of the OER, pH adjustments can be utilized to selectively tune the propensity towards self-assembly while maintaining catalytic functionality [233]. Huynh et al. electrodeposited manganese oxide (MnO_x) onto an FTO working electrode and determined its catalytic rate law for the OER through assessments of the Tafel slopes and the reaction order with respect to the proton concentration at acidic and basic pH values [234]. Reformulations of the Tafel plots to a single potential (E) vs. pH plot, shown in Fig. 35, with an additional MnO_x deposition trace under acidic [235] and slightly basic conditions [236] enabled a prediction of the pH conditions in which catalyst regeneration subsides and a net dissolution of the film commences [234]. The self-healing property of the MnO_x catalytic film, shown to evolve through the disproportionation reaction of two Mn^{+3} ions, was indeed indicated to uphold until a pH of 0 was approached.

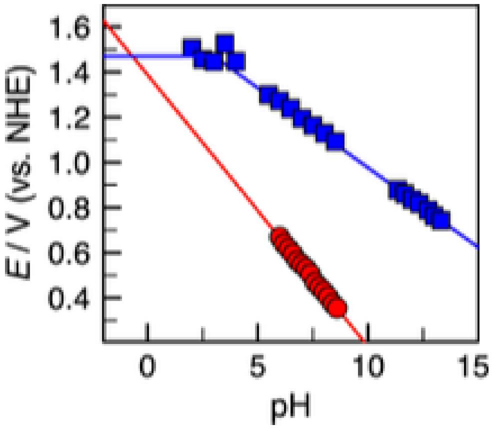

Fig. 35. The potential required for the evolution of oxygen on MnO_x (blue squares) as a function of the pH showing a zero-order dependence on the proton concentration under acidic conditions and the inverse first-order dependence in the alkaline regime. The red trace indicates the fourth-order dependence of MnO_x deposition on the proton concentration under acidic and near neutral pH regimes that were divulged from the literature. The concentrations of Mn^{+2} under both measurements are comparable. Figure of Huynh et al. [234].

Surendranath et al. further showed that cobalt phosphate (CoP_i) was capable of self-healing; electrodeposition of the oxidic metallate onto a FTO electrode achieved an O_2 faradaic efficiency of near 100 % in neutral salt water [237]. The high activity of this catalyst towards the OER in neutral pH conditions was further proposed to improve the selectivity against the CER, which according to the Pourbaix analysis discussed above, becomes thermodynamically unfavored as the pH increases and the OER becomes more thermodynamically preferred [238]. Though more importantly, selectivity against the CER was shown to be achieved by engaging the kinetic competition between the water and chloride ion through exposure of the catalytic edge sites of the metallate cluster present in the CoP_i complexes [238]. The large disparity between the concentration of water and that of chloride ions in solution can promote the substitution of P_i for water to initiate the O–O bond formation. The effectiveness of this strategy to achieve selectivity is seen in Fig. 36, where differential electrochemical mass spectrometry (DEMS) was used to determine the quantities of oxygen and chlorine evolved at pH = 7.

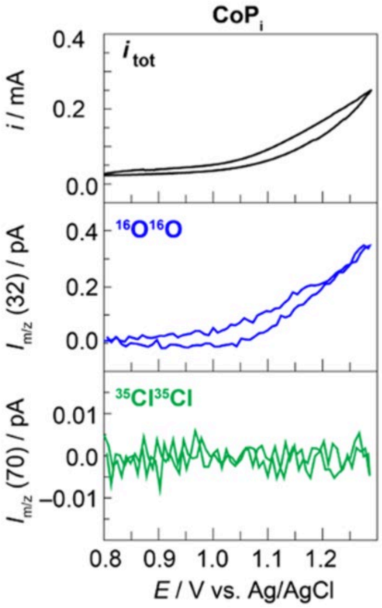

Fig. 36. The top panel is a cyclic voltammogram of CoP$_i$ in an aqueous solution of 100 mM KP$_i$ and 500 mM NaCl at a scan rate of 5 mV/s. The middle and bottom panels are the DEMS results for the evolved oxygen and the evolved chlorine, respectively. Figure of Kean and Nocera [238].

The presence of phosphate in the solution was moreover shown to decrease the faradaic efficiency for the CER through both its buffering effect and ability to associate with oxide surfaces through an inner-sphere mechanism and form a negatively-charged electrically repelling layer [239]. Applying the ingenuity of this advancement towards the design of heterogeneous electrocatalysts selective for the OER that are imbued with the propensity for self-healing under acidic conditions would engender a robust solution for PEMWE technology.

V. Conclusions

A social-technological crisis has emerged as the energy demands of our increscent societies encroach on limited freshwater reserves. It is urgent to develop the capability of utilizing the abundant reserves of seawater in sustainably driven water electrolysers for the generation of hydrogen. While indirect electrolysis may provide the needed short-term solution, the inevitable additional energy costs will prove absorbent over the long term. The advancement of direct seawater technologies that further the selectivity of the anode may improve wastewater treatments, appeasing the exigencies for water conservation imperative for an increasing percentage of our inhabited world. Though utilizing seawater directly in the current state-of-the-art electrolyser technologies can affect its performance both at the system and stack level by degrading the electrolyser durability. Specifically, the presence of the chloride ion enables the evolution of the toxic and corrosive chlorine gas. Using seawater as an electrolyte can also affect the electrochemically active dimensions of the catalyst and perturb the electrolyte permeabilities, diffusivities, conductivities, and vapor pressure, impacting the current and voltage efficiencies.

Thermodynamic analysis of the Pourbaix diagram for artificial seawater indicates that the competition between the oxygen evolution and chlorine evolution is exacerbated in the acidic medium of PEM electrolysers. Nonetheless, in this condition the highest current densities have been achieved. Butler-Volmer kinetics and Marcus theory clarifies the relation between the thermodynamics and the kinetics of electrochemical reactions, enabling an understanding of the observed chlorine gas evolution at the anode. Despite the greater standard potential of the CER, the reaction proceeds through a single intermediate that enables chlorine evolution to be the kinetic product during seawater electrolysis. The proposed mechanisms of the OER were elucidated and indicated that the LOM mechanism can affect the stability of the anode. Thus, designing strategies that can promote the AEM mechanism were proposed. However, the elucidated mechanisms of the CER indicated that the relationship between the key intermediates of the CER pathway and the AEM pathway of the OER are linearly correlated. The need to dissect the rate determining step of the preferred pathway is crucial to stabilize transition states to select for the preferred intermediate. This feat could be accomplished perhaps through the development of descriptors that moreover incorporate stability parameters to derive a catalyst at the apex of the volcano curve possessing realistic potency. Indeed, predictions of the best catalysts must thus be developed with a robustness that accounts for the multi-faceted complexity involved in heterogeneous electrocatalysis to devise the most effective system. Overcoming the inherent linear correlations that the proposed AEM pathway of the OER are subjected to is another potential though challenging means of achieving selectivity. The water and chloride reagents were moreover shown to competitively adsorb onto the electrocatalyst surface; the concentration discrepancy between the water and chloride reagents in solution can thus influence the observed evolved gaseous product.

Achieving selectivity at the anode is therefore a formidable challenge. Design strategies that modulate the structure of the electrocatalyst such as optimizing the exposure of the facet with the greatest OER selectivity, introducing point defects in the local chemical environment, and improving the active site density are ongoing. Indeed, further implementing the design of correlated single atom catalysts could afford the structural flexibility to manipulate the type of atom and its proportion within the first and second coordination shell and optimize the electronic state of the active site to promote selective adsorbate binding. Ruthenium and its modulable redox state greatly diversifies the potential coordination environments and the relative energies of its d-band centers, enabling the optimization of the adsorbate binding. The design of catalysts with greater conductivities may further decrease the observed OER overpotentials. The most realizable solution may indeed be the incorporation of an overlayer that arrests the transport of the chloride ion and decreases its concentration at the active site. Moreover, development of heterogeneous electrocatalytic systems with a penchant for self-healing would facilitate the needed stability under the harsh acidic conditions within PEMWE. Further insights into the effects of the electrified double layer, and the structural sensitivity of adsorbate binding on the electrocatalysis of the evolved gaseous products may further the efforts to achieve selectivity for the OER at the anode under the perilous acidic conditions. Indeed, these design strategies may provide insights into future research efforts to uncover an optimal electrocatalytic surface for selective OER evolution and reveal an effective solution as serendipitous as the abundancy of a natural resource that calls to be implemented into our burgeoning societies for the advancement of our future generations.

Acknowledgements

This research was supported by 3rd Programme d'Investissements d'Avenir [ANR-18-EUR-0006-02]

VI. References

[1] IEA, Comparison of total final consumption in the IPCC scenarios and in the Net Zero Scenario, 2020-2050, in: IEA (Ed.), International Energy Agency, Paris, 2021.

[2] IEA, Net Zero by 2050: A Roadmap for the Global Energy Sector, International Energy Agency, Paris, 2021.

[3] G.L. Decker, Gouse, W.S., Gregory, D.P., Hirsch, R.L., Hoffman, K.C., Hoos, I.R., Johnson, J.E., Longwell,J.P., Siri, W.E., Sliepcevich, C.M., Smelt, R., Hydrogen as a Fuel: A Report, National Academies Press1979.

[4] D. Crisp, H. Dolman, T. Tanhua, G.A. McKinley, J. Hauck, A. Bastos, S. Sitch, S. Eggleston, V. Aich, How Well Do We Understand the Land-Ocean-Atmosphere Carbon Cycle?, Rev. Geophys., 60 (2022) e2021RG000736.

[5] R. de Levie, The electrolysis of water, J. Electroanal. Chem., 476 (1999) 92-93.

[6] R.F. Service, Seawater splitting could help green hydrogen grow, Science, 379 (2023) 1075.

[7] F.a.A. Organization, Renewable internal freshwater resources, in: A. data (Ed.), 2020.

[8] J.J. Urban, Emerging Scientific and Engineering Opportunities within the Water-Energy Nexus, Joule, 1 (2017) 665-688.

[9] U. Nations, United Nations World Water Development Report 2021: Valuing Water, UNESCO 2021, 7, place de Fontenoy, 75352 Paris 07 SP, France, 2021.

[10] F.J. Millero, R. Feistel, D.G. Wright, T.J. McDougall, The composition of Standard Seawater and the definition of the Reference-Composition Salinity Scale, Deep Sea Res. Part I Oceanogr. Res., 55 (2008) 50-72.

[11] H. Yu, J. Wan, M. Goodsite, H. Jin, Advancing direct seawater electrocatalysis for green and affordable hydrogen, One Earth, 6 (2023) 267-277.

[12] Q. Li, A. Molina Villarino, C.R. Peltier, A.J. Macbeth, Y. Yang, M.-J. Kim, Z. Shi, M.R. Krumov, C. Lei, G.G. Rodríguez-Calero, J. Soto, S.-H. Yu, P.F. Mutolo, L. Xiao, L. Zhuang, D.A. Muller, G.W. Coates, P. Zelenay, H.D. Abruña, Anion Exchange Membrane Water Electrolysis: The Future of Green Hydrogen, J. Phys. Chem. C, 127 (2023) 7901-7912.

[13] J.N. Hausmann, R. Schlögl, P.W. Menezes, M. Driess, Is direct seawater splitting economically meaningful?, Energy Environ. Sci., 14 (2021) 3679-3685.

[14] D. Li, A.R. Motz, C. Bae, C. Fujimoto, G. Yang, F.-Y. Zhang, K.E. Ayers, Y.S. Kim, Durability of anion exchange membrane water electrolyzers, Energy Environ. Sci., 14 (2021) 3393-3419.

[15] D. Li, E.J. Park, W. Zhu, Q. Shi, Y. Zhou, H. Tian, Y. Lin, A. Serov, B. Zulevi, E.D. Baca, C. Fujimoto, H.T. Chung, Y.S. Kim, Highly quaternized polystyrene ionomers for high performance anion exchange membrane water electrolysers, Nat. Energy, 5 (2020) 378-385.

[16] S. Dresp, T. Ngo Thanh, M. Klingenhof, S. Brückner, P. Hauke, P. Strasser, Efficient direct seawater electrolysers using selective alkaline NiFe-LDH as OER catalyst in asymmetric electrolyte feeds, Energy Environ. Sci., 13 (2020) 1725-1729.

[17] M.L. Frisch, T.N. Thanh, A. Arinchtein, L. Hager, J. Schmidt, S. Brückner, J. Kerres, P. Strasser, Seawater Electrolysis Using All-PGM-Free Catalysts and Cell Components in an Asymmetric Feed, ACS Energy Lett., 8 (2023) 2387-2394.

[18] E.B. Carneiro-Neto, M.C. Lopes, E.C. Pereira, Simulation of interfacial pH changes during hydrogen evolution reaction, J. Electroanal. Chem., 765 (2016) 92-99.

[19] I. Katsounaros, J.C. Meier, S.O. Klemm, A.A. Topalov, P.U. Biedermann, M. Auinger, K.J.J. Mayrhofer, The effective surface pH during reactions at the solid–liquid interface, Electrochem. Commun., 13 (2011) 634-637.

[20] W. Tong, M. Forster, F. Dionigi, S. Dresp, R. Sadeghi Erami, P. Strasser, A.J. Cowan, P. Farràs, Electrolysis of low-grade and saline surface water, Nat. Energy, 5 (2020) 367-377.

[21] A.A. Bhardwaj, J.G. Vos, M.E.S. Beatty, A.F. Baxter, M.T.M. Koper, N.Y. Yip, D.V. Esposito, Ultrathin Silicon Oxide Overlayers Enable Selective Oxygen Evolution from Acidic and Unbuffered pH-Neutral Seawater, ACS Catal., 11 (2021) 1316-1330.

[22] R. Rossi, D.M. Hall, L. Shi, N.R. Cross, C.A. Gorski, M.A. Hickner, B.E. Logan, Using a vapor-fed anode and saline catholyte to manage ion transport in a proton exchange membrane electrolyzer, Energy Environ. Sci., 14 (2021) 6041-6049.

[23] S. Kumari, R. Turner White, B. Kumar, J.M. Spurgeon, Solar hydrogen production from seawater vapor electrolysis, Energy Environ. Sci., 9 (2016) 1725-1733.

[24] R.J. Ouimet, J.R. Glenn, D. De Porcellinis, A.R. Motz, M. Carmo, K.E. Ayers, The Role of Electrocatalysts in the Development of Gigawatt-Scale PEM Electrolyzers, ACS Catal., 12 (2022) 6159-6171.

[25] C. Minke, M. Suermann, B. Bensmann, R. Hanke-Rauschenbach, Is iridium demand a potential bottleneck in the realization of large-scale PEM water electrolysis?, Int. J. Hydrog. Energy., 46 (2021) 23581-23590.

[26] Y. Yao, S. Hu, W. Chen, Z.-Q. Huang, W. Wei, T. Yao, R. Liu, K. Zang, X. Wang, G. Wu, W. Yuan, T. Yuan, B. Zhu, W. Liu, Z. Li, D. He, Z. Xue, Y. Wang, X. Zheng, J. Dong, C.-R. Chang, Y. Chen, X. Hong, J. Luo, S. Wei, W.-X. Li, P. Strasser, Y. Wu, Y. Li, Engineering the electronic structure of single atom Ru sites via compressive strain boosts acidic water oxidation electrocatalysis, Nat. Catal., 2 (2019) 304-313.

[27] M. Sohail, W. Lv, Z. Mei, Recent Progress in Ruthenium-Based Electrocatalysts for Water Oxidation under Acidic Condition, ACS Sustain. Chem. Eng., 11 (2023) 17564-17594.

[28] S.M. Alia, S. Stariha, R.L. Borup, Electrolyzer Durability at Low Catalyst Loading and with Dynamic Operation, J. Electrochem. Soc., 166 (2019) F1164.

[29] M. Faustini, M. Giraud, D. Jones, J. Rozière, M. Dupont, T.R. Porter, S. Nowak, M. Bahri, O. Ersen, C. Sanchez, C. Boissière, C. Tard, J. Peron, Hierarchically Structured Ultraporous Iridium-Based Materials: A Novel Catalyst Architecture for Proton Exchange Membrane Water Electrolyzers, Adv. Energy Mater., 9 (2019) 1802136.

[30] M. Carmo, G.P. Keeley, D. Holtz, T. Grube, M. Robinius, M. Müller, D. Stolten, PEM water electrolysis: Innovative approaches towards catalyst separation, recovery and recycling, Int. J. Hydrog. Energy., 44 (2019) 3450-3455.

[31] L.E.C. Shore, Process for recycling components of a PEM fuel cell membrane electrode assembly, in: US (Ed.), 2012.

[32] Z. Wang, Y.-R. Zheng, I. Chorkendorff, J.K. Nørskov, Acid-Stable Oxides for Oxygen Electrocatalysis, ACS Energy Lett., 5 (2020) 2905-2908.

[33] H.O. Ailong Li, Nadège Bonnet, Toru Hayashi, Yimeng Sun, Qike Jiang, Can Li, Hongxian Han, Ryuhei Nakamura, Stable Potential Windows for Long-Term Electrocatalysis by Manganese Oxides Under Acidci Conditions, Angew. Chem. Int. Ed., 58 (2019) 5054-5058.

[34] I.A. Moreno-Hernandez, C.A. MacFarland, C.G. Read, K.M. Papadantonakis, B.S. Brunschwig, N.S. Lewis, Crystalline nickel manganese antimonate as a stable water-oxidation catalyst in aqueous 1.0 M H2SO4, Energy Environ. Sci., 10 (2017) 2103-2108.

[35] A.E. Thorarinsdottir, C. Costentin, S.S. Veroneau, D.G. Nocera, p-Block Metal Oxide Noninnocence in the Oxygen Evolution Reaction in Acid: The Case of Bismuth Oxide, Chem. Mater., 34 (2022) 826-835.

[36] M. Blasco-Ahicart, J. Soriano-López, J.J. Carbó, J.M. Poblet, J.R. Galan-Mascaros, Polyoxometalate electrocatalysts based on earth-abundant metals for efficient water oxidation in acidic media, Nat. Chem., 10 (2018) 24-30.

[37] S.S. Veroneau, A.C. Hartnett, A.E. Thorarinsdottir, D.G. Nocera, Direct Seawater Splitting by Forward Osmosis Coupled to Water Electrolysis, ACS Appl. Energy Mater., 5 (2022) 1403-1408.

[38] S.S. Veroneau, D.G. Nocera, Continuous electrochemical water splitting from natural water sources via forward osmosis, Proc. Natl. Acad. Sci., 118 (2021) e2024855118.

[39] Z. Yang, P.-F. Sun, X. Li, B. Gan, L. Wang, X. Song, H.-D. Park, C.Y. Tang, A Critical Review on Thin-Film Nanocomposite Membranes with Interlayered Structure: Mechanisms, Recent Developments, and Environmental Applications, Environ. Sci. Technol., 54 (2020) 15563-15583.

[40] H.B. Park, J. Kamcev, L.M. Robeson, M. Elimelech, B.D. Freeman, Maximizing the right stuff: The trade-off between membrane permeability and selectivity, Science, 356 (2017) eaab0530.

[41] G.M. Geise, H.B. Park, A.C. Sagle, B.D. Freeman, J.E. McGrath, Water permeability and water/salt selectivity tradeoff in polymers for desalination, J. Membr. Sci., 369 (2011) 130-138.

[42] U. Caldera, C. Breyer, Learning Curve for Seawater Reverse Osmosis Desalination Plants: Capital Cost Trend of the Past, Present, and Future, Water Resour. Res., 53 (2017) 10523-10538.

[43] H. Becker, J. Murawski, D.V. Shinde, I.E.L. Stephens, G. Hinds, G. Smith, Impact of impurities on water electrolysis: a review, Sustain. Energy Fuels, 7 (2023) 1565-1603.

[44] C.D.R. Azevedo, A. Baeza, E. Chauveau, J.A. Corbacho, J. Díaz, J. Domange, C. Marquet, M. Martínez-Roig, F. Piquemal, C. Roldán, J. Vasco, J.F.C.A. Veloso, N. Yahlali, Design, setup and routine operation of a water treatment system for the monitoring of low activities of tritium in water, Nucl. Eng. Technol., 55 (2023) 2349-2355.

[45] A.P. G. Tsotridis, EU harmonized protocols for testing of low temperature water electrolysis, in: E. Union (Ed.), 2021.

[46] ISO3696, Water for Analytical Laboratory Use - Specification and Test Methods, 1987.

[47] E.J. Okampo, N. Nwulu, Optimisation of renewable energy powered reverse osmosis desalination systems: A state-of-the-art review, Renew. Sust. Energ. Rev., 140 (2021) 110712.

[48] P. Farràs, P. Strasser, A.J. Cowan, Water electrolysis: Direct from the sea or not to be?, Joule, 5 (2021) 1921-1923.

[49] M.F. Lagadec, A. Grimaud, Water electrolysers with closed and open electrochemical systems, Nat. Mater., 19 (2020) 1140-1150.

[50] W. Zheng, L.Y.S. Lee, K.-Y. Wong, Improving the performance stability of direct seawater electrolysis: from catalyst design to electrode engineering, Nanoscale, 13 (2021) 15177-15187.

[51] P.M. Natishan, W.E. O'Grady, Chloride Ion Interactions with Oxide-Covered Aluminum Leading to Pitting Corrosion: A Review, J. Electrochem. Soc., 161 (2014) C421.

[52] T.u. Haq, Y. Haik, Strategies of Anode Design for Seawater Electrolysis: Recent Development and Future Perspective, Small Science, 2 (2022) 2200030.

[53] A.R. Zeradjanin, The era of stable electrocatalysis, Nat. Catal., 6 (2023) 458-459.

[54] M.B. Ives, Y.C. Lu, J.L. Luo, Cathodic reactions involved in metallic corrosion in chlorinated saline environments, Corros. Sci., 32 (1991) 91-102.

[55] J.G. Vos, A. Venugopal, W.A. Smith, M.T.M. Koper, Competition and selectivity during parallel evolution of bromine, chlorine and oxygen on IrOx electrodes, J. Catal., 389 (2020) 99-110.

[56] S. Geiger, S. Cherevko, K.J.J. Mayrhofer, Dissolution of Platinum in Presence of Chloride Traces, Electrochim. Acta, 179 (2015) 24-31.

[57] M. Maril, J.-L. Delplancke, N. Cisternas, P. Tobosque, Y. Maril, C. Carrasco, Critical aspects in the development of anodes for use in seawater electrolysis, Int. J. Hydrog. Energy., 47 (2022) 3532-3549.

[58] D.W. Kirk, A.E. Ledas, Precipitate formation during sea water electrolysis, Int. J. Hydrog. Energy., 7 (1982) 925-932.

[59] S. Dresp, F. Dionigi, M. Klingenhof, P. Strasser, Direct Electrolytic Splitting of Seawater: Opportunities and Challenges, ACS Energy Lett., 4 (2019) 933-942.

[60] J.-H. Han, E. Jwa, H. Lee, E.J. Kim, J.-Y. Nam, K.S. Hwang, N. Jeong, J. Choi, H. Kim, Y.-C. Jeung, T.D. Chung, Direct seawater electrolysis via synergistic acidification by inorganic precipitation and proton flux from bipolar membrane, J. Chem. Eng., 429 (2022) 132383.

[61] V. Kumaravel, A. Abdel-Wahab, A Short Review on Hydrogen, Biofuel, and Electricity Production Using Seawater as a Medium, Energy Fuels, 32 (2018) 6423-6437.

[62] A. Belila, J. El-Chakhtoura, N. Otaibi, G. Muyzer, G. Gonzalez-Gil, P.E. Saikaly, M.C.M. van Loosdrecht, J.S. Vrouwenvelder, Bacterial community structure and variation in a full-scale seawater desalination plant for drinking water production, Water Research, 94 (2016) 62-72.

[63] C. Debiemme-Chouvy, H. Cachet, Electrochemical (pre)treatments to prevent biofouling, Curr. Opin. Electrochem., 11 (2018) 48-54.

[64] D.E. Slauenwhite, B.D. Johnson, Bubble shattering: Differences in bubble formation in fresh water and seawater, Journal of Geophysical Research: Oceans, 104 (1999) 3265-3275.

[65] Z. Zhang, W. Liu, M.L. Free, Phase-Field Modeling and Simulation of Gas Bubble Coalescence and Detachment in a Gas-Liquid Two-Phase Electrochemical System, J. Electrochem. Soc., 167 (2020) 013532.

[66] J. Tourneur, L. Joanny, L. Perrin, S. Paul, B. Fabre, Efficient and Highly Stable 3D-Printed NiFe and NiCo Bifunctional Electrodes for Practical HER and OER, ACS Applied Engineering Materials, 1 (2023) 2676-2684.

[67] M. Schalenbach, G. Tjarks, M. Carmo, W. Lueke, M. Mueller, D. Stolten, Acidic or Alkaline? Towards a New Perspective on the Efficiency of Water Electrolysis, J. Electrochem. Soc., 163 (2016) F3197.

[68] L.I. Gordon, Y. Cohen, D.R. Standley, The solubility of molecular hydrogen in seawater, Deep Sea Res., 24 (1977) 937-941.

[69] K.G. Nayar, M.H. Sharqawy, L.D. Banchik, J.H. Lienhard V, Thermophysical properties of seawater: A review and new correlations that include pressure dependence, Desalination, 390 (2016) 1-24.

[70] R.L. LeRoy, C.T. Bowen, D.J. LeRoy, The Thermodynamics of Aqueous Water Electrolysis, J. Electrochem. Soc., 127 (1980) 1954-1962.

[71] R.M. de Jonge, E. Barendrecht, L.J.J. Janssen, S.J.D. van Stralen, Gas bubble behaviour and electrolyte resistance during water electrolysis, Int. J. Hydrog. Energy., 7 (1982) 883-894.

[72] F. Dionigi, T. Reier, Z. Pawolek, M. Gliech, P. Strasser, Design Criteria, Operating Conditions, and Nickel–Iron Hydroxide Catalyst Materials for Selective Seawater Electrolysis, ChemSusChem, 9 (2016) 962-972.

[73] R.R.T. John C. Crittenden, Davis W. Hand, Kerry J. Howe and George Tchobanoglous, MWH’s Water Treatment: Principles and Design, 3rd ed., John Wiley & Sons, Inc.2012.

[74] K. Fujimura, K. Izumiya, A. Kawashima, E. Akiyama, H. Habazaki, N. Kumagai, K. Hashimoto, Anodically deposited manganese-molybdenum oxide anodes with high selectivity for evolving oxygen in electrolysis of seawater, J. Appl. Electrochem., 29 (1999) 769-775.

[75] L. Yu, Q. Zhu, S. Song, B. McElhenny, D. Wang, C. Wu, Z. Qin, J. Bao, Y. Yu, S. Chen, Z. Ren, Non-noble metal-nitride based electrocatalysts for high-performance alkaline seawater electrolysis, Nat. Commun., 10 (2019) 5106.

[76] A.J. Bard, Inner-Sphere Heterogeneous Electrode Reactions. Electrocatalysis and Photocatalysis: The Challenge, J. Am. Chem. Soc., 132 (2010) 7559-7567.

[77] J.O.M. Bockris, R.J. Mannan, A. Damjanovic, Dependence of the Rate of Electrodic Redox Reactions on the Substrate, J. Chem. Phys., 48 (2003) 1898-1904.

[78] S. Fierro, T. Nagel, H. Baltruschat, C. Comninellis, Investigation of the oxygen evolution reaction on Ti/IrO2 electrodes using isotope labelling and on-line mass spectrometry, Electrochem. Commun., 9 (2007) 1969-1974.

[79] J.O.M. Bockris, Kinetics of Activation Controlled Consecutive Electrochemical Reactions: Anodic Evolution of Oxygen, J. Chem. Phys., 24 (2004) 817-827.

[80] P. Castelli, S. Trasatti, F.H. Pollak, W.E. O'Grady, Single crystals as model electrocatalysts: Oxygen evolution on RuO2 (110), J. Electroanal. Chem., 210 (1986) 189-194.

[81] H. Over, Surface Chemistry of Ruthenium Dioxide in Heterogeneous Catalysis and Electrocatalysis: From Fundamental to Applied Research, Chem. Rev., 112 (2012) 3356-3426.

[82] J.K.N. B. Hammer, Theoretical Surface Science and Catalysis - Calculations and Concepts, Adv. Catal., 45 (2000) 71.

[83] M. Busch, E. Ahlberg, I. Panas, Electrocatalytic oxygen evolution from water on a Mn(iii–v) dimer model catalyst—A DFT perspective, Phys. Chem. Chem. Phys., 13 (2011) 15069-15076.

[84] M. Busch, Water oxidation: From mechanisms to limitations, Curr. Opin. Electrochem., 9 (2018) 278-284.

[85] S. Geiger, O. Kasian, M. Ledendecker, E. Pizzutilo, A.M. Mingers, W.T. Fu, O. Diaz-Morales, Z. Li, T. Oellers, L. Fruchter, A. Ludwig, K.J.J. Mayrhofer, M.T.M. Koper, S.

Cherevko, The stability number as a metric for electrocatalyst stability benchmarking, Nat. Catal., 1 (2018) 508-515.

[86] V. Pfeifer, T.E. Jones, J.J. Velasco Vélez, R. Arrigo, S. Piccinin, M. Hävecker, A. Knop-Gericke, R. Schlögl, In situ observation of reactive oxygen species forming on oxygen-evolving iridium surfaces, Chem. Sci., 8 (2017) 2143-2149.

[87] E. Sargeant, F. Illas, P. Rodríguez, F. Calle-Vallejo, Importance of the gas-phase error correction for O2 when using DFT to model the oxygen reduction and evolution reactions, J. Electroanal. Chem., 896 (2021) 115178.

[88] R. Urrego-Ortiz, S. Builes, F. Illas, F. Calle-Vallejo, Gas-phase errors in computational electrocatalysis: a review, EES Catalysis, 2 (2024) 157-179.

[89] F.S. Jens K. Nørskov, Frank Abild-Pedersen, and Thomas Bligaard, Fundamental Concepts in Heterogeneous Catalysis, First ed., John Wiley and Sons2014.

[90] N. Abidi, K.R.G. Lim, Z.W. Seh, S.N. Steinmann, Atomistic modeling of electrocatalysis: Are we there yet?, Wiley interdisciplinary reviews. Computational molecular science, 11 (2021) e1499.

[91] J. Rossmeisl, A. Logadottir, J.K. Nørskov, Electrolysis of water on (oxidized) metal surfaces, Chem. Phys., 319 (2005) 178-184.

[92] N.B. Halck, V. Petrykin, P. Krtil, J. Rossmeisl, Beyond the volcano limitations in electrocatalysis – oxygen evolution reaction, Phys. Chem. Chem. Phys., 16 (2014) 13682-13688.

[93] K.S. Exner, On the mechanistic complexity of oxygen evolution: potential-dependent switching of the mechanism at the volcano apex, Materials Horizons, 10 (2023) 2086-2095.

[94] Y.-H. Fang, Z.-P. Liu, Mechanism and Tafel Lines of Electro-Oxidation of Water to Oxygen on RuO2(110), J. Am. Chem. Soc., 132 (2010) 18214-18222.

[95] T. Reier, H.N. Nong, D. Teschner, R. Schlögl, P. Strasser, Electrocatalytic Oxygen Evolution Reaction in Acidic Environments – Reaction Mechanisms and Catalysts, Adv. Energy Mater., 7 (2017) 1601275.

[96] M.T.M. Koper, Thermodynamic theory of multi-electron transfer reactions: Implications for electrocatalysis, J. Electroanal. Chem., 660 (2011) 254-260.

[97] H. Dau, C. Limberg, T. Reier, M. Risch, S. Roggan, P. Strasser, The Mechanism of Water Oxidation: From Electrolysis via Homogeneous to Biological Catalysis, ChemCatChem, 2 (2010) 724-761.

[98] S. Saha, P. Gayen, V.K. Ramani, Facet-dependent Chlorine and Oxygen Evolution Selectivity on RuO2: An Ab initio Atomistic Thermodynamic Study, ChemCatChem, 12 (2020) 4922-4929.

[99] Z.W. Seh, J. Kibsgaard, C.F. Dickens, I. Chorkendorff, J.K. Nørskov, T.F. Jaramillo, Combining theory and experiment in electrocatalysis: Insights into materials design, Science, 355 (2017) eaad4998.

[100] F. Calle-Vallejo, J.I. Martínez, J.M. García-Lastra, J. Rossmeisl, M.T.M. Koper, Physical and Chemical Nature of the Scaling Relations between Adsorption Energies of Atoms on Metal Surfaces, Phys. Rev. Lett., 108 (2012) 116103.

[101] I.C. Man, H.-Y. Su, F. Calle-Vallejo, H.A. Hansen, J.I. Martínez, N.G. Inoglu, J. Kitchin, T.F. Jaramillo, J.K. Nørskov, J. Rossmeisl, Universality in Oxygen Evolution Electrocatalysis on Oxide Surfaces, ChemCatChem, 3 (2011) 1159-1165.

[102] T. Bligaard, J.K. Nørskov, S. Dahl, J. Matthiesen, C.H. Christensen, J. Sehested, The Brønsted–Evans–Polanyi relation and the volcano curve in heterogeneous catalysis, J. Catal., 224 (2004) 206-217.

[103] J. Rossmeisl, Z.W. Qu, H. Zhu, G.J. Kroes, J.K. Nørskov, Electrolysis of water on oxide surfaces, J. Electroanal. Chem., 607 (2007) 83-89.

[104] M.N. R.A. van Santen, Molecular Heterogeneous Catalysis: A Conceptual and Computational Approach, Wiley-VCH Verlag GmbH & Co. KGaA, Germany, 2006.

[105] K.S. Exner, Importance of the Walden Inversion for the Activity Volcano Plot of Oxygen Evolution, Advanced Science, 10 (2023) 2305505.

[106] F. Hess, H. Over, Coordination Inversion of the Tetrahedrally Coordinated Ru4f Surface Complex on RuO2(100) and Its Decisive Role in the Anodic Corrosion Process, ACS Catal., 13 (2023) 3433-3443.

[107] T. Binninger, M.-L. Doublet, The Ir–OOOO–Ir transition state and the mechanism of the oxygen evolution reaction on IrO2(110), Energy Environ. Sci., 15 (2022) 2519-2528.

[108] H.N. Nong, L.J. Falling, A. Bergmann, M. Klingenhof, H.P. Tran, C. Spöri, R. Mom, J. Timoshenko, G. Zichittella, A. Knop-Gericke, S. Piccinin, J. Pérez-Ramírez, B.R. Cuenya, R. Schlögl, P. Strasser, D. Teschner, T.E. Jones, Key role of chemistry versus bias in electrocatalytic oxygen evolution, Nature, 587 (2020) 408-413.

[109] K.S. Exner, Importance of the volcano slope to comprehend activity and selectivity trends in electrocatalysis, Curr. Opin. Electrochem., 39 (2023) 101284.

[110] J. Chen, Y. Chen, P. Li, Z. Wen, S. Chen, Energetic Span as a Rate-Determining Term for Electrocatalytic Volcanos, ACS Catal., 8 (2018) 10590-10598.

[111] O. Piqué, F. Illas, F. Calle-Vallejo, Designing water splitting catalysts using rules of thumb: advantages, dangers and alternatives, Phys. Chem. Chem. Phys., 22 (2020) 6797-6803.

[112] K.S. Exner, A Universal Descriptor for the Screening of Electrode Materials for Multiple-Electron Processes: Beyond the Thermodynamic Overpotential, ACS Catal., 10 (2020) 12607-12617.

[113] K.S. Exner, Recent Progress in the Development of Screening Methods to Identify Electrode Materials for the Oxygen Evolution Reaction, Adv. Funct. Mater., 30 (2020) 2005060.

[114] K.S. Exner, Universality in Oxygen Evolution Electrocatalysis: High-Throughput Screening and a Priori Determination of the Rate-Determining Reaction Step, ChemCatChem, 12 (2020) 2000-2003.

[115] K.S. Exner, Beyond the Traditional Volcano Concept: Overpotential-Dependent Volcano Plots Exemplified by the Chlorine Evolution Reaction over Transition-Metal Oxides, J. Phys. Chem. C, 123 (2019) 16921-16928.

[116] S. Razzaq, K.S. Exner, Materials Screening by the Descriptor Gmax(η): The Free-Energy Span Model in Electrocatalysis, ACS Catal., 13 (2023) 1740-1758.

[117] S. Mavrikis, M. Göltz, S. Rosiwal, L. Wang, C. Ponce de León, Boron-Doped Diamond Electrocatalyst for Enhanced Anodic H_2O_2 Production, ACS Appl. Energy Mater., 3 (2020) 3169-3173.

[118] J. Suntivich, K.J. May, H.A. Gasteiger, J.B. Goodenough, Y. Shao-Horn, A Perovskite Oxide Optimized for Oxygen Evolution Catalysis from Molecular Orbital Principles, Science, 334 (2011) 1383-1385.

[119] D.A. Kuznetsov, B. Han, Y. Yu, R.R. Rao, J. Hwang, Y. Román-Leshkov, Y. Shao-Horn, Tuning Redox Transitions via Inductive Effect in Metal Oxides and Complexes, and Implications in Oxygen Electrocatalysis, Joule, 2 (2018) 225-244.

[120] A. Grimaud, O. Diaz-Morales, B. Han, W.T. Hong, Y.-L. Lee, L. Giordano, K.A. Stoerzinger, M.T.M. Koper, Y. Shao-Horn, Activating lattice oxygen redox reactions in metal oxides to catalyse oxygen evolution, Nat. Chem., 9 (2017) 457-465.

[121] Y.-T. Kim, P.P. Lopes, S.-A. Park, A.Y. Lee, J. Lim, H. Lee, S. Back, Y. Jung, N. Danilovic, V. Stamenkovic, J. Erlebacher, J. Snyder, N.M. Markovic, Balancing activity, stability and conductivity of nanoporous core-shell iridium/iridium oxide oxygen evolution catalysts, Nat. Commun., 8 (2017) 1449.

[122] W.T. Hong, R.E. Welsch, Y. Shao-Horn, Descriptors of Oxygen-Evolution Activity for Oxides: A Statistical Evaluation, J. Phys. Chem. C, 120 (2016) 78-86.

[123] L. Wu, Z. Guan, D. Guo, L. Yang, X.a. Chen, S. Wang, High-Efficiency Oxygen Evolution Reaction: Controllable Reconstruction of Surface Interface, Small, 19 (2023) 2304007.

[124] T. Binninger, R. Mohamed, K. Waltar, E. Fabbri, P. Levecque, R. Kötz, T.J. Schmidt, Thermodynamic explanation of the universal correlation between oxygen evolution activity and corrosion of oxide catalysts, Sci. Rep., 5 (2015) 12167.

[125] F.-Y. Chen, Z.-Y. Wu, Z. Adler, H. Wang, Stability challenges of electrocatalytic oxygen evolution reaction: From mechanistic understanding to reactor design, Joule, 5 (2021) 1704-1731.

[126] A. Grimaud, A. Demortière, M. Saubanère, W. Dachraoui, M. Duchamp, M.-L. Doublet, J.-M. Tarascon, Activation of surface oxygen sites on an iridium-based model catalyst for the oxygen evolution reaction, Nat. Energy, 2 (2016) 16189.

[127] N. Zhang, Y. Chai, Lattice oxygen redox chemistry in solid-state electrocatalysts for water oxidation, Energy Environ. Sci., 14 (2021) 4647-4671.

[128] V.A. Saveleva, L. Wang, D. Teschner, T. Jones, A.S. Gago, K.A. Friedrich, S. Zafeiratos, R. Schlögl, E.R. Savinova, Operando Evidence for a Universal Oxygen Evolution Mechanism on Thermal and Electrochemical Iridium Oxides, J. Phys. Chem. Lett., 9 (2018) 3154-3160.

[129] S. Cherevko, A.R. Zeradjanin, A.A. Topalov, N. Kulyk, I. Katsounaros, K.J.J. Mayrhofer, Dissolution of Noble Metals during Oxygen Evolution in Acidic Media, ChemCatChem, 6 (2014) 2219-2223.

[130] M. Pourbaix, Atlas of Electrochemical Equilibria in Aqueous Solutions, National Association of Corrosion Engineers, Houston, TX, 1974.

[131] R. Kötz, H.J. Lewerenz, S. Stucki, XPS Studies of Oxygen Evolution on Ru and RuO2 Anodes, J. Electrochem. Soc., 130 (1983) 825.

[132] O. Kasian, J.-P. Grote, S. Geiger, S. Cherevko, K.J.J. Mayrhofer, The Common Intermediates of Oxygen Evolution and Dissolution Reactions during Water Electrolysis on Iridium, Angew. Chem. Int. Ed., 57 (2018) 2488-2491.

[133] R.V. Mom, L.J. Falling, O. Kasian, G. Algara-Siller, D. Teschner, R.H. Crabtree, A. Knop-Gericke, K.J.J. Mayrhofer, J.-J. Velasco-Vélez, T.E. Jones, Operando Structure–Activity–Stability Relationship of Iridium Oxides during the Oxygen Evolution Reaction, ACS Catal., 12 (2022) 5174-5184.

[134] M. Elmaalouf, M. Odziomek, S. Duran, M. Gayrard, M. Bahri, C. Tard, A. Zitolo, B. Lassalle-Kaiser, J.-Y. Piquemal, O. Ersen, C. Boissière, C. Sanchez, M. Giraud, M. Faustini, J. Peron, The origin of the high electrochemical activity of pseudo-amorphous iridium oxides, Nat. Commun., 12 (2021) 3935.

[135] S. Kevin, G. Baptiste, M. Isabelle, K. Olga, Lattice Oxygen Exchange in Rutile IrO2 during the Oxygen Evolution Reaction, J. Phys. Chem. Lett., 11 (2020) 5008-5014.

[136] L. She, G. Zhao, T. Ma, J. Chen, W. Sun, H. Pan, On the Durability of Iridium-Based Electrocatalysts toward the Oxygen Evolution Reaction under Acid Environment, Adv. Funct. Mater., 32 (2022) 2108465.

[137] E. Willinger, C. Massué, R. Schlögl, M.G. Willinger, Identifying Key Structural Features of IrOx Water Splitting Catalysts, J. Am. Chem. Soc., 139 (2017) 12093-12101.

[138] J. Xu, H. Jin, T. Lu, J. Li, Y. Liu, K. Davey, Y. Zheng, S.-Z. Qiao, IrOx·nH2O with lattice water–assisted oxygen exchange for high-performance proton exchange membrane water electrolyzers, Sci. Adv., 9 (2023) eadh1718.

[139] M. Lu, Y. Zheng, Y. Hu, B. Huang, D. Ji, M. Sun, J. Li, Y. Peng, R. Si, P. Xi, C.-H. Yan, Artificially steering electrocatalytic oxygen evolution reaction mechanism by regulating oxygen defect contents in perovskites, Sci. Adv., 8 (2022) eabq3563.

[140] Y. Hao, S.-F. Hung, W.-J. Zeng, Y. Wang, C. Zhang, C.-H. Kuo, L. Wang, S. Zhao, Y. Zhang, H.-Y. Chen, S. Peng, Switching the Oxygen Evolution Mechanism on Atomically Dispersed Ru for Enhanced Acidic Reaction Kinetics, J. Am. Chem. Soc., 145 (2023) 23659-23669.

[141] L.I. Krishtalik, Kinetics and mechanism of anodic chlorine and oxygen evolution reactions on transition metal oxide electrodes, Electrochim. Acta, 26 (1981) 329-337.

[142] L. Krishtalik, Z. Rotenberg, Overvoltage in the anodic evolution of chlorine on graphite. II. Kinetic dependence in different regions of potentials, Zh. Fiz. Khim., 39 (1965) 907.

[143] L. Krishtalik, Z. Rotenberg, Overpotential of the anodic evolution of chlorine on graphite. I. Influence of pH, Zh. Fiz. Khim., 39 (1965) 328-334.

[144] L.J.J. Janssen, J.G. Hoogland, The electrolysis of an acidic NaCl solution with a graphite anode—III. Mechanism of chlorine evolution, Electrochim. Acta, 15 (1970) 941-951.

[145] G. Faita, G. Fiori, J.W. Augustynski, Electrochemical Processes of the Chlorine-Chloride System on Platinum-Iridium-Coated Titanium Electrodes, J. Electrochem. Soc., 116 (1969) 928.

[146] H.B. Beer, The Invention and Industrial Development of Metal Anodes, J. Electrochem. Soc., 127 (1980) 303C.

[147] H.B. Beer, Brit. Patent 1147442, 1965.

[148] S. Trasatti, Electrocatalysis: understanding the success of DSA®, Electrochim. Acta, 45 (2000) 2377-2385.

[149] H. Dong, W. Yu, M.R. Hoffmann, Mixed Metal Oxide Electrodes and the Chlorine Evolution Reaction, J. Phys. Chem. C, 125 (2021) 20745-20761.

[150] K.S. Exner, I. Sohrabnejad-Eskan, H. Over, A Universal Approach To Determine the Free Energy Diagram of an Electrocatalytic Reaction, ACS Catal., 8 (2018) 1864-1879.

[151] S. Trasatti, Electrocatalysis in the anodic evolution of oxygen and chlorine, Electrochim. Acta, 29 (1984) 1503-1512.

[152] H.A. Hansen, I.C. Man, F. Studt, F. Abild-Pedersen, T. Bligaard, J. Rossmeisl, Electrochemical chlorine evolution at rutile oxide (110) surfaces, Phys. Chem. Chem. Phys., 12 (2010) 283-290.

[153] K.S. Exner, J. Anton, T. Jacob, H. Over, Chlorine Evolution Reaction on RuO2(110): Ab initio Atomistic Thermodynamics Study - Pourbaix Diagrams, Electrochim. Acta, 120 (2014) 460-466.

[154] K.S. Exner, J. Anton, T. Jacob, H. Over, Microscopic Insights into the Chlorine Evolution Reaction on RuO2(110): a Mechanistic Ab Initio Atomistic Thermodynamics Study, Electrocatalysis, 6 (2015) 163-172.

[155] K.S. Exner, Design criteria for the competing chlorine and oxygen evolution reactions: avoid the OCl adsorbate to enhance chlorine selectivity, Phys. Chem. Chem. Phys., 22 (2020) 22451-22458.

[156] K.S. Exner, J. Anton, T. Jacob, H. Over, Full Kinetics from First Principles of the Chlorine Evolution Reaction over a RuO2(110) Model Electrode, Angew. Chem. Int. Ed., 55 (2016) 7501-7504.

[157] H. Over, Fundamental Studies of Planar Single-Crystalline Oxide Model Electrodes (RuO2, IrO2) for Acidic Water Splitting, ACS Catal., 11 (2021) 8848-8871.

[158] R. Parsons, General equations for the kinetics of electrode processes, Trans. Faraday Soc., 47 (1951) 1332-1344.

[159] D.-Y. Kuo, J.K. Kawasaki, J.N. Nelson, J. Kloppenburg, G. Hautier, K.M. Shen, D.G. Schlom, J. Suntivich, Influence of Surface Adsorption on the Oxygen Evolution Reaction on IrO2(110), J. Am. Chem. Soc., 139 (2017) 3473-3479.

[160] P. Jovanovič, N. Hodnik, F. Ruiz-Zepeda, I. Arčon, B. Jozinović, M. Zorko, M. Bele, M. Šala, V.S. Šelih, S. Hočevar, M. Gaberšček, Electrochemical Dissolution of Iridium and Iridium Oxide Particles in Acidic Media: Transmission Electron Microscopy, Electrochemical Flow Cell Coupled to Inductively Coupled Plasma Mass Spectrometry, and X-ray Absorption Spectroscopy Study, J. Am. Chem. Soc., 139 (2017) 12837-12846.

[161] C.F. Dickens, C. Kirk, J.K. Nørskov, Insights into the Electrochemical Oxygen Evolution Reaction with ab Initio Calculations and Microkinetic Modeling: Beyond the Limiting Potential Volcano, J. Phys. Chem. C, 123 (2019) 18960-18977.

[162] K.S. Exner, Controlling Stability and Selectivity in the Competing Chlorine and Oxygen Evolution Reaction over Transition Metal Oxide Electrodes, ChemElectroChem, 6 (2019) 3401-3409.

[163] H.S. Taylor, E.F. Armstrong, A theory of the catalytic surface, Proc. R. Soc. Lond. Ser. A-Contain. Pap. Math. Phys. Character, 108 (1925) 105-111.

[164] A. Wang, J. Li, T. Zhang, Heterogeneous single-atom catalysis, Nat. Rev. Chem., 2 (2018) 65-81.

[165] H. Zhang, S. Zuo, M. Qiu, S. Wang, Y. Zhang, J. Zhang, X.W. Lou, Direct probing of atomically dispersed Ru species over multi-edged TiO2 for highly efficient photocatalytic hydrogen evolution, Sci. Adv., 6 (2020) eabb9823.

[166] R. Shen, W. Chen, Q. Peng, S. Lu, L. Zheng, X. Cao, Y. Wang, W. Zhu, J. Zhang, Z. Zhuang, C. Chen, D. Wang, Y. Li, High-Concentration Single Atomic Pt Sites on Hollow CuSx for Selective O2 Reduction to H2O2 in Acid Solution, Chem, 5 (2019) 2099-2110.

[167] D. Ji, L. Fan, L. Li, S. Peng, D. Yu, J. Song, S. Ramakrishna, S. Guo, Atomically Transition Metals on Self-Supported Porous Carbon Flake Arrays as Binder-Free Air Cathode for Wearable Zinc−Air Batteries, Adv. Mater., 31 (2019) 1808267.

[168] C. Gao, S. Chen, Y. Wang, J. Wang, X. Zheng, J. Zhu, L. Song, W. Zhang, Y. Xiong, Heterogeneous Single-Atom Catalyst for Visible-Light-Driven High-Turnover CO2 Reduction: The Role of Electron Transfer, Adv. Mater., 30 (2018) 1704624.

[169] J.K. Nørskov, T. Bligaard, B. Hvolbæk, F. Abild-Pedersen, I. Chorkendorff, C.H. Christensen, The nature of the active site in heterogeneous metal catalysis, Chem. Soc. Rev., 37 (2008) 2163-2171.

[170] C. Vogt, B.M. Weckhuysen, The concept of active site in heterogeneous catalysis, Nat. Rev. Chem., 6 (2022) 89-111.

[171] C.F. Dickens, J.K. Nørskov, A Theoretical Investigation into the Role of Surface Defects for Oxygen Evolution on RuO2, J. Phys. Chem. C, 121 (2017) 18516-18524.

[172] K.A. Stoerzinger, L. Qiao, M.D. Biegalski, Y. Shao-Horn, Orientation-Dependent Oxygen Evolution Activities of Rutile IrO2 and RuO2, J. Phys. Chem. Lett., 5 (2014) 1636-1641.

[173] E.G.a.S. Trasatti, Recent Developments in Understanding Factors of Electrocatalysis, Russ. J. Electrochem., 42 (2006) 1017-1025.

[174] V. Consonni, S. Trasatti, F. Pollak, W.E. O'Grady, Mechanism of chlorine evolution on oxide anodes study of pH effects, J. Electroanal. Chem., 228 (1987) 393-406.

[175] R.R. Rao, M.J. Kolb, J. Hwang, A.F. Pedersen, A. Mehta, H. You, K.A. Stoerzinger, Z. Feng, H. Zhou, H. Bluhm, L. Giordano, I.E.L. Stephens, Y. Shao-Horn, Surface Orientation Dependent Water Dissociation on Rutile Ruthenium Dioxide, J. Phys. Chem. C, 122 (2018) 17802-17811.

[176] P. Adiga, N. William, W. Cindy, K.M. Anusha, N. Sreejith, J. Bharat, A.S. Kelsey, Breaking OER and CER scaling relations via strain and its relaxation in RuO2 (101), Mater. Today Energy, 28 (2022) 101087.

[177] K.S. Exner, J. Anton, T. Jacob, H. Over, Ligand Effects and Their Impact on Electrocatalytic Processes Exemplified with the Oxygen Evolution Reaction (OER) on RuO2(110), ChemElectroChem, 2 (2015) 707-713.

[178] K.S. Exner, J. Anton, T. Jacob, H. Over, Controlling Selectivity in the Chlorine Evolution Reaction over RuO2-Based Catalysts, Angew. Chem. Int. Ed., 53 (2014) 11032-11035.

[179] R.K.B. Karlsson, A. Cornell, Selectivity between Oxygen and Chlorine Evolution in the Chlor-Alkali and Chlorate Processes, Chem. Rev., 116 (2016) 2982-3028.

[180] L.-Å. Näslund, C.M. Sánchez-Sánchez, Á.S. Ingason, J. Bäckström, E. Herrero, J. Rosen, S. Holmin, The Role of TiO2 Doping on RuO2-Coated Electrodes for the Water Oxidation Reaction, J. Phys. Chem. C, 117 (2013) 6126-6135.

[181] B.V. Tilak, V.I. Birss, J. Wang, C.P. Chen, S.K. Rangarajan, Deactivation of Thermally Formed Ru/Ti Oxide Electrodes: An AC Impedance Characterization Study, J. Electrochem. Soc., 148 (2001) D112.

[182] K.M. Macounová, R.K. Pittkowski, R. Nebel, A. Zitolo, P. Krtil, Selectivity of Ru-rich Ru-Ti-O oxide surfaces in parallel oxygen and chlorine evolution reactions, Electrochim. Acta, 427 (2022) 140878.

[183] C. Astudillo, K.M. Macounová, A.M. Frandsen, R. Nebel, J. Rossmeisl, P. Krtil, Ru rich Ru-Mn-O phases for selective suppression of chlorine evolution in sea water electrolysis, Electrochim. Acta, 470 (2023) 143295.

[184] S. Divanis, A.M. Frandsen, T. Kutlusoy, J. Rossmeisl, Lifting the discrepancy between experimental results and the theoretical predictions for the catalytic activity of RuO2(110) towards oxygen evolution reaction, Phys. Chem. Chem. Phys., 23 (2021) 19141-19145.

[185] V. Petrykin, K. Macounova, O.A. Shlyakhtin, P. Krtil, Tailoring the Selectivity for Electrocatalytic Oxygen Evolution on Ruthenium Oxides by Zinc Substitution, Angew. Chem. Int. Ed., 49 (2010) 4813-4815.

[186] Z.-Y. Wu, F.-Y. Chen, B. Li, S.-W. Yu, Y.Z. Finfrock, D.M. Meira, Q.-Q. Yan, P. Zhu, M.-X. Chen, T.-W. Song, Z. Yin, H.-W. Liang, S. Zhang, G. Wang, H. Wang, Non-iridium-based electrocatalyst for durable acidic oxygen evolution reaction in proton exchange membrane water electrolysis, Nat. Mater., 22 (2023) 100-108.

[187] Z.L. Zhao, Q. Wang, X. Huang, Q. Feng, S. Gu, Z. Zhang, H. Xu, L. Zeng, M. Gu, H. Li, Boosting the oxygen evolution reaction using defect-rich ultra-thin ruthenium oxide nanosheets in acidic media, Energy Environ. Sci., 13 (2020) 5143-5151.

[188] A. Zagalskaya, V. Alexandrov, Role of Defects in the Interplay between Adsorbate Evolving and Lattice Oxygen Mechanisms of the Oxygen Evolution Reaction in RuO2 and IrO2, ACS Catal., 10 (2020) 3650-3657.

[189] P. Gayen, S. Saha, K. Bhattacharyya, V.K. Ramani, Oxidation State and Oxygen-Vacancy-Induced Work Function Controls Bifunctional Oxygen Electrocatalytic Activity, ACS Catal., 10 (2020) 7734-7746.

[190] P. Gayen, S. Saha, V. Ramani, Pyrochlores for Advanced Oxygen Electrocatalysis, Acc. Chem. Res., 55 (2022) 2191-2200.

[191] P. Gayen, S. Saha, V. Ramani, Selective Seawater Splitting Using Pyrochlore Electrocatalyst, ACS Appl. Energy Mater., 3 (2020) 3978-3983.

[192] M.A. Subramanian, G. Aravamudan, G.V. Subba Rao, Oxide pyrochlores — A review, Prog. Solid State Chem., 15 (1983) 55-143.

[193] A.F. Fuentes, S.M. Montemayor, M. Maczka, M. Lang, R.C. Ewing, U. Amador, A Critical Review of Existing Criteria for the Prediction of Pyrochlore Formation and Stability, Inorg. Chem., 57 (2018) 12093-12105.

[194] M.A. Hubert, A.M. Patel, A. Gallo, Y. Liu, E. Valle, M. Ben-Naim, J. Sanchez, D. Sokaras, R. Sinclair, J.K. Nørskov, L.A. King, M. Bajdich, T.F. Jaramillo, Acidic Oxygen Evolution Reaction Activity–Stability Relationships in Ru-Based Pyrochlores, ACS Catal., 10 (2020) 12182-12196.

[195] H.N. Nong, T. Reier, H.-S. Oh, M. Gliech, P. Paciok, T.H.T. Vu, D. Teschner, M. Heggen, V. Petkov, R. Schlögl, T. Jones, P. Strasser, A unique oxygen ligand environment facilitates water oxidation in hole-doped IrNiOx core–shell electrocatalysts, Nat. Catal., 1 (2018) 841-851.

[196] B. Lu, Q. Liu, S. Chen, Electrocatalysis of Single-Atom Sites: Impacts of Atomic Coordination, ACS Catal., 10 (2020) 7584-7618.

[197] J. Ji, J. Liu, L. Shi, S. Guo, N. Cheng, P. Liu, Y. Gu, H. Yin, H. Zhang, H. Zhao, Ruthenium Oxide Clusters Immobilized in Cationic Vacancies of 2D Titanium Oxide for Chlorine Evolution Reaction, Small Struct., In Press 2300240.

[198] J. Shan, C. Ye, Y. Jiang, M. Jaroniec, Y. Zheng, S.-Z. Qiao, Metal-metal interactions in correlated single-atom catalysts, Sci. Adv., 8 (2022) eabo0762.

[199] J. Cho, T. Lim, H. Kim, L. Meng, J. Kim, S. Lee, J.H. Lee, G.Y. Jung, K.-S. Lee, F. Viñes, F. Illas, K.S. Exner, S.H. Joo, C.H. Choi, Importance of broken geometric symmetry of single-atom Pt sites for efficient electrocatalysis, Nat. Commun., 14 (2023) 3233.

[200] T. Lim, G.Y. Jung, J.H. Kim, S.O. Park, J. Park, Y.-T. Kim, S.J. Kang, H.Y. Jeong, S.K. Kwak, S.H. Joo, Atomically dispersed Pt–N4 sites as efficient and selective electrocatalysts for the chlorine evolution reaction, Nat. Commun., 11 (2020) 412.

[201] J. Shan, C. Ye, S. Chen, T. Sun, Y. Jiao, L. Liu, C. Zhu, L. Song, Y. Han, M. Jaroniec, Y. Zhu, Y. Zheng, S.-Z. Qiao, Short-Range Ordered Iridium Single Atoms Integrated into Cobalt Oxide Spinel Structure for Highly Efficient Electrocatalytic Water Oxidation, J. Am. Chem. Soc., 143 (2021) 5201-5211.

[202] J.B. Souza Junior, G.R. Schleder, J. Bettini, I.C. Nogueira, A. Fazzio, E.R. Leite, Pair Distribution Function Obtained from Electron Diffraction: An Advanced Real-Space Structural Characterization Tool, Matter, 4 (2021) 441-460.

[203] E. Antolini, Iridium As Catalyst and Cocatalyst for Oxygen Evolution/Reduction in Acidic Polymer Electrolyte Membrane Electrolyzers and Fuel Cells, ACS Catal., 4 (2014) 1426-1440.

[204] X. Liang, L. Shi, Y. Liu, H. Chen, R. Si, W. Yan, Q. Zhang, G.-D. Li, L. Yang, X. Zou, Activating Inert, Nonprecious Perovskites with Iridium Dopants for Efficient Oxygen Evolution Reaction under Acidic Conditions, Angew. Chem. Int. Ed., 58 (2019) 7631-7635.

[205] Y. Liu, C. Li, C. Tan, Z. Pei, T. Yang, S. Zhang, Q. Huang, Y. Wang, Z. Zhou, X. Liao, J. Dong, H. Tan, W. Yan, H. Yin, Z.-Q. Liu, J. Huang, S. Zhao, Electrosynthesis of chlorine from seawater-like solution through single-atom catalysts, Nat. Commun., 14 (2023) 2475.

[206] J.E. Bennett, Electrodes for generation of hydrogen and oxygen from seawater, Int. J. Hydrog. Energy., 5 (1980) 401-408.

[207] H. Habazaki, T. Matsui, A. Kawashima, K. Asami, N. Kumagai, K. Hashimoto, Nanocrystalline manganese-molybdenum-tungsten oxide anodes for oxygen evolution in seawater electrolysis, Scr. Mater., 44 (2001) 1659-1662.

[208] N.A. Abdel Ghany, N. Kumagai, S. Meguro, K. Asami, K. Hashimoto, Oxygen evolution anodes composed of anodically deposited Mn–Mo–Fe oxides for seawater electrolysis, Electrochim. Acta, 48 (2002) 21-28.

[209] J.G. Vos, T.A. Wezendonk, A.W. Jeremiasse, M.T.M. Koper, MnOx/IrOx as Selective Oxygen Evolution Electrocatalyst in Acidic Chloride Solution, J. Am. Chem. Soc., 140 (2018) 10270-10281.

[210] M.E.S. Beatty, H. Chen, N.Y. Labrador, B.J. Lee, D.V. Esposito, Structure–property relationships describing the buried interface between silicon oxide overlayers and electrocatalytic platinum thin films, J. Mater. Chem. A., 6 (2018) 22287-22300.

[211] M. Pourbaix, Atlas of Electrochemical Equilibria in Aqueous Solution, National Association of Corrosion Engineers, Houston, Texas, USA, 1974.

[212] J.E. Robinson, N.Y. Labrador, H. Chen, B.E. Sartor, D.V. Esposito, Silicon Oxide-Encapsulated Platinum Thin Films as Highly Active Electrocatalysts for Carbon Monoxide and Methanol Oxidation, ACS Catal., 8 (2018) 11423-11434.

[213] Y. Marcus, Ionic radii in aqueous solutions, Chem. Rev., 88 (1988) 1475-1498.

[214] J.G. Vos, A.A. Bhardwaj, A.W. Jeremiasse, D.V. Esposito, M.T.M. Koper, Probing the Effects of Electrode Composition and Morphology on the Effectiveness of Silicon Oxide Overlayers to Enhance Selective Oxygen Evolution in the Presence of Chloride Ions, J. Phys. Chem. C, 126 (2022) 20314-20325.

[215] R. Balaji, B.S. Kannan, J. Lakshmi, N. Senthil, S. Vasudevan, G. Sozhan, A.K. Shukla, S. Ravichandran, An alternative approach to selective sea water oxidation for hydrogen production, Electrochem. Commun., 11 (2009) 1700-1702.

[216] R. Venkatkarthick, S. Elamathi, D. Sangeetha, R. Balaji, B. Suresh Kannan, S. Vasudevan, D. Jonas Davidson, G. Sozhan, S. Ravichandran, Studies on polymer modified metal oxide anode for oxygen evolution reaction in saline water, J. Electroanal. Chem., 697 (2013) 1-4.

[217] A.R. Jadhav, A. Kumar, J. Lee, T. Yang, S. Na, J. Lee, Y. Luo, X. Liu, Y. Hwang, Y. Liu, H. Lee, Stable complete seawater electrolysis by using interfacial chloride ion blocking layer on catalyst surface, J. Mater. Chem. A., 8 (2020) 24501-24514.

[218] N. Kitiphatpiboon, M. Chen, C. Feng, Y. Kansha, S. Li, A. Abudula, P. Wu, Y. Ma, G. Guan, Highly durable FeNiSx/NiFe(OH)x electrocatalyst for selective oxygen evolution reaction in alkaline simulated seawater at high current densities, Int. J. Hydrog. Energy., 48 (2023) 34255-34271.

[219] S. Loomba, M.W. Khan, M. Haris, S.M. Mousavi, A. Zavabeti, K. Xu, A. Tadich, L. Thomsen, C.F. McConville, Y. Li, S. Walia, N. Mahmood, Nitrogen-Doped Porous Nickel Molybdenum Phosphide Sheets for Efficient Seawater Splitting, Small, 19 (2023) 2207310.

[220] K. Obata, K. Takanabe, A Permselective CeOx Coating To Improve the Stability of Oxygen Evolution Electrocatalysts, Angew. Chem. Int. Ed., 57 (2018) 1616-1620.

[221] M. Balasubramanian, C.A. Melendres, A.N. Mansour, An X-ray absorption study of the local structure of cerium in electrochemically deposited thin films, Thin Solid Films, 347 (1999) 178-183.

[222] H. Han, S.J. Kim, S.Y. Jung, D. Oh, A.K. Nayak, J.U. Jang, J. Bang, S. Yeo, T.H. Shin, Amorphous-Crystalline Interfaces on Hollow Nanocubes Derived from Ir-Doped Ni–Fe–Zn Prussian Blue Analog Enables High Capability of Alkaline/Acidic/Saline Water Oxidations, Small, 19 (2023) 2303912.

[223] H. Xie, Z. Zhao, T. Liu, Y. Wu, C. Lan, W. Jiang, L. Zhu, Y. Wang, D. Yang, Z. Shao, A membrane-based seawater electrolyser for hydrogen generation, Nature, 612 (2022) 673-678.

[224] H. Shi, T. Wang, J. Liu, W. Chen, S. Li, J. Liang, S. Liu, X. Liu, Z. Cai, C. Wang, D. Su, Y. Huang, L. Elbaz, Q. Li, A sodium-ion-conducted asymmetric electrolyzer to lower the operation voltage for direct seawater electrolysis, Nat. Commun., 14 (2023) 3934.

[225] D.B.I. Yet-Ming Chiang, W. David Kingery, Physical Ceramics: Principles for Ceramic Science and Engineering, John Wiley and Sons, Inc.1997.

[226] R. Rousseau, V.-A. Glezakou, A. Selloni, Theoretical insights into the surface physics and chemistry of redox-active oxides, Nat. Rev. Mater., 5 (2020) 460-475.

[227] M. Reticcioli, I. Sokolović, M. Schmid, U. Diebold, M. Setvin, C. Franchini, Interplay between Adsorbates and Polarons: CO on Rutile TiO2 (110), Phys. Rev. Lett., 122 (2019) 016805.

[228] K.A. Stoerzinger, W.S. Choi, H. Jeen, H.N. Lee, Y. Shao-Horn, Role of Strain and Conductivity in Oxygen Electrocatalysis on LaCoO3 Thin Films, J. Phys. Chem. Lett., 6 (2015) 487-492.

[229] Y. Tian, S. Wang, E. Velasco, Y. Yang, L. Cao, L. Zhang, X. Li, Y. Lin, Q. Zhang, L. Chen, A Co-Doped Nanorod-like RuO2 Electrocatalyst with Abundant Oxygen Vacancies for Acidic Water Oxidation, iScience, 23 (2020) 100756.

[230] A.E. Thorarinsdottir, D.G. Nocera, Energy catalysis needs ligands with high oxidative stability, Chem Catal., 1 (2021) 32-43.

[231] H. Lux, “Säuren” und “Basen” im Schmelzfluss: Die Bestimmung der Sauerstoffionen-Konzentration, Zeitschrift für Elektrochemie und angewandte physikalische Chemie, (1939).

[232] R.H. Crabtree, The Organometallic Chemistry of the Transition Metals, John Wiley & Sons(2014).

[233] C. Costentin, D.G. Nocera, Self-healing catalysis in water, Proc. Natl. Acad. Sci., 114 (2017) 13380-13384.

[234] M. Huynh, D.K. Bediako, D.G. Nocera, A Functionally Stable Manganese Oxide Oxygen Evolution Catalyst in Acid, J. Am. Chem. Soc., 136 (2014) 6002-6010.

[235] M. Fleischmann, H.R. Thirsk, I.M. Tordesillas, Kinetics of electrodeposition of γ-manganese dioxide, Trans. Faraday Soc., 58 (1962) 1865-1877.

[236] M. Huynh, D.K. Bediako, Y. Liu, D.G. Nocera, Nucleation and Growth Mechanisms of an Electrodeposited Manganese Oxide Oxygen Evolution Catalyst, J. Phys. Chem. C, 118 (2014) 17142-17152.

[237] Y. Surendranath, M. Dincă, D.G. Nocera, Electrolyte-Dependent Electrosynthesis and Activity of Cobalt-Based Water Oxidation Catalysts, J. Am. Chem. Soc., 131 (2009) 2615-2620.

[238] T.P. Keane, D.G. Nocera, Selective Production of Oxygen from Seawater by Oxidic Metallate Catalysts, ACS Omega., 4 (2019) 12860-12864.

[239] T.P. Keane, S.S. Veroneau, A.C. Hartnett, D.G. Nocera, Generation of Pure Oxygen from Briny Water by Binary Catalysis, J. Am. Chem. Soc., 145 (2023) 4989-4993.